Synthesis and Physico-Chemical Characterization of Semiconducting Nano-crystalline Photocatalysts and its Application in Environmental Remediation

BY

ABUL LAIS

A Thesis Presented to the
DEANSHIP OF GRADUATE STUDIES

KING FAHD UNIVERSITY OF PETROLEUM & MINERALS

DHAHRAN, SAUDI ARABIA

In Partial Fulfillment of the
Requirements for the Degree of

MASTER OF SCIENCE

In

PHYSICS

JANUARY 2018

KING FAHD UNIVERSITY OF PETROLEUM & MINERALS

DHAHRAN 31261, SAUDI ARABIA

DEANSHIP OF GRADUATE STUDIES

This thesis, written by **ABUL LAIS** under the direction of his thesis adviser and approved by his thesis committee, has been presented to and accepted by the Dean of Graduate Studies, in partial fulfilment of the requirements for the degree of **MASTER OF SCIENCE IN PHYSICS.**

Thesis Committee

M. A. Gondal

Dr. Mohammad A. Gondal (Advisor)

Dr. Zain Hassan Yamani (Member)

Dr. Chanbasha Basheer (Member)

Dr. A. A. Al-Sunaidi
Department Chairman

Dr. Salam A. Zummo
Dean of Graduate Studies

29/1/18

Date

Dedicated to my parents

ACKNOWLEDGMENTS

All thanks and praise belong to Allah ta'aala for the innumerable gifts and bounties showered upon us daily. In addition, I am grateful to my thesis advisor Distinguished Professor Dr. M. A. Gondal for his extensive encouragement, guidance, support, ideas and assistance with troubleshooting throughout the course of this research project. Also, I convey my deepest appreciation to my thesis committee members: Dr. Zain Hassan Yamani, for his tremendous support, encouragement, time and assistance towards a successful thesis, and Dr. Basheer Chanbasha, for his words of encouragement during the course of my work.

In addition, I convey my sincerest thanks to the entire physics faculty and staff members for their innumerable instances of support, whether direct or indirect, during my research efforts. In particular, I would like to pay special gratitude to those professors who are also my teachers: Dr. M. M. Faiz, Dr. F. Z. Khiari, Dr. T. A. Al-Aithan, Dr. I. M. A. Nasser, Dr. M. F. Al-Kuhaili, Dr Khalil Ziq, Dr. A. A. Naqvi and Dr. Khalil Harrabi. Also, to the chairman of the physics department, Dr. A. A. Al-Sunaidi, I utter my heartfelt thanks for his endless support in all our endeavours.

I will never be able to sufficiently thank the following persons: Dr. Fida Al-Adel, Dr. Umair. Baig, Mr. M. A. Dastageer, Mr. S Pillai and the entire team of the laser research group, including Mr. Luqman Oloore, Mr. Q. Talal, Mr Mohsin Sarwar, Mr. Redhwan Moqbel, Mr. Lutfi Mulyadi; I thank you all. Special thanks also goes to the entire

membership of the Center of Research Excellence in Nanotechnology (CENT), under the directorship of Dr. Zain Hassan Yamani. I appreciate contribution from CENT to the successful characterization of the samples for this thesis work. Also, I thank CENT as well as Deanship of Scientific Research for financial aid during the course of this work.

Above all, sincere acknowledgment is due to the Kingdom of Saudi Arabia and King Fahd University of Petroleum and Minerals (KFUPM) for offering this amazing scholarship that has allowed me to enhance my knowledge and wisdom drastically. Lastly, I am always grateful to my parents for their constant support and care in countless forms till date.

TABLE OF CONTENTS

LIST OF TABLES

LIST OF FIGURES

THESIS ABSTRACT (ENGLISH)

NAME:	Abul Lais
TITLE OF STUDY:	Synthesis and Physico-Chemical Characterization of Semiconducting Nano-crystalline Photocatalysts and its Application in Environmental Remediation
MAJOR FIELD:	Physics
DATE OF DEGREE:	January 2018

This thesis focused on the synthesis and characterization of semiconductor photocatalysts and its application in environmental remediation by photocatalytic reduction of CO_2 to value-added hydrocarbon products, especially methanol. We have synthesized and extensively characterized two semiconductor photocatalytic materials: graphitic carbon nitride ($g\text{-}C_3N_4$), which is an excellent solar-harvesting photocatalyst for large scale CO_2 conversion into fuels, and silver-loaded sodium niobate (Ag-loaded $NaNbO_3$), which exhibits significantly enhanced methanol product selectivity over pure sodium niobate. These photocatalytic materials are extensively characterized to study their electronic, optical, morphological and crystallographic properties, to understand how its properties correlate with the observed photocatalytic performance. For this purpose, various advanced analytical equipment were employed such as XPS, XRD, UV-Vis, FT-IR, PL, Raman and FESEM,

for characterizing the photocatalysts. After materials characterization, these photocatalysts were applied for the conversion of CO_2 to fuels, especially methanol.

Firstly, g-C_3N_4, was tested using 3 different irradiation sources (solar radiation, UV lamp, and pulsed laser). After 40 min of irradiation, 355-nm pulsed laser (40 mJ/pulse, 10 Hz) rendered the best methanol production yield (510 μmol g^{-1}), followed by solar radiation (130 μmol g^{-1}), and UV broadband lamp (110 μmol g^{-1}). Pulsed laser gave the best methanol yield due to its high photon flux and monochromaticity, but the methanol yield of 130 μmol g^{-1} with natural sunlight is a very significant development, as it can be used for the development of large-scale solar fuel generation facilities by harnessing the naturally abundant solar radiation.

Secondly, pure and Ag-loaded $NaNbO_3$ were applied for photocatalytic CO_2 reduction under UV lamp irradiation exclusively, and the silver loading was found to significantly enhance the methanol product selectivity over that of formic acid. This implies that depositing metal atoms on existing photocatalytic materials can alter the product distribution selectivity in favour of a particular hydrocarbon compound, such as methanol in this case. Extensive literature review revealed that loading silver changes 3 surface properties of photocatalytic materials: surface hydrophobicity, surface electron density and CO_2 binding modes. These changes hold the key to understanding the underlying reason as to why silver deposition enhances the methanol product selectivity.

THESIS ABSTRACT (ARABIC)

ركزت هذه الأطروحة على توليف وتوصيف ضوئي أشباه الموصلات وتطبيقه في المعالجة البيئية عن طريق تقليل التحفيز الضوئي من ثاني أكسيد الكربون إلى منتجات الهيدروكربون ذات القيمة المضافة، وخاصة الميثانول. لقد قمنا بتوليف وتميز على نطاق واسع اثنين من مواد أشباه الموصلات ضوئي: نيتريد الكربون غرافيتيك($g\text{-}C_3N_4$) ، وهو ممتاز ضوئي حاصد للطاقة الشمسية لتحويل ثاني أكسيد الكربون على نطاق واسع في الوقود، والفضة نيوبات الصوديوم تحميل ($Ag\text{-}$ تحميل($NaNbO_3$ ، والتي المعارض تعزيز كبير الانتقائية المنتج الميثانول فوق نيوبات الصوديوم النقي. وتتميز هذه المواد تحفيز ضوئي على نطاق واسع لدراسة خصائصها الإلكترونية والبصرية والمورفولوجية والبلورية، لفهم كيف ترتبط خصائصها مع أداء ضوئي. لهذا الغرض، تم استخدام مختلف المعدات التحليلية المتقدمة مثل زس، زرد، الأشعة فوق البنفسجية فيس، فت-إر، بل، رامان و فيسم، لتوصيف ضوئي. بعد توصيف المواد، تم تطبيق هذه المحفزات الضوئية لتحويل ثاني أآسيد الكربون إلى أنواع الوقود، وخاصة الميثانول.

أولا، $g\text{-}C_3N_4$، تم اختباره باستخدام 3 مصادر التشعيع مختلفة (الإشعاع الشمسي، مصباح الأشعة فوق البنفسجية، والليزر نابض). بعد 40 دقيقة من التشعيع، قدم الليزر 355 نانومتر (40 مللي جول / نبض، 10 هرتز) أفضل إنتاج إنتاج الميثانول 510 ميكرومول ز$^{-1}$, تليها الإشعاع الشمسي 130 ميكرومول ز$^{-1}$ ، والأشعة فوق البنفسجية مصباح النطاق العريض 110 ميكرومول ز$^{-1}$. أعطى الليزر نابض أفضل عائد الميثانول بسبب تدفقه الفوتون عالية وحيدة اللون، ولكن الغلة الميثانول من 130 ميكرومول ز$^{-1}$ مع أشعة الشمس الطبيعية هو تطور كبير جدا، كما أنه يمكن استخدامها لتطوير واسعة النطاق مرافق توليد الوقود الشمسي عن طريق تسخير الإشعاع الشمسي الوفير بشكل طبيعي.

ثانيا، تم تطبيق $NaNbO_3$ نقية و أغ-لوادد للتحليل الضوئي CO_2 تحت أشعة مصباح الأشعة فوق البنفسجية حصرا، وتم العثور على تحميل الفضة لتعزيز كبير الانتقائية المنتج الميثانول أكثر من حمض الفورميك. وهذا يعني أن إيداع ذرات معدنية على مواد تحفيز ضوئية قائمة يمكن أن يغير انتقائية توزيع المنتجات لصالح مركب هيدروكربوني معين، مثل الميثانول لهذه الدراسة. وكشفت مراجعة الأدب واسعة النطاق أن تحميل الفضة التغييرات 3 خصائص سطح المواد التحفيز الضوئي: هدروفوبيسيتي السطح، وكثافة الإلكترون السطحية وسائط ملزم CO_2. هذه التغييرات تحمل المفتاح لفهم السبب الكامن وراء مضيفا الفضة يزيد الانتقائية منتج الميثانول.

CHAPTER 1

INTRODUCTION AND OVERVIEW

Global warming is widely perceived as one of the most pressing environmental concerns grappling humanity today [1-4]. According to a report published by the IPCC (Intergovernmental Panel on Climate Change), the average increase of the earth's surface temperature was as great as 0.9 °C between 1906 and 2005, and the rate of increase virtually doubled during the last half a century [5]. It is alarming to know that by 2100, the mean global temperature could potentially increase by 2 °C [6]. The consequences of global warming are catastrophic and universal; for instance, molten ice caps at the earth's poles could flood and drown low-lying lands [7] and cause extreme weather-related natural calamities like heat waves, droughts, hurricanes etc. [8].

There are many harmful gases like methane, nitrous oxides and carbon dioxide, which are being excessively released to the fragile atmosphere through heavy industrialization and reckless human activities. Through the greenhouse effect, these gases lead to global warming. Amongst these, CO_2 wreaks more havoc to the environment owing to its high concentration and long lifetime [9]. More significantly, since the dawn of industrialization two centuries ago, atmospheric CO_2 levels have been steadily rising. Measurements obtained from Antarctic ice cores emphatically demonstrate that CO_2 levels are higher today than at any point in the past 800,000 years [10], having risen by 40% between 1750 and 2011 and, for the first time in human history, exceeded 400 ppm in 2013 [11]. The major source of human-induced CO_2 emission is invariably from the combustion of fossil fuels for energy production. For instance, in the United States, fossil fuel combustion accounted for 93.3% of CO_2 emissions in 2015 [12]. Realistically, in the modern society, man's overdependence on energy cannot be reduced. In this context, the development of a technology that caters to the energy demands of humanity without jeopardizing the environment is imperative.

Amongst all the alternate energy sources explored, solar energy is more promising as it is ubiquitous and convertible to other energy forms. Solar energy can be harvested by many techniques such as photovoltaic cells, solar power towers [13-17] and photochemical reactors. The former two processes convert solar irradiation into electricity and molten salt [18-22] respectively and, though encouraging, the low-density energy storage is a major limiting factor of these technologies. On the other hand, in photocatalytic processes, CO_2 and H_2O are converted into value-added hydrocarbon fuels like HCHO, HCOOH, CH_4, CH_3OH etc. using solar radiation and a photocatalyst. For instance, molten salt (1:1 mixture by weight of $NaNO_3$:KNO_3) stores approximately 0.9 GJ/m^3 [23] whereas methanol stores an order of magnitude more at 15.6 GJ/m^3. This process helps sequester atmospheric CO_2 into valuable hydrocarbon fuels, thus simultaneously catering to global energy needs whilst reducing the excessive CO_2 content in the atmosphere.

To achieve the aforementioned green objectives, the quest is on to develop an artificial photosynthetic (APS) system, which is a cost-effective method for efficiently transforming carbon dioxide gas into value-added hydrocarbon fuels in the presence of solar energy and a suitable photocatalyst. There are numerous review articles discussing photocatalytic reduction of CO_2 to generate a variety of C1/C2 products [24-39]. Amongst these reduction products, methanol is the most promising and sought after, as it is a high-density liquid fuel, that can be easily transported using existing pipeline infrastructure. It also finds widespread usage as a chemical precursor [40-42] in the industrial sector. The greater significance of methanol lies in the near-simultaneous development of direct-methanol fuel cells (DMFCs), which can easily convert it to electricity in a single step. DMFCs are very actively being studied nowadays [43-53]. Also, methanol can be mixed with gasoline and injected directly into cars [54-58], whereby the emitted CO_2 can be converted back into fuel by an APS. This process is envisioned as part of a methanol economy [59-61] that finally accomplishes true "green cars" by closing the carbon loop. Hence, for this study, we select methanol as the ideal reduction product from the photocatalytic reduction of CO_2.

To achieve this noble vision, frenzied scientific research has been ongoing to improve the efficiency of the CO_2-to-fuel conversion process, technically known as photocatalytic CO_2 reduction. Improving efficiency, in this context, is broadly defined as increasing the yield of fuels for a given set of input parameters (CO_2 flow rate, photon intensity, amount of catalyst used). For the photochemical conversion of CO_2 into methanol, most contemporary researchers focus on three areas: photocatalyst synthesis, photoreactor design and engineering, and optimising experimental parameters.

In brief, we synthesise and characterize suitable photocatalysts for this process. Next, these photocatalysts are applied for CO_2 reduction to methanol. In addition, experimental parameters are optimised to enhance the methanol production yields even further. These endeavours will pave the way for a “green” methanol economy, by eventually using naturally abundant solar radiation with the help of inexpensive photocatalysts to convert atmospheric CO_2 into methanol.

In this thesis, we will investigate the photocatalytic conversion of CO_2 into value-added hydrocarbon fuels, especially methanol. Firstly, a thorough literature search will be conducted to understand the current technological state of this process. This literature review will be presented in Chapter 2, where suitable photocatalysts (section 2.2) and experimental parameters (section 2.3) are explored in depth. Insights gleamed off this literature review will then guide the experimental phase of this study.

The primary objective of this thesis is twofold: firstly, to develop a solar-harvesting photocatalyst that can convert CO_2 to methanol directly using natural sunlight, and secondly, to enhance the methanol product selectivity of a reported photocatalyst. After extensive literature review and trial-and-error experimentation, we have decided upon graphitic carbon nitride (g-C_3N_4) as the solar-harvesting photocatalyst, and Ag-loaded $NaNbO_3$ as the methanol-selective CO_2 reduction photocatalyst.

In chapter 3, the experimental details (synthesis procedures, reactor set-up etc.) are presented for this study. In chapter 4, the materials characterization results are presented for the two aforementioned photocatalysts selected for this study. Subsequently, these photocatalysts are applied for the photocatalytic CO_2 reduction reaction into hydrocarbons. Results obtained are presented in chapter 5. The results will be explained from first principles in those instances where the reaction mechanism has been properly understood, and suitable hypotheses will be offered if it has not yet been fully clarified. This study ends off with concluding remarks presented in chapter 6, along with recommendations for future study.

CHAPTER 2

LITERATURE REVIEW

2.1 A brief overview

As noted in chapter 1, the vast majority of contemporary photocatalytic CO_2 reduction researchers focus on three areas: photocatalyst synthesis, photoreactor design and engineering, and optimising experimental parameters. This thesis will investigate the first (photocatalyst synthesis – section 2.2) and third (experimental parameters – section 2.3) areas. For the literature review hereunder, we will explore several reported photocatalysts (section 2.2) for the CO_2-to-methanol reduction process, and also analysing the theoretical basis for several experimental parameters (section 2.3) that affect the CO_2-to-methanol conversion rate.

2.2 Review of semiconductor oxide photocatalysts

There are numerous photocatalysts that have been reported for the photocatalytic CO_2 reduction process, and they can be broadly classified into 3 groups: semiconducting materials, layered double hydroxides (LDHs) and carbon nanomaterials [62].

Under semiconductor-based photocatalysts, there are various sub-classes like oxides, nitrides, carbides [63], halides [64-66], sulfides [67-72] etc. Photocatalysts based on semiconducting oxides can be further classified into TiO_2-based and non-TiO_2-based oxides. An enormous amount of work has been carried out for TiO_2 using different variants of pure, doped and nanostructured TiO_2 as it is a pioneering photocatalyst material [73-79].

In addition, there are many carbon nanomaterials-based catalysts like g-C_3N_4 [80-88], graphene [89-92], graphene oxide [93-95], multi-walled carbon nanotubes [96-98], carbon quantum dots [99] etc. which have been applied for the photocatalytic conversion of CO_2 into methanol.

In this section, we will study the less-reviewed non-TiO_2-based semiconducting oxide photocatalysts for converting CO_2 into methanol. As mentioned earlier, the inherent limitations such as poor visible-light sensitivity, low reactants' adsorption, high charge carrier recombination rate, slow reaction kinetics and consequently low methanol yield have significantly hampered the progress of this technology. Hence, the discussion of this section will be centered on various creative strategies adopted, for each photocatalyst, to minimise the aforementioned limiting factors so that methanol yield through photocatalytic reduction of CO_2 is maximized. The trends deduced here can be extrapolated for developing novel photocatalytic materials with improved methanol yield.

This following section covers the following non-TiO_2-based semiconducting oxide photocatalysts: bismuth (V) vanadate ($BiVO_4$ – Section 2.2.1), bismuth (III) tungstate (Bi_2WO_6 – Section 2.2.2), copper (II) ferrite ($CuFe_2O_4$ – Section 2.2.3) and sodium niobate ($NaNbO_3$ – Section 2.2.4).

2.2.1 Bismuth (V) vanadate ($BiVO_4$)

Bismuth vanadate is a stable, visible-light sensitive photocatalyst, with proven performance for converting CO_2 into methanol. Synthetic $BiVO_4$ exists in 3 crystalline phases: zircon structure with tetragonal system (z-t), scheelite structure with monoclinic (s-m) and scheelite structure with tetragonal (s-t) systems. The phase transformation from the s-m to s-t crystalline phase is achieved by heating to 255 ^oC [100-101], whilst the z-t to s-m phase transformation occurs by heating at approximately 400 – 600 ^oC [102]. The photocatalytic activity of the z-t phase is low [103-104], whilst that of the s-m phase is the highest owing to its small band energy-gap (~ 2.4 eV) [105-107].

2.2.1.1 Photocatalytic reduction of CO_2 to methanol

Mao et al. [108] used the pure monoclinic (s-m) phase (i.e. lamellar $BiVO_4$) for photocatalytic CO_2 conversion to methanol and obtained a methanol yield of ~ 175 μmol/g-cat (after 9 hours) and an O_2/CH_3OH ratio of ~ 1.22, which is less than the theoretically predicted value of 1.5. This discrepancy is attributed to errors in O_2 detection and/or O_2 dissolution in the reaction medium.

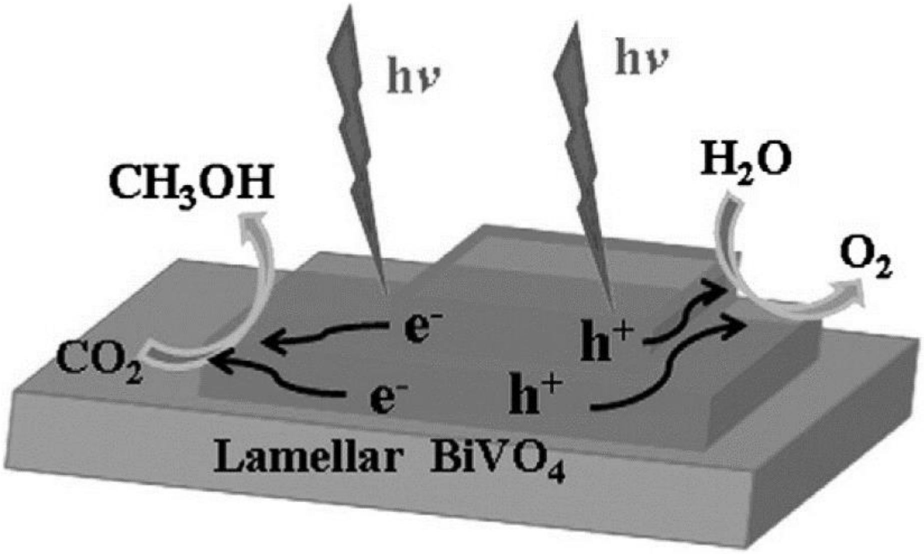

Fig. 2.1 Proposed mechanism of CH_3OH production from the CO_2 reduction. Reproduced from [108].

Mao et al. [108] also proposed a charge transfer mechanism (Fig. 2.1), and noted that the optimum catalyst loading and NaOH concentrations were 2 g/L and 1.0 M respectively. It was hypothesized that increased basicity enhanced the methanol yield by improving CO_2 solubility in the reaction medium, and the hydroxyl ion scavenges holes to enhance charge-carrier separation. However, when the NaOH concentration exceeded 1.0 M, only a marginal increase of methanol yield was observed, and it is not worth risking damage to chromatographic column caused by a strongly-basic solution. Also, after 9 hours of irradiation, the methanol yield saturated and remained unchanged, which is often ascribed to methanol re-oxidation. Gondal et al. [63] noted that two competitive reactions (i.e. photo-reduction with rate k_r and photo-oxidation with rate k_o – Fig. 2.2) occur during photocatalytic conversion of CO_2 to methanol. Initially, the photoreduction rates (k_r) will be faster than photooxidation rates (k_o) because of the low concentration of methanol produced. As the methanol concentration gradually builds up and approaches its threshold value, the two photoreaction rates become equal (i.e. $k_r = k_o$), and the absolute methanol concentration becomes stationary in batch-phase reactions, provided the photocatalyst's valence band edge is sufficiently oxidizing to catalyse the methanol-to-CO_2 back-oxidation reaction.

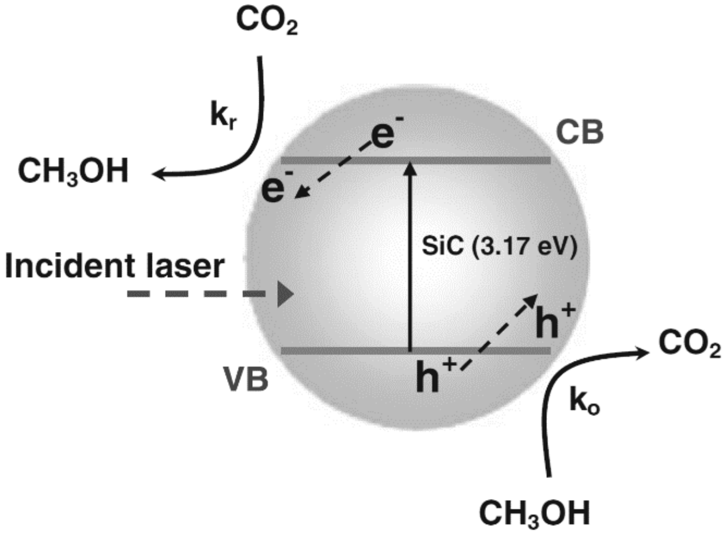

Fig. 2.2 Representation of the forward photoreduction and competing backward photooxidation reactions. Reproduced from [63].

In a more elaborate study, Liu et al. [109] also reported superior photocatalytic performance of monoclinic over tetragonal $BiVO_4$ for the photocatalytic CO_2 reduction to fuels. Their work extended to study the effects of illumination intensity on product selectivity (Table 2.1), where they found that under high-intensity irradiation (300W Xe-arc lamp – Table 2.1), ethanol was the major product obtained by dimerization and the methanol yield was almost negligible. At high intensity, more photogenerated charge carriers are generated, leading to a large concentration of C1 intermediate species bound to the $BiVO_4$ surface, which dimerize to form ethanol. Adding a UV cut-off filter to the high-intensity lamp drastically reduced the ethanol yield (Table 2.1), which indicates that poor visible-light-responsiveness of $BiVO_4$ still exists, and this study necessitates further investigation on how to extend it further across the entire visible spectrum. Under low-intensity illumination (36W fluorescent lamp), comparable amounts of methanol and ethanol were produced. Recyclability tests on $BiVO_4$ for the photocatalytic conversion of CO_2 into methanol demonstrated excellent reusability, with no measurable degradation in catalytic performance up to 5 cycles of reaction. The superior photocatalytic behaviour of the monoclinic $BiVO_4$ was explained by Liu et al. [109] as follows: the local electronic environment around the Bi^{3+} cation has greater asymmetricity in the monoclinic phase than in the tetragonal phase, resulting in the cation bearing greater lone pair character in the monoclinic phase; this facilitates the formation of a Bi…O bond with CO_3^{2-} (i.e. dissolved form of CO_2), which allows efficient transfer of photoexcited electron from V_{3d} orbitals (CB) to the adsorbed CO_3^{2-}.

	300W Xe-arc lamp (Ethanol)		**36W fluorescent lamp**	
Phase	**Vis (UV filter present)**	**UV/Vis (UV filter absent)**	**Ethanol**	**Methanol**
Monoclinic	21.6	406.6	2.3	1.8
Tetragonal	1.1	4.9	0.6	0.6

Table 2.1 Ethanol yields (μmol/hr) for both phases of BiVO4 under 300W Xe-arc lamp in the presence (Vis) and absence (UV/Vis) of a UV filter, and methanol/ethanol yields (μmol/hr) for both phases of BiVO4 under 36W fluorescent lamp

2.2.2 Bismuth (III) tungstate (Bi_2WO_6)

Bismuth tungstate is another well-established photocatalyst for photocatalytic reduction of CO_2 to methanol, and this catalyst has been nanoengineered to synthesise an extraordinary array of nanostructured photocatalysts. Bulk Bi_2WO_6 is typically synthesized by traditional solid-state reaction (SSR) route, and several groups have synthesized various nanostructured versions of Bi_2WO_6, that have two advantages over its bulk counterpart: (a) an increased surface area, which offers abundant active catalytic sites for greater reactants' adsorption/reaction and (b) a shorter charge migration distance to the catalyst surface which reduces the electron-hole recombination rate, leading to enhanced photocatalytic activity. The various nanostructured versions of Bi_2WO_6 are atomically-thin single-unit-cell layers, ball-flower-like nanoplates, ultrathin square nanoplates, hollow microspheres (HMS), hierarchical hollow microspheres (HHMS) and g-C_3N_4/Ag co-modified microsphere, summarised in Table 2.2.

2.2.2.1 Photocatalytic reduction of CO_2 to methanol

The photocatalytic CO_2-to-methanol conversion yield from the various Bi_2WO_6-based nanostructures and heterostructures are summarised in Table 2.2.

No.	Nanostructure	Precursors	Synthesis procedure	Methanol Formation Rate	Ref.
1	Atomically-thin single-unit-cell Bi_2WO_6 layers	$Bi(NO_3)_3 \cdot 5H_2O$, $Na_2WO_4 \cdot 2H_2O$, sodium oleate	$Bi(NO_3)_3 \cdot 5H_2O$ and sodium oleate vigorously stirred in water to form a lamellar Bi-oleate hybrid complex (the oleate ions interact with Bi^{3+} via self-assembly process). Next, Na_2WO_4 added in followed by hydrothermal treatment (140 °C for 24 h)	451.7 μmol g^{-1} (after 5 hrs); 3- and 125-times higher than Bi_2WO_6 nanocrystals & bulk Bi_2WO_6 respectively	[110]
2	Ball-flower-like Bi_2WO_6 nanoplates	$Bi(NO_3)_3 \cdot 5H_2O$, $Na_2WO_4 \cdot 2H_2O$, HNO_3	$Bi(NO_3)_3 \cdot 5H_2O$ and $Na_2WO_4 \cdot 2H_2O$ dissolved in HNO_3 and deionized water respectively; both solutions mixed dropwise, stirred vigorously, followed by hydrothermal treatment (160 °C for 20 h)	None; only CO detected	[111]
3	Ultrathin square Bi_2WO_6 nanoplates	$Bi(NO_3)_3 \cdot 5H_2O$, $Na_2WO_4 \cdot 2H_2O$, HNO_3, $NH_3 \cdot H_2O$, $C_{18}H_{37}N$	Generally same as above, except for addition of 1 mL $C_{18}H_{37}N$, pH adjustment to ~ 7 with $NH_3 \cdot H_2O$ and hydrothermal treatment at 200°C for 20 h	None; only CH_4 detected	[112]
4	Bi_2WO_6 hollow microspheres (HMS)	BiOBr solid microspheres, $Na_2WO_4 \cdot 2H_2O$	BiOBr solid microspheres stirred in Na_2WO_4 solution, followed by hydrothermal treatment (160 °C for 24 – 48 h)	32.6 μmol g^{-1}; 25.5 times higher than bulk Bi_2WO_6	[113]
5	conducting polymers-modified Bi_2WO_6 hierarchical hollow microspheres (CP-modified Bi_2WO_6 HHMS)	$Bi(NO_3)_3 \cdot 5H_2O$, PVP, ethylene glycol (EG), $Na_2WO_4 \cdot 2H_2O$	**BiOBr**: $Bi(NO_3)_3 \cdot 5H_2O$ and PVP added slowly to EG solution with ultrasonic treatment and magnetic stirring, followed by hydrothermal treatment (120 °C for 12 h) **HHMS**: BiOBr suspended in Na_2WO_4 solution, stirred followed by hydrothermal treatment (160 °C for 36 h) **CP-modified HHMS**: HHMS stirred in ethanol placed in ice bath, monomer added and stirred at 0 °C, then $HCl/FeCl_3$ mixture added dropwise. Resulting mixture stirred (6 h @ 0 °C), followed by washing, filtering, drying	**Methanol**: 56.5 μmol g^{-1} (4 hrs) **Ethanol**: 20.5 μmol g^{-1} (4 hrs) 2.8 and 2.5 times higher than bulk Bi_2WO_6 respectively	[114]
6	g-C_3N_4/Ag co-modified Bi_2WO_6 microsphere	$Bi(NO_3)_3 \cdot 5H_2O$, $Na_2WO_4 \cdot 2H_2O$, AgNO3, Melamine, Acetic acid,	**Microsphere**: $Na_2WO_4 \cdot 2H_2O$ dissolved in dilute acetic acid solvent, $Bi(NO_3)_3 \cdot 5H_2O$ added next under stirring, followed by hydrothermal treatment (160 °C for 12 h) **Ag-modified Microsphere**: Photodeposition method – AgNO3 solution added to Microsphere dispersion under vigorous stirring, followed by UV irradiation **g-C_3N_4/Ag co-modified Microsphere**: g-C_3N_4 and Ag-modified microsphere added to methanol, ultrasonicated and stirred followed by filtering, washing, and drying	None; photocatalysts used for dye degradation only	[115]

Table 2.2 Synthesis procedure and methanol production yield from various nanostructures and heterostructures of Bi_2WO_6

2.2.3 Copper (II) ferrite ($CuFe_2O_4$)

Copper ferrite ($CuFe_2O_4$) is a well-known catalyst that has been extensively used in numerous fields such as the synthesis of spiro-pyrimidine scaffolds [116], dye degradation [117], water splitting [118], gas sensing [119-120] and CO_2 photocatalytic reduction to methanol [121]. The crystallographic structure and active catalytic surface area of $CuFe_2O_4$ depends on the chosen synthesis procedure and it can crystallize either in the tetragonal or cubic phase due to the Jahn–Teller effect [122]. $CuFe_2O_4$ in the tetragonal structure is stable under ambient conditions (i.e. room temperature) and it is converted into the cubic phase at a temperature above 360 ^oC. The photocatalytic activity of tetragonal $CuFe_2O_4$ is much better than cubic $CuFe_2O_4$ [123]; hence, numerous synthesis methods like sol-gel [119, 124], co-precipitation [117, 124], microwave-assisted co-precipitation [125] and solid-state reaction [120, 124] have been used to synthesize tetragonal-phase $CuFe_2O_4$.

2.2.3.1 Photocatalytic reduction of CO_2 to methanol

Unfortunately, there is a dearth of CO_2 reduction studies using this stable, recyclable material. Uddin et al [121] synthesized $CuFe_2O_4/TiO_2$ heterostructure (at 1:1 weight ratio by adopting sol–gel synthesis method for preparing $CuFe_2O_4$, followed by a high-temperature calcination with TiO_2.

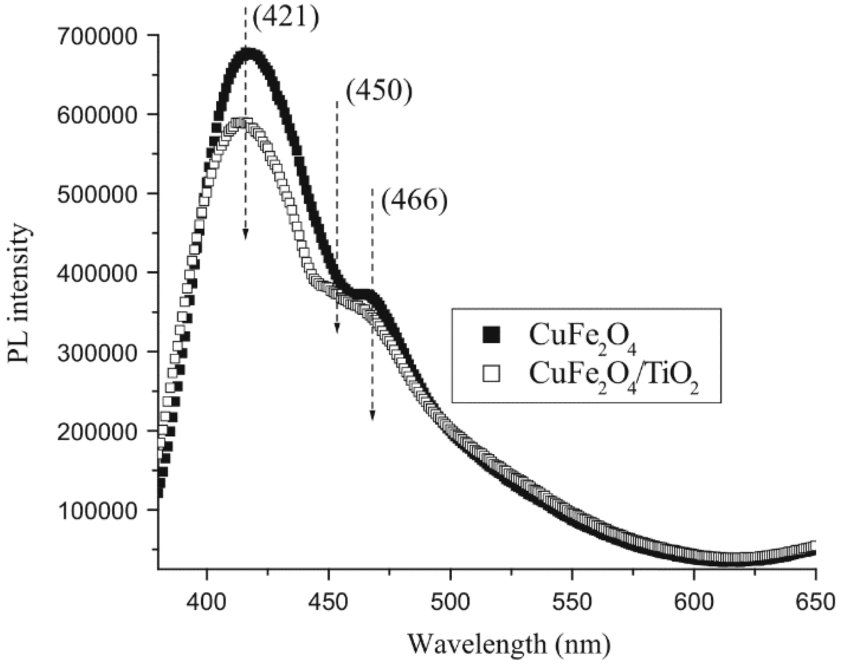

Fig. 2.3 PL emission spectra of prepared photocatalysts; excitation at 350 nm. Reproduced from [121].

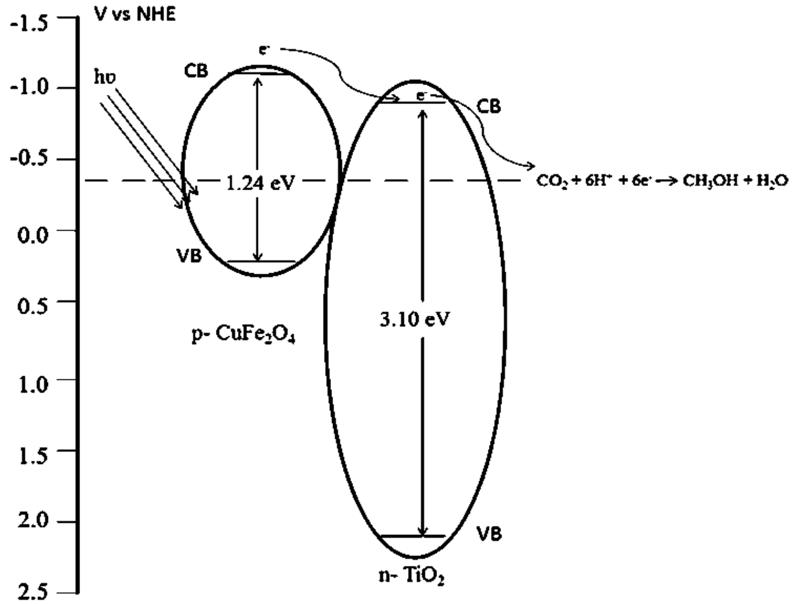

Fig. 2.4 The mechanism of enhanced charge separation over $CuFe_2O_4/TiO_2$ heterojunction – electrons excited from VB → CB ($CuFe_2O_4$), then rapidly swept across interface to CB (TiO_2) which prevents their recombination with VB ($CuFe_2O_4$) holes, thus enhancing carrier lifetime. Reproduced from [121].

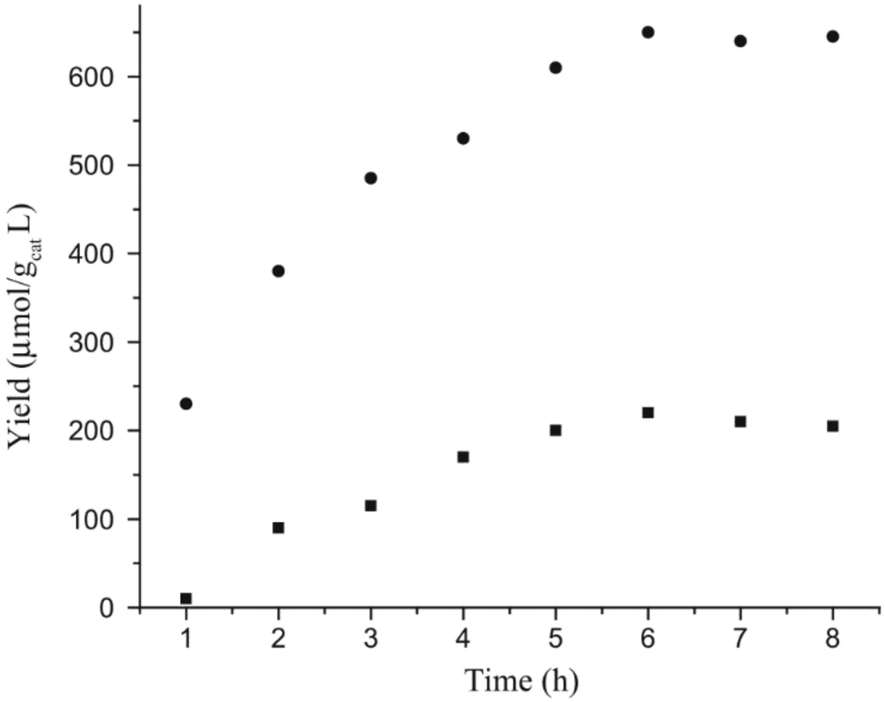

Fig. 2.5 Methanol yield of $CuFe_2O_4$ (filled square) and $CuFe_2O_4/TiO_2$ (filled circle); Reaction conditions: 8 hours irradiation under visible light (light intensity ~ 240 W/m^2) at room temperature. Reproduced from [121].

Photocatalyst properties	$CuFe_2O_4$	$CuFe_2O_4/TiO_2$
Band gap (eV)	1.24	2.61
Surface area ($m^2\ g^{-1}$)	1.4837	1.9791
Average pore diameter (nm)	3.36	25.52
Specific pore volume ($cm^3\ g^{-1}$)	0.0012	0.0013
Methanol yield (µmol/g-cat L)	220	651

Table 2.3 Comparison of optical, structural and morphological properties of $CuFe_2O_4$ and $CuFe_2O_4/TiO_2$

The reduced PL intensity (Fig. 2.3) for $CuFe_2O_4/TiO_2$ catalysts compared to $CuFe_2O_4$ is caused by the hindered electron–hole recombination as electrons and holes are swept in opposite directions (Fig. 2.4) at the $CuFe_2O_4/TiO_2$ interface. Therefore, TiO_2 loading on $CuFe_2O_4$ promotes charge carrier separation, resulting in higher CO_2 reduction efficiency and higher methanol formation rate (Fig. 2.5). The mesoporous characteristics of $CuFe_2O_4$ and $CuFe_2O_4/TiO_2$ samples are summarised in Table 2.3, and this structure was achieved not by using any surface directing agents, but rather simply by controlling the hydrolysis process.

2.2.4 Sodium niobate ($NaNbO_3$)

Perovskite photocatalysts such as niobates, titanates and strontates are another well-known class of semiconductor photocatalytic materials, of which sodium niobate ($NaNbO_3$) is the most extensively studied (see Table 2.4). $NaNbO_3$ exists in cubic and orthorhombic crystal phases and they can be synthesized either by solid state reaction (SSR) yielding bulk photocatalyst, or by various hydrothermal techniques resulting in an impressive array of exotic nanostructures (nanocube, nanorods, nanowire etc) [126, 127]. The advantages of nanostructured $NaNbO_3$ over its bulk counterpart are: increased surface area which enhances CO_2 adsorbability and lowered charge recombination rate, both of which are highly reminiscent of Bi_2WO_6.

Besides nanostructuring, several $NaNbO_3$-based bulk composites, like $CdS/NaNbO_3$ and $g\text{-}C_3N_4/NaNbO_3$ have lower charge recombination rate owing to heterostructure formation [127, 128]. Also, nitrogen-doped $NaNbO_3$ (N-doped $NaNbO_3$) has been synthesized to enhance the visible light responsiveness through the formation of impurity states in the forbidden zone [129]. Lastly, $NaNbO_3$ has also been loaded with various co-catalysts such as Cu, Pt, Au etc and applied for various photocatalytic applications [130-132].

	Photocatalyst Name	Catalytic properties	Photocatalytic performance	Ref.
Different crystallographic phases	cubic-$NaNbO_3$ (with 0.5 wt% Pt)	3.29 eV, 28.6 $m^2 g^{-1}$	H_2 evolution = 127 mol/hr CH_4 evolution = 0.486 mol/hr	[133]
	orthorhombic-$NaNbO_3$ (with 0.5 wt% Pt)	3.45 eV, 26.4 $m^2 g^{-1}$	H_2 evolution = 72.3 mol/hr CH_4 evolution = 0.245 mol/hr	
Co-catalyst loading	Cu/$NaNbO_3$	3.3 eV	Improved H_2 evolution for low Cu loading; worsened for high Cu	[131]
	Pt/$NaNbO_3$	$NaNbO_3$ NC: $NaNbO_3$ NW: Pt/$NaNbO_3$ NC: Pt/$NaNbO_3$ NW: } band gap & surface area not given	$NaNbO_3$ NC: 0.5 mol/hr $NaNbO_3$ NW: 3.2 mol/hr Pt/$NaNbO_3$ NC: 1.1 mol/hr Pt/$NaNbO_3$ NW: 26.6 mol/hr	[126]
	Au/$NaNbO_3$	Au/$NaNbO_3$: -- $NaNbO_3$ (100 oC) : 7 m2 g-1, 3.4 eV $NaNbO_3$ (150 oC) : 9 m2 g-1, 3.3 eV $NaNbO_3$ (200 oC) : 13 m2 g-1, 3.2 eV $NaNbO_3$ (250 oC) : 16 m2 g-1, 3.1 eV	**MG dye degradation rate (a.u.)** Au/$NaNbO_3$: 1980 $NaNbO_3$ (100 °C) : 90 $NaNbO_3$ (150 °C) : 198 $NaNbO_3$ (200 °C) : 220 $NaNbO_3$ (250 °C) : 495 TiO_2 (P25) : 495	[130]
	Others/$NaNbO_3$ (Fe, Ni, Co, Ag)	$NaNbO_3$: 3.34 eV Fe/$NaNbO_3$: 3.2 eV, 2.29 eV, 1.48 eV Ni/$NaNbO_3$: 3.62 eV Co/$NaNbO_3$: 3.16 eV, 2.38 eV, 1.60 eV Ag/$NaNbO_3$: 3.34 eV, 1.08 eV	**H_2 evolution (μmol)** $NaNbO_3$: 160 Fe/$NaNbO_3$: 118 Ni/$NaNbO_3$: 72 Co/$NaNbO_3$: 80 Ag/$NaNbO_3$: 192	[132]
Heterostructure formation	CdS/$NaNbO_3$	$NaNbO_3$: 3.35 eV, 7.18 $m^2 g^{-1}$ CdS: 2.60 eV, 9.61 $m^2 g^{-1}$ CdS/$NaNbO_3$: 2.95 eV, 77.0 $m^2 g^{-1}$	**MB dye degradation rate (min^{1})** $NaNbO_3$: 9.15 x 10^{-5} CdS: 1.07 x 10^{-2} CdS/$NaNbO_3$: 6.33 x 10^{-2}	[128]
	g-C_3N_4/$NaNbO_3$	$NaNbO_3$: 12.0 $m^2 g^{-1}$ g-C_3N_4: 6.5 $m^2 g^{-1}$ g-C_3N_4/$NaNbO_3$: 10.7 $m^2 g^{-1}$	**CH_4 evolution (μmol/g/hr)** Pt/$NaNbO_3$: Trace Pt/g-C_3N_4 : 0.8 Pt/g-C_3N_4/$NaNbO_3$: 6.4	[127]

Table 2.4 Comparison of hydrocarbon yields of several composites of $NaNbO_3$ photocatalysts

2.2.4.1 Photocatalytic reduction of CO_2 to methanol

Like copper ferrite, few CO_2 reduction studies have been reported using this high-performance photocatalyst. Fresno et al [134] have used $NaNbO_3$, $NaTaO_3$ and TiO_2 for photocatalytic CO_2 reduction and obtained various hydrocarbon products as per Fig. 2.6. Without using metal co-catalysts, the product selectivity is geared towards CO instead of highly-reduced carbon products like CH_3OH and CH_4. However, on a positive note, the competition for electrons between CO_2 reduction and water-splitting is interestingly shifted towards the former, as H_2 evolution is suppressed whilst CO production is enhanced in using perovskite photocatalysts rather than TiO_2. The slightly higher carbon product evolution using $NaTaO_3$ instead of $NaNbO_3$ is ascribed to the conduction band electrons of $NaTaO_3$ having a higher energy (more negative reduction potential) than those in $NaNbO_3$.

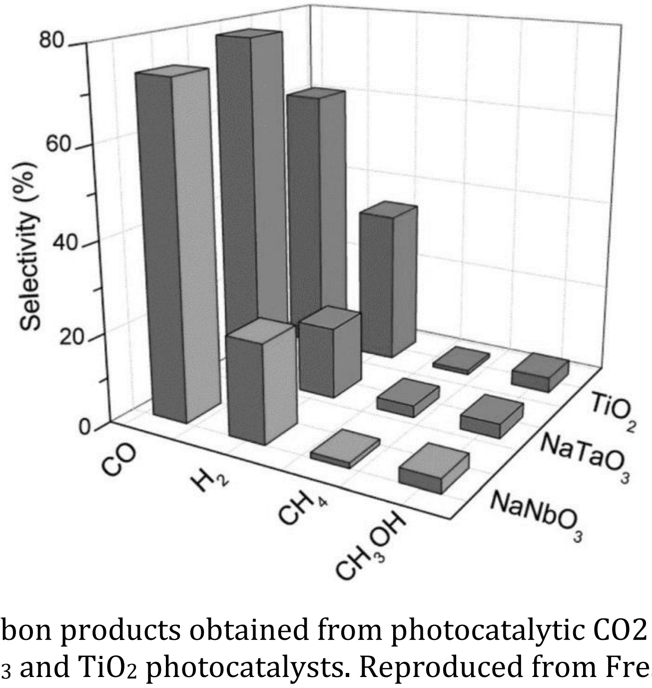

Fig. 2.6 Hydrocarbon products obtained from photocatalytic CO2 reduction using $NaNbO_3$, $NaTaO_3$ and TiO_2 photocatalysts. Reproduced from Fresno et al [134].

2.2.5 Closing remarks

This section touches upon the research advances made in improving the material characteristics of semiconductor metal oxide photocatalysts, which are crucial for developing a technology based on photocatalytic CO_2 reduction to value-added hydrocarbon products, especially methanol. In principle the development of this process could be potentially a revolutionary solution to tackle two pressing global issues in energy and environment, where the much needed energy is generated using ever increasing excessive levels of atmospheric CO_2, which is a major threat for the earth due to its active contribution to global warming. In addition, this technology helps to harvest the abundant solar energy in the form of transportable and easily storable value added high energy density fuel using menacing atmospheric CO_2 as the raw material.

Although many value added hydrocarbons can be generated using this process, this section mainly focuses on semiconductor metal oxide photocatalysts developed and improvised for photocatalytic reduction of CO_2 into methanol. Methanol is a fuel with higher energy density, easier transportability, and capable of less cumbersome and direct conversion into electrical energy, compared to other hydrocarbon products. The photocatalytic performance of a material can be enhanced by optimizing the key properties like increasing the adsorption of the reactants on the catalyst by increasing the surface area, improving the visible light sensitivity, lowering the rate of photogenerated charge recombination. It is rather hard to find a catalyst that possesses all these positive attributes simultaneously. Hence novel materials need to be engineered to improve the weakness, while harnessing the natural positive attributes of a catalyst. These material engineering techniques include synthesizing nanostructured material, transforming into different crystal phases, annealing, doping with other metals, forming heterojunction with composite materials, and the various combinations of these strategies. Several of these improvisations on different classes of metal oxide semiconductor photocatalysts to improve photocatalytic CO_2 reduction to methanol have been discussed in this section.

2.3 Review of experimental parameters

Besides the nature of photocatalysts used, several experimental parameters such as temperature, pressure, solvents used, energy and wavelength of the radiation, addition of scavengers, addition of H_2 gas, presence of dissolved oxygen, catalyst loading systems and catalyst concentration play a crucial role in the photocatalytic production yield and the selectivity of the reaction product. The success of the photocatalytic reaction leading to the conversion of CO_2 into methanol depends on determining the optimal value of experimental parameters that enhance the total methanol production yield. However, it is not always easy to determine the optimal experimental parameters for a particular photocatalytic reaction mediated through a specific photocatalyst. If we take temperature as the experimental parameter for instance, lowering the temperature favourably increases the availability of CO_2 molecules due to increased CO_2 solubility, but the reaction rate constant and the collision frequency decrease, which is an undesirable factor. Hence, it is readily apparent that there are many factors and mechanisms, competing with one another in the same reaction system, leading to a particular end product. The net effect depends on the aggregate of the influence of each parameter on the different mechanisms in the same reaction system. Hence each reaction system with a particular catalyst has a unique set of optimum experimental parameters that enhances the yield of a particular reaction products. This complexity opens the door for novel research endeavours in the photocatalytic conversion of CO_2 into methanol in terms of discovering the optimum operating conditions and explaining the experimental results with possible theoretical models.

There are two kinds of experimental parameters pertaining to photocatalytic conversion of CO_2 into methanol: the parameters such as the concentration of CO_2 and the photocatalyst availability are called dependent parameters because they are not directly controllable, rather they change with variations of other parameters like temperature and pressure. On the other hand, the experimental parameters that can be easily controlled and do not change with the change of other parameters are known as independent parameters. Since the CO_2 conversion process is highly complicated, there is no simple one-to-one correlation between the set of independent and dependent parameters. Certain dependent parameters (like CO_2 availability) are affected by multiple independent, controllable parameters such as temperature, pressure and solvent used; likewise, certain independent, controllable parameters (like temperature) influence several dependent parameters like reaction constant, CO_2 and Catalyst availability. The various dependent and independent parameters, and their inter-dependences are presented in Table 2.5.

Dependent Variables Independent Variables	CO_2 availability	Hole conc.	Electron conc.	Catalyst availability	Photon availability	Rate constant
Temperature	✓			✓		✓
Pressure	✓					
Solvent Used	✓	✓				✓
Irradiation					✓	
Addition of Hole scavenger		✓				
Catalyst loading system				✓		
Catalyst Concentration				✓	✓	
Dissolved O_2			✓			

Table 2.5 Interrelationships between independent and dependent variables affecting photocatalytic CO_2 reduction to methanol

In this upcoming section we will be focusing on a few selected parameters, in the following sequence: temperature, solvent used, illumination settings, addition of hole scavenger and catalyst concentration.

2.3.1 Temperature

Like any chemical reaction, photocatalytic CO_2-to-methanol conversion is influenced by the reaction temperature; hence, choosing the optimal temperature is not easy since the temperature influences the methanol yield in 4 different ways, as summarised in Table 2.6.

Effect of Temp. change Temperature	CO_2 solubility	Reactant Adsorption	Catalyst availability	Reaction constant
Increase	**Decrease**	**Decrease**	**Increase**	**Increase**
Decrease	**Increase**	**Increase**	**Decrease**	**Decrease**

Table 2.6 Effect of temperature on various factors indirectly affecting the photocatalytic CO_2 reduction rate

Firstly, the temperature affects the amount of CO_2 that can dissolve in water, and decreasing the temperature raises the solubility of CO_2 in water. This increased amount of dissolved CO_2 in water can enhance the methanol production yield. In general, the solubility of CO_2 in water increases by approximately 2.5 times when water is cooled from 25 ˚C to 0 ˚C, which results in a 2.5-times increase of dissolved CO_2. The corresponding increase in the methanol production yield is based on Equation 1, where the methanol production is stoichiometrically-related to the CO_2 availability.

$$\mathbf{CO_2 + 6H^+ + 6e^- \rightarrow CH_3OH + H_2O \quad (1)}$$

Secondly, the temperature influences the ease of reactants' adsorption onto the surface of the catalyst. Under low temperature conditions, reactants absorb more readily onto the catalytic surface due to lower thermal agitation. It is quite natural that the photocatalytic reaction rate increases with the amount of reactants adsorbed on the catalyst surface.

Thirdly, it affects the rate of product desorption, thus determining the degree of catalyst poisoning and, consequently, catalyst availability. At lower temperatures, the reactive intermediates and products are more likely to remain adsorbed on the catalyst surface, impeding any further catalytic activity and this adverse effect is called catalyst poisoning. Consequently, fresh reactants are unable to adsorb on the surface owing to a lack of vacant catalytic adsorption sites and this leads to the slowing down of the photocatalytic CO_2 reduction. Lastly, another adverse effect of lower temperature on the photocatalytic CO_2 reduction process is that it leads to a decrease in the reactants' diffusion rates and collision frequencies, resulting in lower reaction rate constant for methanol production. These four effects of temperature on the photocatalytic reaction suggests that there is an optimum temperature at which the adverse effects taking place at high and low temperatures can be minimized, without compromising on the positive effects.

The temperature dependence on the production yield of value added hydrocarbons by photocatalytic CO_2 reduction reaction was studies by many research groups. Mei Gui et al [135] reported that the photocatalytic reaction rate rises with temperatures, which they attribute to the increased rate of molecular diffusion and collision frequency of the reactants; this helps to fulfil the requisite activation energy for the photocatalytic reaction to proceed. Anpo et al. [136] discovered that the yields of CO_2 reaction products like CH_3OH, CH_4 and CO were greater at 323 K than 275 K using ultraviolet irradiation. This agrees with the trend observed by Slamet et al. [137], who investigated the temperature dependence of CO_2 photoreduction in the temperature range of 43 °C to 100 °C and concluded that high temperatures improve methanol yield owing to enhanced product desorption from catalytic surfaces; their methanol yield after 6 hours of illumination was greater at 100 ˚C than 43 ˚C. At high temperatures, products desorb more easily, and they deduce that product desorption is the rate determining step from the activation energy values of the photocatalytic reaction.

Koci et al [138] attributed an increase in reaction rate at elevated temperatures to increased molecular diffusion and collision, and reported that the optimal temperature needed for CO_2 reduction generally lies between 293 and 353K, with reduced photocatalytic activity outside this temperature range [139], which they attributed to the exothermic adsorption of reactants. Yamashita et al. [140] observed increased CH_4 and CH_3OH yield under UV illumination at 323 K relative to 275K, from which they confirmed that the photocatalytic CO_2 reduction rate (in a system using anchored titanium oxide catalysts), is accelerated at temperatures higher than 275 K.

2.3.2 Solvent used

The solvent medium used for the photocatalytic reduction of CO_2 has several functions, such as acting as a hydrogen source, hole scavenger and a medium to dissolve CO_2. The pH is a major factors to be considered when choosing a solvent.

The pH of the solvent is also crucial in semiconductor-based photocatalytic reactions because it alters the theoretical reduction potential of CO_2 due to varied proton concentration and consequently influences the photocatalytic reaction process, based on the following Equation 1, wherein the methanol yield depends on the H^+ concentration. There have been a few works investigating the effects of acidic, basic and neutral solvents as a medium in the photocatalytic CO_2 reduction.

2.3.2.1 Acidic

In acidic conditions, the proton concentration is quite high (low pH) and this leads to a lower theoretical CO_2 reduction potential [141], which is more favorable to reduce CO_2

to CH_3OH. On the contrary, if the proton concentration were even higher, water splitting would preferentially occur over CO_2 reduction, leading to H_2 production.

2.3.2.2 Neutral and Alkaline

Between neutral and alkaline medium, there are conflicting reports about the optimal solvent conditions that favor CO_2 reduction process. In general, the increased solubility of CO_2 in the alkaline medium leads to the enhancement of the methanol production rate. However, the dissolved CO_2 in alkaline media creates carbonates or bicarbonates, which tend to be more difficult to reduce than even CO_2. Neatu et al [142] proposed that even though higher pH increases the CO_2 solubility in water, this does not necessarily work favourably for CO_2 reduction, because under these conditions, more carbonates and/or bicarbonates are formed (Equations (2) and (3)).

$$\mathrm{CO_2 + OH^- \longrightarrow HCO_3^-} \qquad (2)$$

$$\mathrm{HCO_3^- + OH^- \longrightarrow CO_3^{2-}} \qquad (3)$$

$$\mathrm{CO_3^{2-} + h^+ \longrightarrow CO_3^{\bullet -}} \qquad (4)$$

$$\mathrm{2CO_3^{\bullet -} \longrightarrow 2CO_2 + O_2 + 2e^-} \qquad (5)$$

$$\mathrm{2H_2O + 4h^+ \rightarrow O_2 + 4H^+} \qquad (6)$$

$$\mathbf{CO_2 + 6H^+ + 6e^- \rightarrow CH_3OH + H_2O} \qquad (\mathbf{7})$$

As carbonates or bicarbonates are even more difficult to reduce than CO_2, the advantages of having increased CO_2 solubility in water cannot be harnessed. Moreover, as carbonates and bicarbonates are negatively-charged, they function as good hole-quenchers, by donating electrons to the photocatalyst, as seen in Equations (4) and (5). Hence, according to Neatu et al [142], in this process, the outcome is the evolution of oxygen (Equation (6)) rather than the real reduction of CO_2 (Equation (7)). The reduction potentials of various carbonaceous species (CO_2, H_2CO_3, CO_3^{2-}) have been compiled by Tahir et al [143].

The above perspective was substantiated by the work of Gonell et al [144], who studied the photocatalytic reduction of CO_2 using Cu-TiO_2 as a photocatalyst in the medium of aqueous suspensions of NaOH (0.1 M) under UV irradiation. They reported that the addition of NaOH led to the production of only a trace of CO and did not produce any liquid phase products like methanol or formic acid. Their work concluded that hydroxide salts are of limited benefit in terms of increasing the dissolved CO_2 amount in the form of carbonate and bicarbonate ions.

Quite contrary to the above finding, Tseng et al [145] noted that an alkaline medium was beneficial in the photoreduction of CO_2. They observed a substantial increase of methanol yield with the addition of NaOH, which they attributed to 2 factors: (1) the strong hole-scavenging ability of OH^- ions [146] in aqueous solution helps to reduce the electron–hole recombination rate and maximizes the lifetime of free electrons, which considerably helps the CO_2 reduction process, (2) the higher solubility of CO_2 in aqueous NaOH solution than in pure water.

2.3.3 Irradiation settings

2.3.3.1 Wavelength of irradiation source

In the process of photocatalytic CO_2 reduction, the wavelength of the incident radiation plays a substantial part in affecting the production yield of the reaction products. For photocatalysis to occur, the incident radiation should at least have the threshold photon energy [147], which exceeds the photocatalyst band-gap energy (E_g). This is essential to transfer electrons from the valance band to the conduction band. Matthews and McEvoy [148] demonstrated that the threshold wavelength alone is often insufficient and having an incident photon energy that is in excess of the threshold energy drastically improves the CO_2 reduction rate. They studied CO_2 reduction with TiO_2 as a photocatalyst under the incident radiation of different wavelengths and reported that light with shorter wavelength (254 nm) is significantly more effective (60 times) than longer wavelength light (350 nm) for CO_2 reduction, even though both illumination sources satisfy the threshold wavelength criteria. Koci [149] studied the wavelength effect on photocatalytic reduction of CO_2 using Ag/TiO_2 photocatalyst and reported that the concentrations of the main products (CH_4 and CH_3OH) were higher with the radiation of wavelength 254 nm lamp than with the radiation of wavelength 365 nm while no products were observed with an illumination wavelength of 400 nm as the catalyst was not active under visible light.

2.3.3.2 Intensity of irradiation source

Intensity of an illumination source is proportional to the number of photons falling on a unit area in unit time. In a photocatalytic process, the generation of the crucial electron-hole charge pair depends on the number of incident photons and thus the methanol yield is proportional to the intensity of the incident radiation. The geometrical design of the photoreactor, the lamp-to-photoreactor distance and usage of fiber optics are all appropriate techniques to maximize the radiation intensity on the reaction medium, in addition to the obvious method of using a higher intensity radiation source.

2.3.4 Addition of hole scavengers

The addition of a hole scavenger [150], which is an independent, controllable experimental parameter, controls the density of holes present in the aqueous solution. Kamat [151] noted the importance of scavenging one type of charge carrier, so as to make surplus the opposite charge type and allow it to accumulate within the photocatalyst particles. Hence, hole scavengers reduce the electron density, thereby suppressing the charge carrier recombination rate, converting the system into a reducing condition [152] and improving the photocatalytic reaction efficiency. In the case of CO_2 reduction, electrons reduce CO_2 molecules; hence, the scavenging of holes to reduce the hole density is vital to ensure that an appreciable electron density builds up for rapid photocatalytic CO_2 reduction. Na_2SO_3 is typically used as a hole scavenger [153] to consume the valance band holes generated in the photocatalyst, based on the mechanism in Equation (8). Also, the longer decay time of surface electrons facilitates the reduction of CO_2 [154]. Reli et al [72] have investigated the consequence of Na_2SO_3 addition for photocatalytic CO_2 reduction in an alkaline medium, and have observed an increase in the methanol yield using both NaOH and NH_4OH, as summarised in Table 2.7.

$$2(SO_3^{2-} + h^+) \longrightarrow 2SO_3^{\bullet -}(+H_2O) \longrightarrow SO_4^{2-} + SO_3^{2-} + 2H^+$$
$$\mathbf{OR} \longrightarrow S_2O_6 \qquad (8)$$

Reaction conditions	Methanol yield (µmol/g-cat)
NaOH	**2.2**
NaOH + Na_2SO_3	**3.0**
NH_4OH	**0.95**
NH_4OH + Na_2SO_3	**1.55**

Table 2.7 Methanol yields under various reaction mediums (type of alkaline medium, presence/absence of hole scavengers)

2.3.5 Catalyst concentration

The concentration of photocatalyst is an important experimental parameter to be considered in the photocatalytic reduction of CO_2. When the catalyst concentration is very low, there will be insufficient active catalytic sites for CO_2 and H_2O adsorption and reduction to occur, which leads to low methanol yield. A high catalyst concentration, on the other hand, scatters the incident radiations and hinders proper illumination of the entire reaction volume. Hence, a significant proportion of the photocatalyst particles do not get activated by photons, which decreases the maximum methanol yield attained [155]. The ideal concentration of photocatalyst reported for photocatalytic CO_2 reduction is 0.1 – 1 g per 100 ml of aqueous reductant.

Liu et al [156] reported an optimal value of 0.25 g of CoPc–TiO_2 catalyst per 100 ml of NaOH aqueous medium, which gave a peak in the methanol yield and they also found that varying the catalyst concentration even slightly to 0.3 g drastically reduced the methanol yield. The same trend of drastic and sensitive effect of catalyst concentration on methanol yield was observed by Tseng et al [145], where the optimal catalyst concentration was 1 g per 100 ml. In fact, the optimal catalyst concentration depends on many other factors such as photoreactor design [157], geometry [68], and the photocatalyst scattering cross-section and hence it is recommended to initially estimate the optimal concentration prior to conducting detailed CO_2 reduction experiments. Also, the optimal catalyst concentration value should be independent of the catalyst used, provided all other experimental parameters (photoreactor design, particle size etc) are the same.

2.3.6 Closing remarks

This section focuses on various operational parameters that affect the activities of CO_2 photocatalytic reduction to methanol. Since the effect of the parameters on the photocatalytic conversion rate is sometimes controversial, it is imperative for detailed empirical and theoretical studies to better understand the detailed and precise manner in which the parameters affect this process. By optimising the operational parameters discussed in this section, the photocatalytic CO_2 conversion rate to methanol could be significantly enhanced, thus giving a major boost to this process that has been languishing inefficiently for decades.

CHAPTER 3

Experimental details

3.1 Overview

In this chapter, we present the experimental details pertaining to the choice of photocatalyst, its synthesis and the materials characterization equipment used for this study. In addition, we present the reactor setup used for photocatalytic CO_2 reduction used in this thesis.

This chapter is organised as follows:

(a) choice of photocatalyst, its synthesis and materials' characterization equipment (section 3.2), and

(b) photoreactor setup and photocatalytic experimental details (section 3.3).

3.2 Photocatalyst

3.2.1 Choice of photocatalysts

The objective of this thesis is twofold: firstly, to develop a solar-harvesting photocatalyst that can convert CO_2 to methanol using natural sunlight, and secondly, to enhance the methanol product selectivity of a reported photocatalyst. After extensive literature review and trial-and-error experimentation, we have decided upon graphitic carbon nitride (g-C_3N_4) as the solar-harvesting photocatalyst, and Ag-loaded $NaNbO_3$ as the methanol selective CO_2 reduction photocatalyst.

The suitability of each photocatalyst for CO_2 conversion to methanol is explained hereunder. As mentioned earlier, photocatalytic reduction of CO_2 can take different reaction pathways each leading to different reaction products like HCHO, CO, HCOOH, CH_3OH and C_2H_5OH. In order to selectively target any particular reaction product, like methanol in our case, the photocatalyst should be chosen in such a way that its valance and conduction band edges are compatible with the redox potential of the redox reaction that leads to the desired product. Therefore, the photo-generated charge carriers in such photocatalysts should be potent enough to catalyze the photocatalytic reaction by oxidation and reduction. Particularly, in the case of photocatalytic reduction of CO_2 to methanol, the following reactions are suggested:

$$2H_2O + 4h^+ \rightarrow O_2 + 4H^+ \qquad + 0.82\ \mathrm{V}$$

$$\mathbf{CO_2 + 6H^+ + 6e^- \rightarrow CH_3OH + H_2O \qquad - 0.38\ V}$$

As is clear from the schematic diagram depicted in Fig. 3.1, the valance band edge of g-C_3N_4 (+1.85 V) is more positive than the water splitting oxidation potential (+0.82 V) and the conduction band edge of g-C_3N_4 (-0.85 V) is more negative than the CO_2/CH_3OH reduction potential (-0.38 V). Likewise, from Fig. 3.2, the valance band edge of $NaNbO_3$ (+2.52 V) is more positive than the water splitting oxidation potential (+0.82 V) and its conduction band edge (-0.78 V) is more negative than the CO_2/CH_3OH reduction potential (-0.38 V). These band structures justify the suitability of g-C_3N_4 and $NaNbO_3$ to catalyse the photocatalytic reaction that leads to the conversion of CO_2 into methanol.

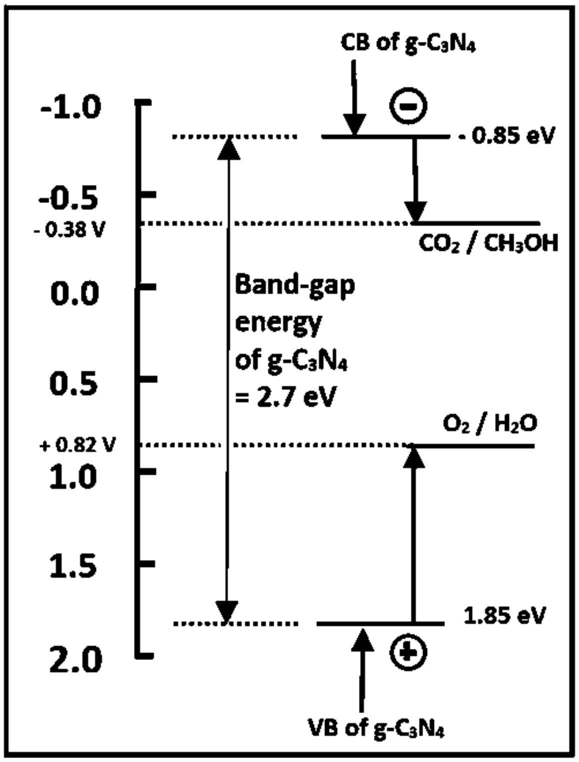

Fig. 3.1 Band edge positions of g-C3N4 [158]

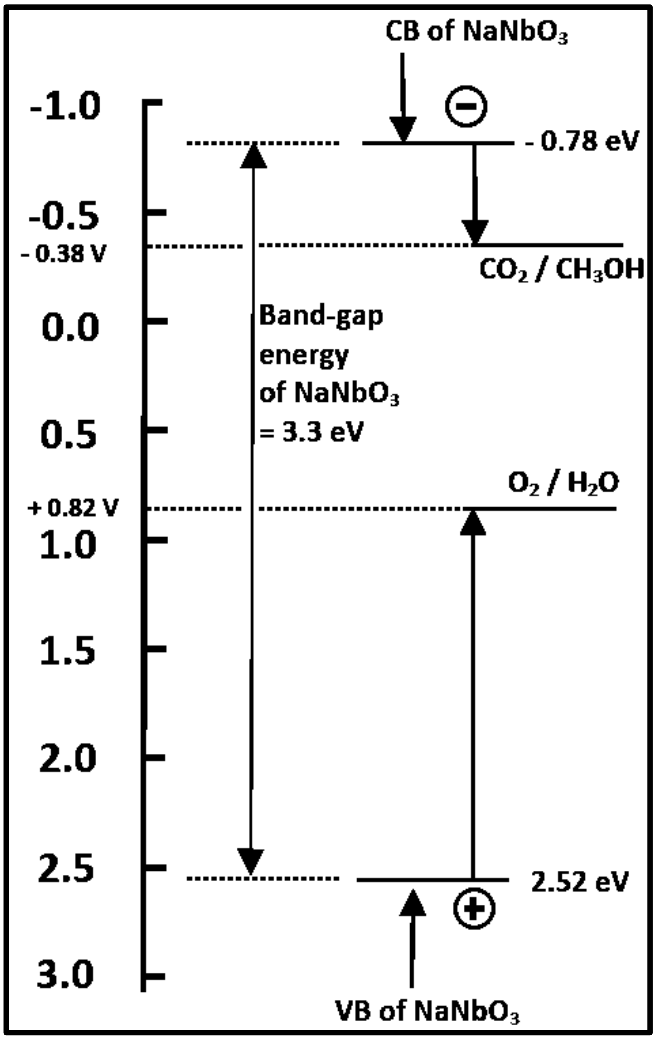

Fig. 3.2 Band edge positions of $NaNbO_3$ [159]

3.2.2 Synthesis of photocatalysts

3.2.2.1 graphitic carbon nitride

Pure graphitic carbon nitride (g-C_3N_4) was synthesized by direct pyrolysis of melamine at 500 ˚C, heated at a ramp rate of 20 ˚C/min. After maintaining the melamine at 500 ˚C for a duration of 2 hours, it was further heated to 550 ˚C at a ramp rate of 5 ˚C/min for de-amination treatment [160]. During the heating phase, the single melamine units condense into tri-s-triazine units, which subsequently condense into large sheets of graphitic carbon nitride, as shown in Fig. 3.3 [160].

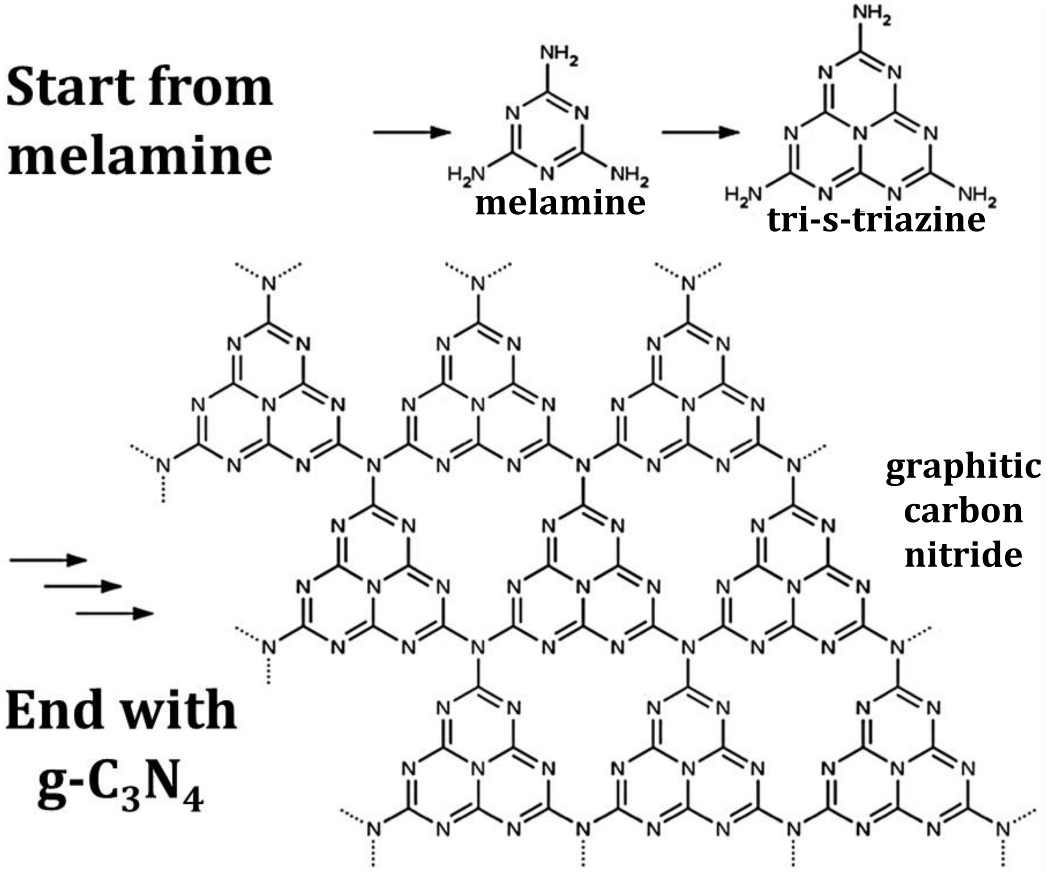

Fig. 3.3 Synthesis of graphitic carbon nitride by heating melamine precursor leading to repeated condensation

3.2.2.2 Ag-loaded $NaNbO_3$

Pure $NaNbO_3$ was synthesized by a solid state reaction process. Nb_2O_5 and Na_2CO_3 were carefully ground together using a pestle and mortar; Na_2CO_3 was taken in 5% excess with respect to the stoichiometric amount to compensate for volatilisation losses. The mixture was then heated in air in a muffle furnace at a heating rate of 10 °C min^{-1} until 900 °C, then held at 900 °C for 12 h [159], before allowing it to cool naturally to room temperature.

The Ag-loaded $NaNbO_3$ photocatalyst was prepared by a wet impregnation method starting from an aqueous solution of silver nitrate ($AgNO_3$) and the as-synthesized $NaNbO_3$. The mass content of metal ions in $NaNbO_3$ was 5%. In the first step of Ag/$NaNbO_3$ preparation, $NaNbO_3$ and the silver nitrate solution were put into a ceramic dish. The obtained suspension was stirred whilst evaporating of water. After drying the resultant powder was thoroughly ground finely. Afterwards, the dried/ground powder was placed in a high-temperature crucible and calcined at the temperature of 400 °C for 4h, before being allowed to cool naturally to room temperature.

3.2.3 Materials' characterization equipment

For the X-ray photoelectron spectra (XPS), VG scientific ESCALAB MKII spectrometer was used and in this, a dual aluminium–magnesium anode X-ray gun and a concentric hemispherical analyser using Al Kα radiation were used. FTIR (Fourier transform infra-red spectroscopy) spectra were acquired with a Thermo scientific NICOLET 6700 in an ATR mode. Raman spectra were acquired using a Horiba Jobin Yvon Modular Raman

Spectrometer, using a Stellar Pro Argon-ion laser emitting 50 mW at 514 nm (Green), with a data acquisition time of 10 s, and a total of 3 accumulations. The system was calibrated using a silicon reference before the measurement (520.5 cm^{-1}). For solid-state UV-vis spectroscopy, a Shimadzu UV-2450 UV-vis spectrophotometer was used, with $BaSO_4$ used as a reference. The measurement range and resolution are 200 – 900 nm and 0.5 nm respectively. For photoluminescence spectroscopy, a Horiba Fluorolog-3 Spectrofluorometer equipped with a broadband 450 W Xenon lamp as the excitation source was used. The crystalline phase was characterized by powder X-ray diffraction (XRD) using a Rigaku MiniFlex II diffractometer (40 kV, 30 mA with Cu Kα radiation of $\lambda = 1.5406$ Å). The data were collected in 2θ–θ scanning mode at a scan speed of 3° min^{-1} and a step-size of 0.02°. The morphology was examined using a Tescan Lyra-3 field emission-scanning electron microscopy (FE-SEM) operating at an accelerating voltage of 20 kV.

3.2.3.1 XRD

X-Ray Diffraction (XRD) is a tool used for determining the crystallographic structure, phase and lattice parameters of unknown materials. In 1912, Max von Laue discovered that crystalline samples behave like 3D diffraction gratings when an X-ray beam is incident upon them [161]. One year later, in 1913, the Bragg father-son team (William and Henry Bragg) derived the equation that now bears their name (Bragg's law) [162], by regarding a crystal as being comprised of parallel equidistant atomic planes.

To proceed, X-ray diffraction works on the principle of constructive interference when monochromatic X-rays interact with a sample. X-rays are generated by a cathode ray tube, wherein an electric current passing through a filament heats it (i.e. the filament), leading to thermionic electron ejection. The high-energy electrons impinge on a copper target, where they decelerate, and emit bremsstrahlung (braking radiation) i.e. X-rays, which are monochromatized, collimated and fired on a sample. The interaction of the incident X-rays with the sample produces constructive interference (and a strongly-diffracted X-ray beam) when the aforementioned Bragg's Law ($n\lambda = 2d \sin \theta$) is fulfilled. This law links the lattice spacing (d) of a crystalline sample to the incident X-ray wavelength (λ), the diffraction angle (θ) and the diffracted beam order (n). The basic idea of constructive interference is illustrated in Fig. 3.4 below.

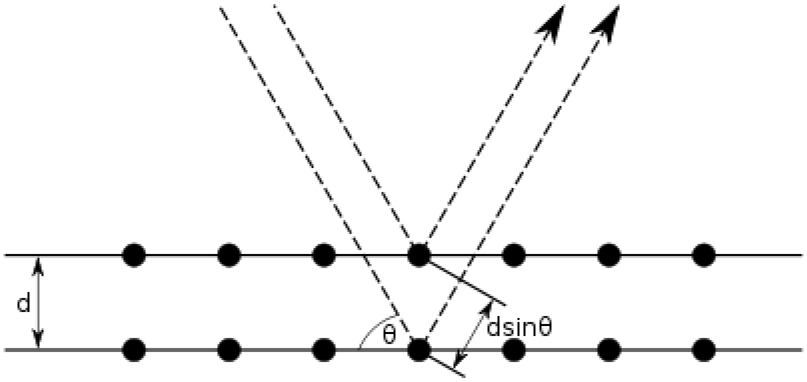

Fig. 3.4 Bragg diffraction. Two monochromatic beams strike a crystalline solid and are scattered by different atoms. The path difference of the 2 beams is 2dsinθ, leading to constructive interference if this length equals an integer multiple of incident wavelength.

The diffracted X-rays are then detected and counted, leading to a diffractogram which plots the X-ray diffraction intensity against the scattering angle 2θ. This diffractogram gives a series of peaks, wherein each peak represents x-rays diffracted from a distinct set of atomic planes characteristic of the sample. By scanning the sample through a complete angular range of values for 2θ, all possible diffraction directions of the lattice should be attained due to the random orientation of the powdered material. By comparing the diffraction peak positions against a standard crystallography database, we can identify the unknown sample, as each sample possesses a unique set of diffraction peaks [163].

3.2.3.2 SEM

The scanning electron microscope (SEM) is a powerful magnification tool that utilizes focused electrons beams to obtain information about the sample under study. It scans a focused beam of electrons on a sample of interest. Primarily, an SEM set-up comprises the following: an electron source, a long column along which electrons travel, an electron detector, a sample chamber and a computer to display the images [163].

In modern FE-SEM devices, electrons are produced by a field-emission cathode that provides well-collimated, narrow electron beams, resulting in enhanced spatial resolution, reduced sample charging and damage [165]. Electrons are produced at the top of the column by an electron gun, accelerated downwards by an applied electric potential difference and passed through a series of electromagnetic lenses and apertures to focus and collimate the electron beam, which strikes the sample surface. In the sample chamber, the sample is mounted on a stage and the electron column and sample chamber are evacuated by vacuum pumps to avoid eletron-air collisions. The position of the electron beam on the sample is moved systematically over the sample in a raster scanning manner, which enables information about a defined area on the sample to be collected [166]. Due to the various electron-sample interaction mechanisms, a number of signals are produced, including secondary and backscattered electrons, which are then detected by appropriate electron detectors [167]. These signals are then converted to images which are displayed on a computer.

3.2.3.3 XPS

X-ray photoelectron spectroscopy (XPS) is a surface-sensitive quantitative technique that measures the elemental composition, empirical formula, chemical and electronic state of elements within a material [168]. To obtain an XPS spectra, the sample under study is irradiated with a beam of collimated, monochromatic X-rays, which strikes the sample and causes photoelectron emission from it [169]. The kinetic energy and number of these ejected electrons is measured, which gives a characteristic plot of intensity against binding energy [170]. It operates under high vacuum conditions to avoid the X-rays and electrons from getting perturbed by colliding with air molecules [171].

We now elaborate on the beam-sample interaction process. When an X-ray photon strikes an atom, it can knock out an electron. The kinetic energy (KE) of the emitted electron depends upon the incident X-ray energy (hν) and the electron binding energy (BE) (energy required to remove the electron from the surface). By measuring the KE of the emitted electrons, we can obtain the BE values of the photoelectrons. From these BE values, one can determine which elements are near a material's surface, and their chemical states [172]. The most interesting feature of XPS is its ability to distinguish between the same element existing in different electronic environments. For instance, a nitrogen atom in a C-N bond is not chemically-identical to a nitrogen atom in an N-H bond, which implies that the binding energy of electrons emitted from both nitrogen atoms will be different. This is known as a chemical shift in XPS analysis. From these shifts we can identify the precise electronic environments in which a particular element (e.g. nitrogen) is located, from which we can arrive at the detailed sample composition and bonding.

3.2.3.4 UV/Vis spectroscopy

UV-Vis spectroscopy is a characterization technique for measuring the optical properties of solid/liquid samples by the transmission or reflection of light in the visible and UV region. There are 2 modes of operation: UV-VIS absorption spectroscopy, measured by transmittance, and UV-Vis diffuse reflection spectroscopy (DRS) measured by diffuse reflectance. In general, the former is used for solutions/thin films, whilst the latter is used for solid, powdered samples.

Solid powders are defined by their internal inhomogeneities. Light propagation through inhomogeneous media is very different from that through homogeneous material, because the light scatters off at various points along its path. The mathematical description of diffuse reflectance (R) is most commonly approximated by the Kubelka-Munk (KM) function, F(R):

$$\mathrm{F(R)} = \frac{(1-\mathrm{R})^2}{2\mathrm{R}}$$

Originally, the Kubelka-Munk (KM) function was developed to analyse paint-coated surfaces [173] and thus makes the following assumptions: the surface under analysis is completely flat, of infinitesimal thickness and is semi-infinite. These assumptions allow all geometric peculiarities of the inhomogeneous sample to be subsumed into one parameter, known as the scattering coefficient (s). The so-called KM function is approximately equal to the absorption coefficient. The justification for this lies in the fact that the degree of scattering is not strongly wavelength- or absorption-dependent, so the KM model considers it a constant. However, scattering does change significantly with packing density, so powdered samples must be packed as identically as possible to ensure reproducible results.

The band gap, E_g, of the materials was determined by a Tauc plot [174], which typically plots the quantity $h\nu$ (photon energy) and $(Fh\nu)^{1/n}$ on the horizontal and vertical axis respectively. The value of the exponent n depends on the nature of the electron transition. In this work, the value of $n = 2$ was used since all the semiconductor materials used exhibit direct transition. The extrapolation of the linear part of the Tauc plot to the horizontal axis gives the band gap energy of the material [174].

3.2.3.5 Photoluminescence spectroscopy

Photoluminescence (PL) spectroscopy is a non-destructive technique to probe the electronic structure of materials. The sample under study is exposed to an incident broadband excitation source, which gets absorbed by the material, i.e. electrons are photoexcitation from the ground to allowed excited state. Upon returning to the original equilibrium state, energy is released and it may (radiative process) or may not (non-radiative process) include the emission of light. It is the former process (radiative emission) that constitutes photoluminescence spectra. The energy of the emitted light (photoluminescence) relates to the difference in energy levels between the two energy states (the excited and ground state). The quantity of the emitted light is related to the relative contribution of the radiative process [175]. In semiconductors, the most common radiative transition in semiconductors is between the conduction and valence bands, with the energy difference being known as the band gap. The PL spectrum intensity is an indicator of the number of electron–hole recombination centres present in the material.

3.2.3.6 Raman spectroscopy

When monochromatic radiation is incident upon a sample, it interacts with the latter, in a process known as light-matter interaction. There are various scattering processes that occur when photons strike matter, and by analysing the scattered radiation, we can obtain useful information pertaining to the samples' molecular structure. For Raman scattering, the relevant scattering processes are Rayleigh scattering, Stokes and Anti-Stokes Raman scattering

In Rayleigh scattering, the wavelength of the incident and scattered radiation is the same, whereas in Stokes (and Anti-Stokes) Raman scattering, the wavelength of the scattered radiation is shorter (longer) than the incident radiation. From this wavelength change of the scattered photon, we can obtain chemical and structural information of the sample under study. In molecular systems, the characteristic wavelength shift values are principally associated with rotational, vibrational and electronic level transitions in the sample. Raman shifted photons of light can be either of higher or lower energy, depending upon the vibrational state of the molecule. In retrospect, Raman spectroscopy probes the chemical structure of a material and provides information about chemical structure and identity [176].

3.2.3.7 FTIR spectroscopy

FTIR is an analytical testing technique used to identify organic and some inorganic materials through the application of infrared radiation (IR). When IR is passed through a sample, some radiation is absorbed by the sample and some passes through (gets transmitted). FTIR uses interferometry to record direct information about a material placed in the IR beam. The Fourier Transform results in a wavenumber spectrum that analysts can be used to identify the sample, representing a molecular 'fingerprint' of the sample. The usefulness of infrared spectroscopy arises because different chemical structures (molecules) produce different spectral fingerprints. Once the spectrum is produced, computer searches of reference libraries assist in the material's identification. There are four major sampling techniques in FTIR: transmission, attenuated total reflection (ATR), specular reflection, and diffuse reflectance.

Thick samples often produce intense peaks when measured in the transmission mode. Hence, ATR works better for thick samples because the intensity of the evanescent waves decays exponentially with distance from the surface of the ATR crystal, making the technique generally insensitive to sample thickness.

We used the ATR technique owing to its several advantages: minimal sample preparation (just place the sample on the crystal and acquire the data), easy clean-up (simply remove the sample and wipe the crystal surface), ability to analyse samples in their natural states (no heating or pelletizing is necessary), and it is excellent for thick (e.g. powders) or strongly absorbing samples.

A common FTIR spectrometer consists of a source, interferometer, sample compartment, detector, amplifier, A/D convertor, and a computer. The source generates radiation which passes the sample through the interferometer and reaches the detector. Then the signal is amplified and converted to digital signal by the amplifier and analog-to-digital converter, respectively. Eventually, the signal is transferred to a computer in which Fourier transform is carried out.

The Michelson interferometer, the heart of modern FTIR spectrometers, splits a light beam into 2 so that their optical paths are different. Then the interferometer recombines the 2 beams and channels them to the detector, where the intensity difference of the 2 beams is recorded against the path difference of the 2 paths. Fig. 3.5 [177] is a schematic of the Michelson Interferometer.

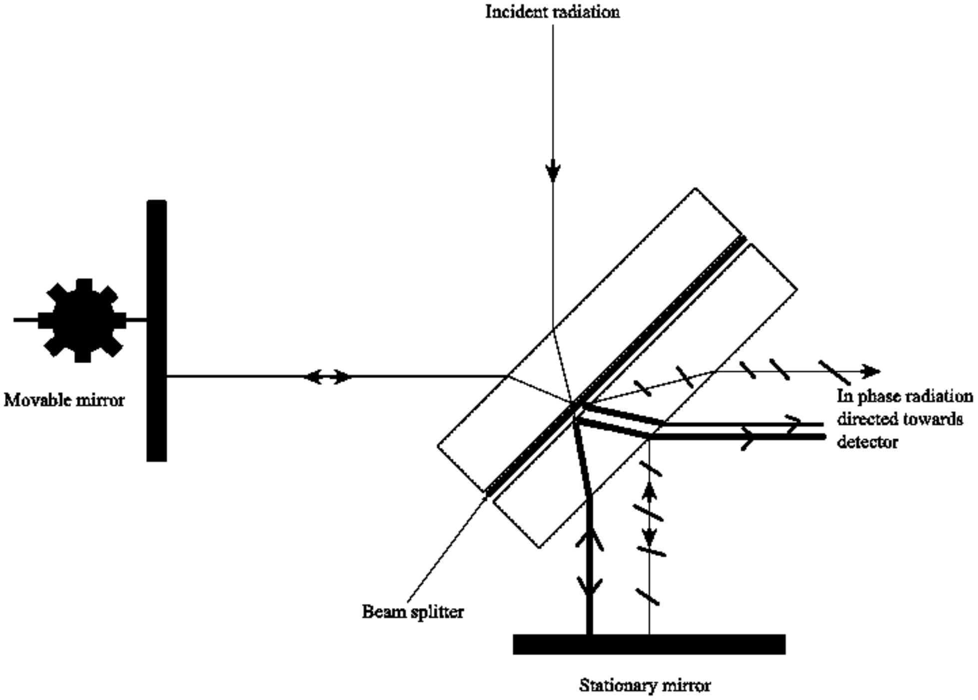

Fig. 3.5 Michelson interferometer set-up illustration [177]

Usually, a Michelson interferometer comprises 2 mutually-perpendicular mirrors, along with a beamsplitter. One mirror is stationary and the other is movable. The beamsplitter transmits 50% of the incident light and reflects the remaining 50%. The transmitted portion is incident on the stationary mirror, whilst the reflected one strikes the movable mirror. After being reflected back, the 2 beams recombine at the beamsplitter.

If both beams travelled exactly the same optical path length, the situation is called a zero path difference (ZPD). But if the moving mirror moves away from the beamsplitter, the corresponding light beam travels longer than the other beam, and this extra path length is known as the optical path difference (OPD). If the OPD is an integer multiple of wavelengths OPD $= n\lambda$, constructive interference occurs based on the principle of wave superposition. Conversely, if the OPD fulfils this criteria:

$$OPD = \left(n + \frac{1}{2}\right)\lambda$$

destructive interference occurs because crests overlap with troughs. If the OPD is neither $n\lambda$ nor $(n + 1/2)\lambda$, there is incomplete cancellation and the intensity obtained is somewhere between maximum and minimum. Therefore, as the mirror moves back and forth, the signal intensity increases and decreases, yielding a sinusoidal wave, known as an interferogram. The interferogram is a function of OPD, which is in the spatial (r) domain. This spatial domain (r) is Fourier transformed into the wavenumber (k) domain, which is the final FTIR spectrum of intensity against wavenumber [178].

3.3 Experimental set-up and details

3.3.1 Graphitic carbon nitride

3.3.1.1 Photoreactor set-up and details

The photocatalytic reduction of CO_2 to methanol was carried out in a vacuum tight cylindrical aluminium vessel, fitted with a quartz window (UV-permeable) on the top circular surface. This allows radiation to pass through it into the reaction chamber. The reaction chamber has a CO_2 gas inlet port with a pressure gauge to monitor the chamber gauge pressure. The sample for analysis is dispensed through a quarter inch outlet fitted with an airtight septum; 100 ml of deionized water is mixed with 100 mg of photocatalyst in the chamber, and the mixture is purged with continuously flowing CO_2 gas for 30 min prior to experiment, during which the solution is continuously stirred with a magnetic stirrer.

$$\mathbf{CO_2 + 6H^+ + 6e^- \rightarrow CH_3OH + H_2O \qquad -0.38\,V}$$
$$\mathbf{O_2 + 4H^+ + 4e^- \rightarrow 2H_2O \qquad +1.23\,V}$$

From the above redox equations, the reduction potential of O_2 is more positive than that of CO_2, which indicates that O_2 is a better electron scavenger than CO_2 and hence more easily reduced. This stronger electron scavenging by O_2 reduces the amount of electrons available for CO_2, leading to a decrease in the CO_2 photocatalytic reduction rate. The dissolved oxygen should be completely depleted, as far as possible, from the reaction medium by thorough purging to enable the efficient reduction of CO_2 to methanol. Hence, the reactor was purged for 30 mins prior to irradiation.

Before initiating the reaction with irradiation exposure, the CO_2 outlet valve was closed and the CO_2 gas pressure was maintained at 50 psi. While the reaction is in progress, 3.0 μL of the liquid sample was collected through the outlet septum using a micro syringe and filter system at regular intervals for gas chromatography mass spectrometry (GC/MS) analysis of the methanol concentration.

Since the amount of sample extracted is a very small proportion of the total liquid reaction medium, (0.003/100 = 0.003%), sample extraction did not cause the reactor pressure to fall, which was experimentally verified by the pressure gauge reading remaining virtually unchanged after extraction.

The analysis of the sample was carried out using an integrated gas chromatograph/mass spectrometry (Agilent 7890B), which is capable of analyzing the mass chromatograph and mass spectrum of the injected sample simultaneously. A brief schematic outline of the setup used for this study is presented in Fig. 3.6 below.

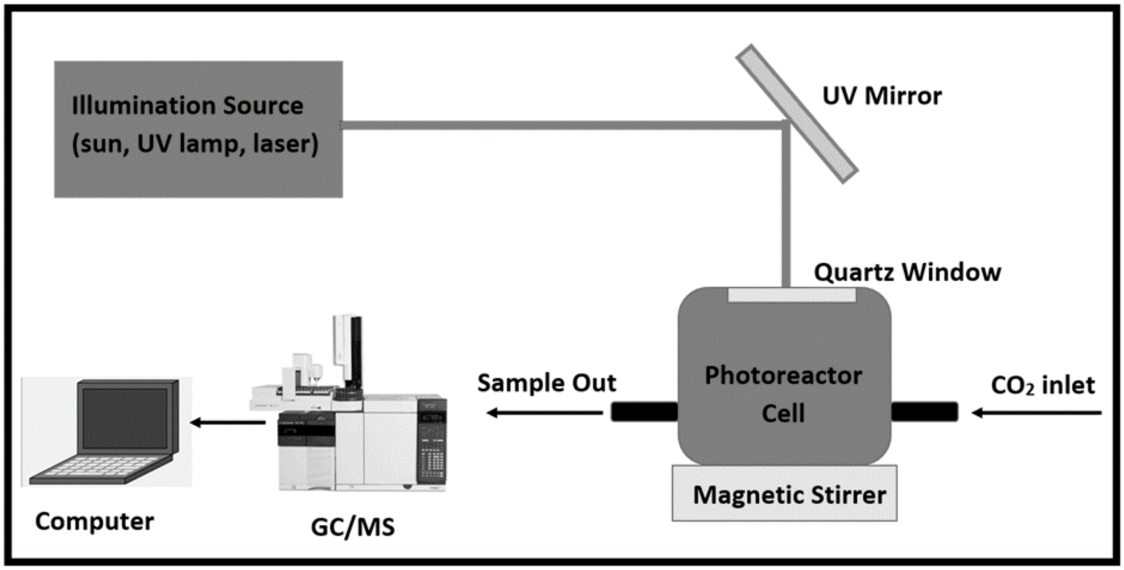

Fig. 3.6 Schematic diagram of the experimental setup for CO_2 reduction using g-C_3N_4.

3.3.1.2 GC calibration and retention time

In order to confirm the production of methanol/formic acid and also to quantify the respective amounts of each product, we first calibrated our GC/MS using standard aqueous methanol and formic acid solutions having known concentrations and plotted this against GC peak area. For the method used on our GC/MS, the retention time of 4.08 min and 8.69 min was observed for formic acid and methanol respectively. The calibration curves in Fig. 3.7 and 3.8 were obtained by using formic acid and methanol samples of known concentrations.

These samples were injected to the GC inlet, and the peak area for each product, at the relevant retention time, was observed. This calibration curve is then subsequently used to quantify the amount of methanol/formic acid produced in the photochemical reaction through CO_2 reduction. Prior to injecting each standard solution, several blank runs were performed to ensure that no residual methanol contaminant remained from previous experiments.

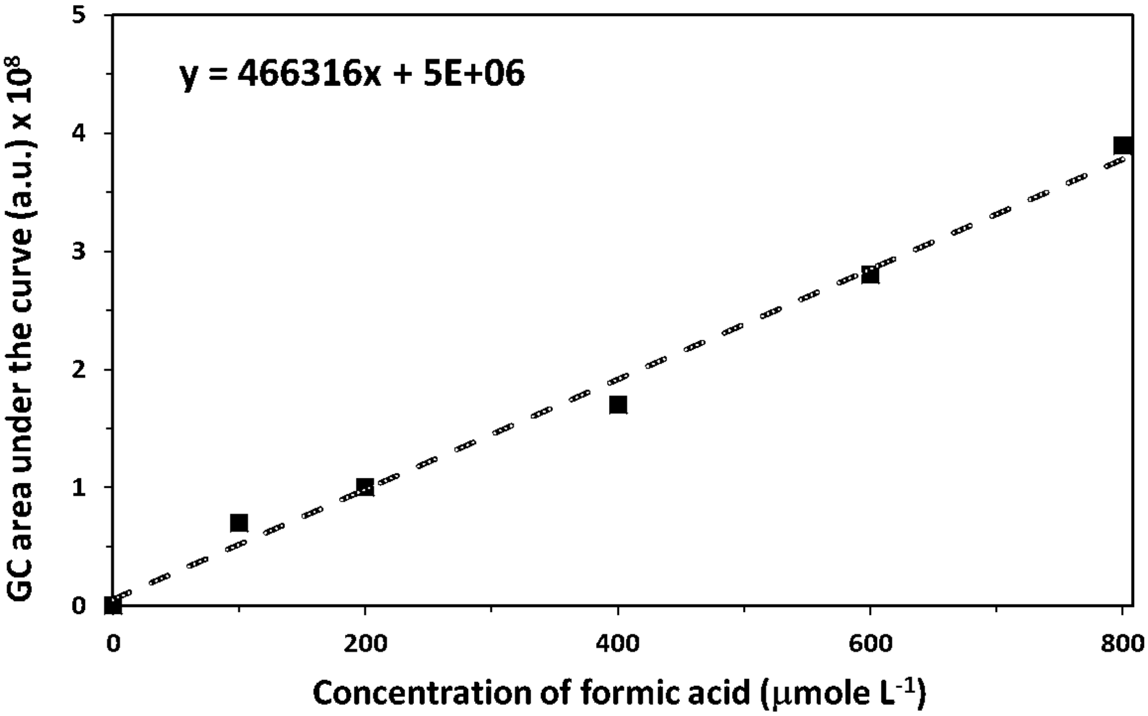

Fig. 3.7 Calibration curve showing gas chromatography peak area versus standard formic acid concentration

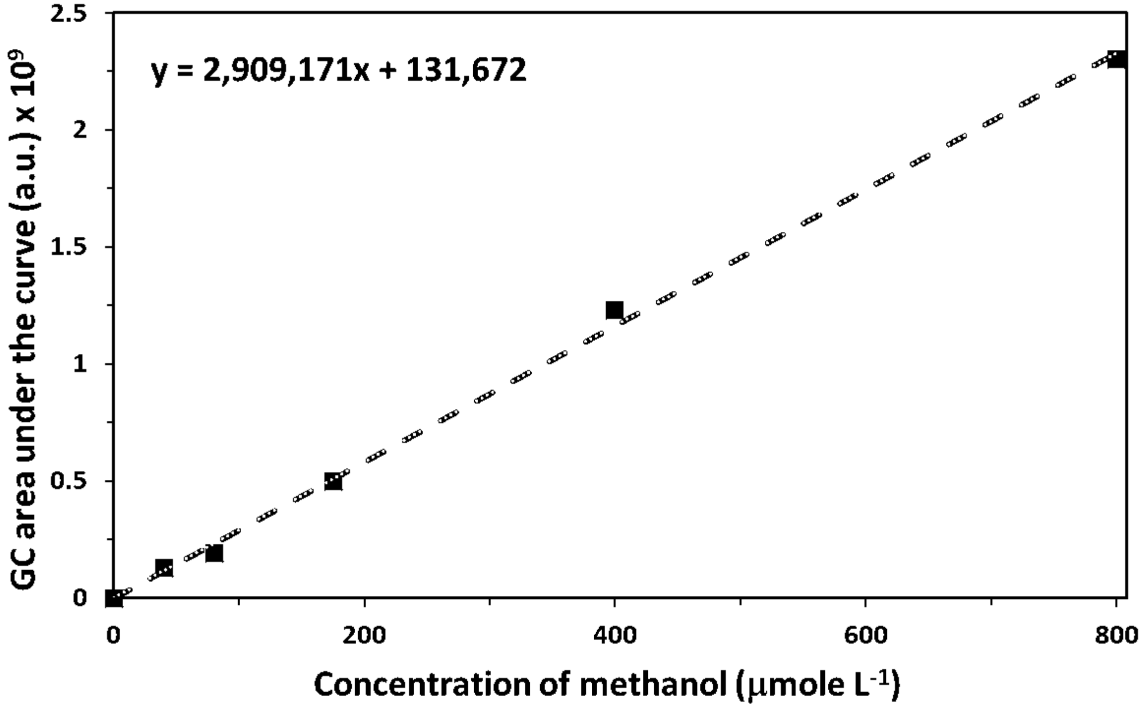

Fig. 3.8 Calibration curve showing gas chromatography peak area versus standard methanol concentration

3.3.1.3 Illumination sources used

The synthesized g-C_3N_4 was used for converting CO_2 into methanol using three different radiation sources: (i) 355-nm pulsed laser beam, which is the third harmonic of the Spectra Physics (Model GCR 250) Nd: YAG laser; (ii) Xe–Hg lamp; and (iii) natural solar radiation. The results obtained are presented in section 5.2. The various photoreactor configurations are shown in Fig. 3.9 (a) - (c) for pulsed laser, Fig. 3.9 (d) - (e) for the UV lamp and Fig. 3.9 (f) for natural solar radiation.

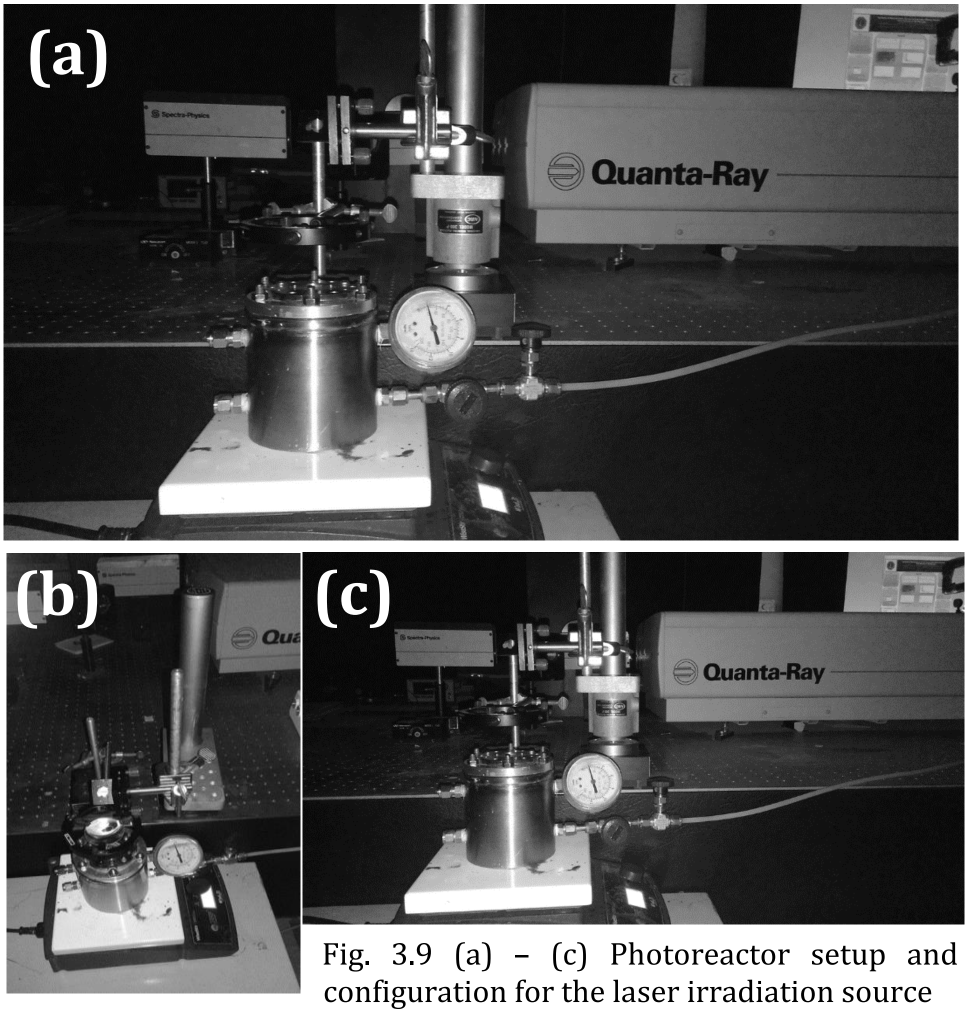

Fig. 3.9 (a) – (c) Photoreactor setup and configuration for the laser irradiation source

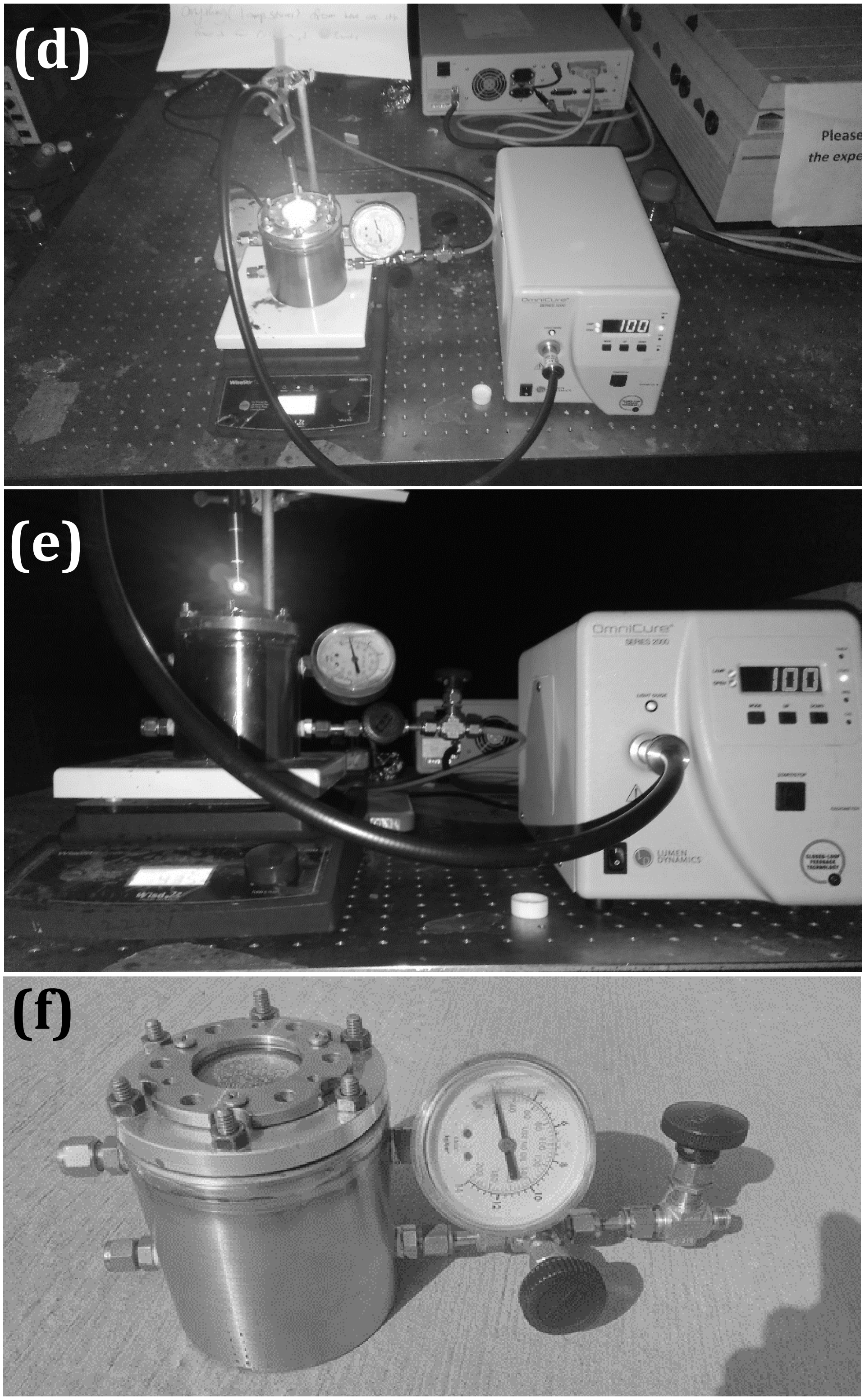

Fig. 3.9 (d) – (f) Photoreactor setup and configuration for the (d), (e) UV lamp and (f) natural solar radiation

3.3.2 Silver-loaded $NaNbO_3$

The experimental part involving photocatalytic testing of the pure and Ag-loaded $NaNbO_3$ photocatalyst is pretty much identical to that described above pertaining to graphitic carbon nitride, with two noteworthy exceptions.

Firstly, only the UV broadband lamp (Newport Xe–Hg lamp) was used for this part and it was kept at a fixed distance of approximately 2 cm from the reactor. Secondly, instead of using a pressurised reactor, we simply used a small 20 ml glass scintillation bottle as the reactor. This was inspired from reading published papers where some groups even used simple test tubes as the reactor. Since the focus of this thesis is on photocatalyst synthesis and parameter studies, we have learnt through experience that there is not much need to invest excessive amounts of time and resources into developing advanced reactors. Any vessel that performs the basic function of allowing the four basic reactants (CO_2, H_2O, photons and photocatalyst) to come within reaction range of each other is suitable for photocatalyst testing. Of course, there is always room for developing novel photoreactor designs but that is not the focus and objective of this study. Hence, for the aforementioned reasons, we used a 20 ml glass scintillation vial and filled it with 15 ml of deionized water for all parts of the experimentation involving $NaNbO_3$; i.e., for section 5.3. The reactor set-up is shown in Fig. 3.10(a) and (b).

The exact experimental procedure is as follows. Typically 25 mg of photocatalyst was dispersed in 15 ml of deionized water and this was sonicated for 15 to 20 minutes until we could visually confirm that the catalyst had formed a uniform homogeneous dispersion throughout the entire reactor volume. This is an extremely important criteria to prevent catalyst segregation and settling. After ensuring proper catalyst dispersion, CO_2 gas was bubbled into the reactor medium continuously for approximately 20 minutes to ensure proper saturation of CO_2 in the water. Whilst bubbling the CO_2, the reactor was immersed in freezing water to increase CO_2 solubility. In addition, during the bubbling phase, the reactor was left uncapped to allow CO_2 to flow through and out of the reactor volume. After 20 minutes of bubbling, the glass vial was immediately capped shut tightly (to create an airtight solution) with a septum cap. This cap allows sample extraction at periodic time intervals without having to open the reactor and disturb the reaction progress. The lamp position was set at a fixed orientation (i.e. both distance and angle were held fixed) with respect to the glass vial and this was consistently maintained for all parts of this experiment. A note was placed on the lamp head to instruct other personnel not to make any changes to the position of the lamp, to ensure consistency of all experiments performed in this section. In this manner, we tested 2 photocatalysts: pure $NaNbO_3$ and Ag-loaded $NaNbO_3$, over a time interval of roughly 10 hours, with hourly sample measurements taken via the septum. The products were analysed using the GC/MS system that has been detailed previously.

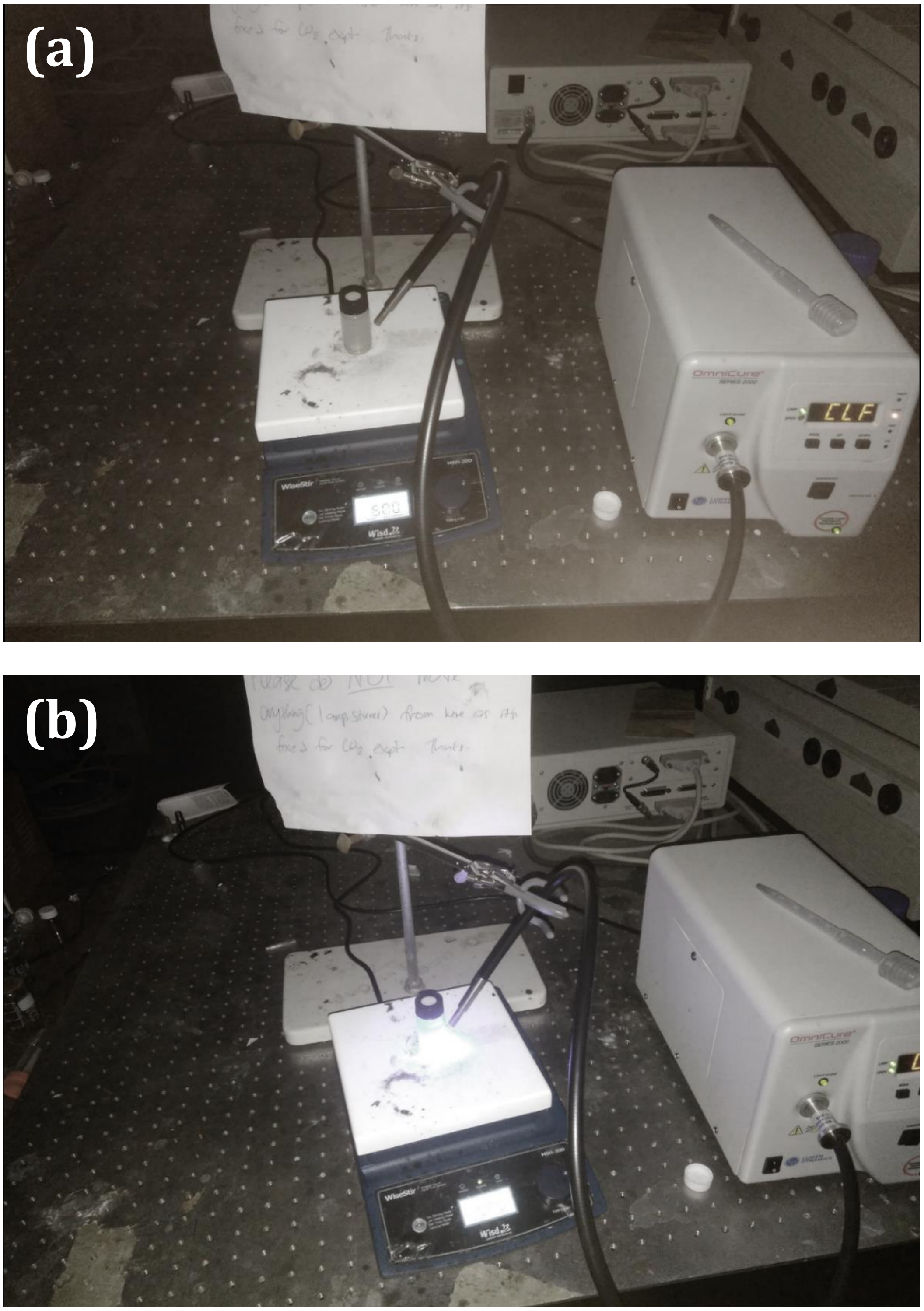

Fig. 3.10 Photoreactor setup and configuration using a 20 ml vial when the UV lamp is (a) switched off & (b) on

CHAPTER 4

MATERIALS CHARACTERIZATION OF PHOTOCATALYSTS

4.1 An overview

In this chapter, we present the materials characterization results pertaining to the following photocatalysts:

(c) graphitic carbon nitride (g-C_3N_4) as the solar-harvesting photocatalyst (section 4.2), and

(d) Ag-loaded $NaNbO_3$ as the methanol-selective (section 4.3) photocatalyst. The characterization results for each catalyst are classified in Table 4.1:

Material properties	Characterization techniques
Crystallographic	X-ray diffraction (XRD)
Morphological	Scanning electron microscope (SEM) Transmission electron microscope (TEM)
Electronic	X-ray Photoelectron Spectroscopy (XPS)
Optical	Ultraviolet-visible spectroscopy (UV-Vis) Fourier transform infrared spectroscopy (FT-IR) Photoluminescence spectroscopy (PL) Raman spectroscopy

Table 4.1 Classification of materials characterization techniques based on the material properties it studies

4.2 Solar-harvesting graphitic carbon nitride

4.2.1 Crystallographic and Structural Properties

Fig. 4.1 shows the X-ray diffraction (XRD) pattern of g-C_3N_4, where we observe a mostly flat profile, with the exception of two peaks: a weak peak at 13.0° due to the in-plane ordering of tri-s-triazine units and a stronger peak around 27.4° due to the graphite-like interlayer-stacked structure [179]

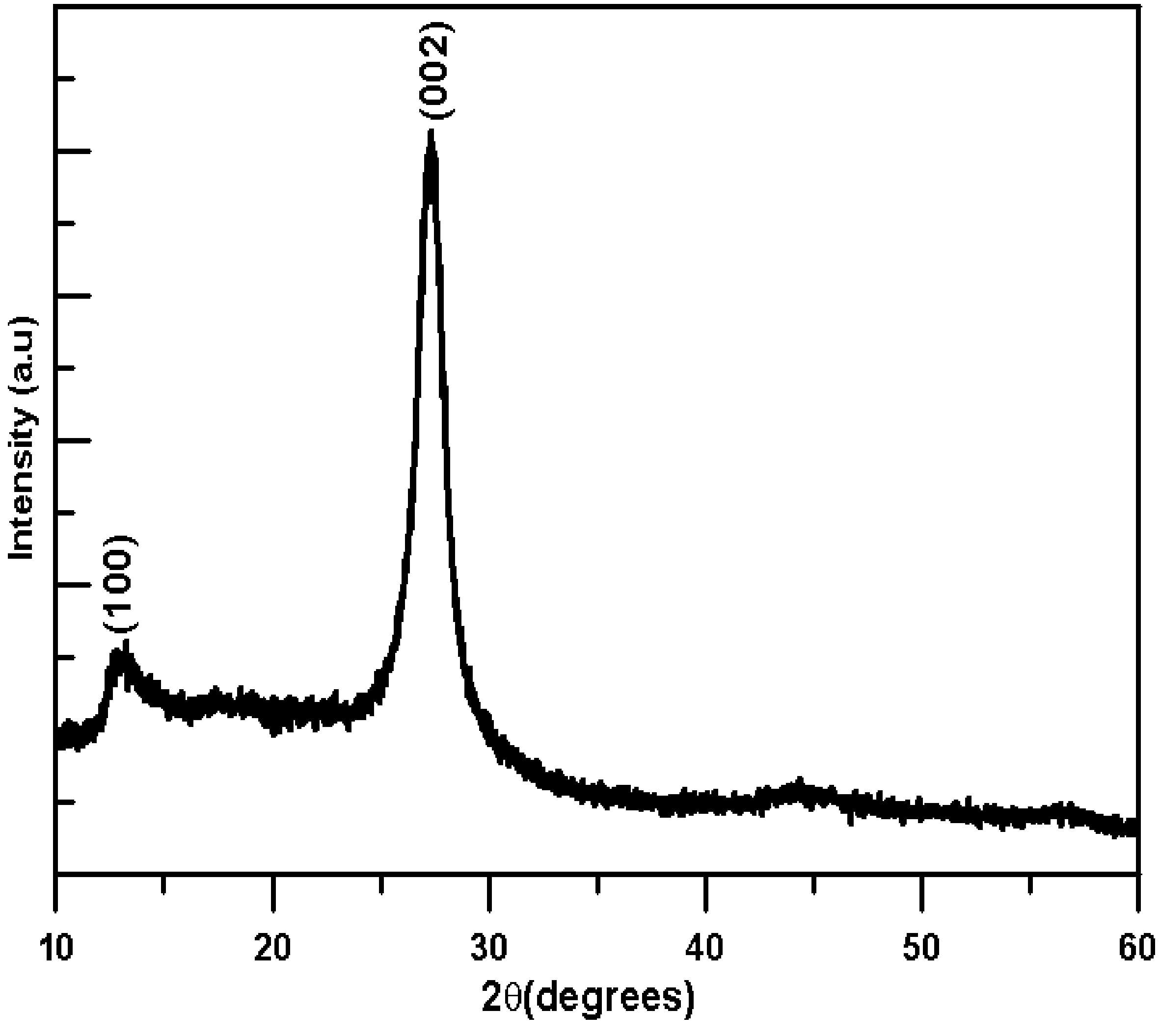

Fig. 4.1 X-ray diffraction pattern of g-C_3N_4

The physical origin of these peaks is accounted for by the structure of graphitic carbon nitride. As the term graphitic implies, g-C_3N_4 is comprised of stacked layers of atomic planes arranged in a parallel manner, wherein each layer is composed of repeating tri-s-triazine units (Fig. 4.2).

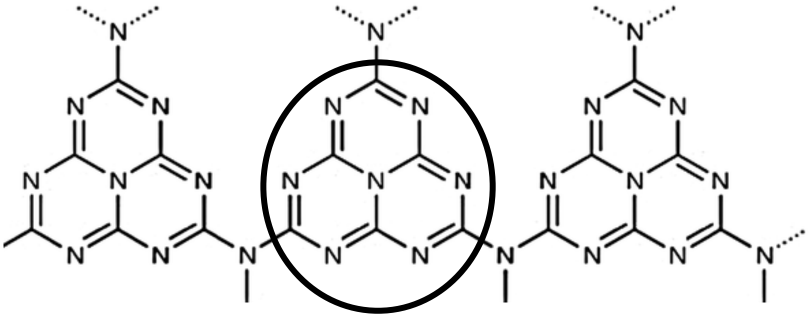

Fig. 4.2 X-ray diffraction pattern of g-C_3N_4 with a tri-s-triazine unit circled in black.

When the stacked layers act as diffraction planes, out-of-plane diffraction occurs (Fig. 4.3(a)). In-plane diffraction occurs when repeating tri-s-triazine units within each plane act as diffraction planes (Fig. 4.3(b)).

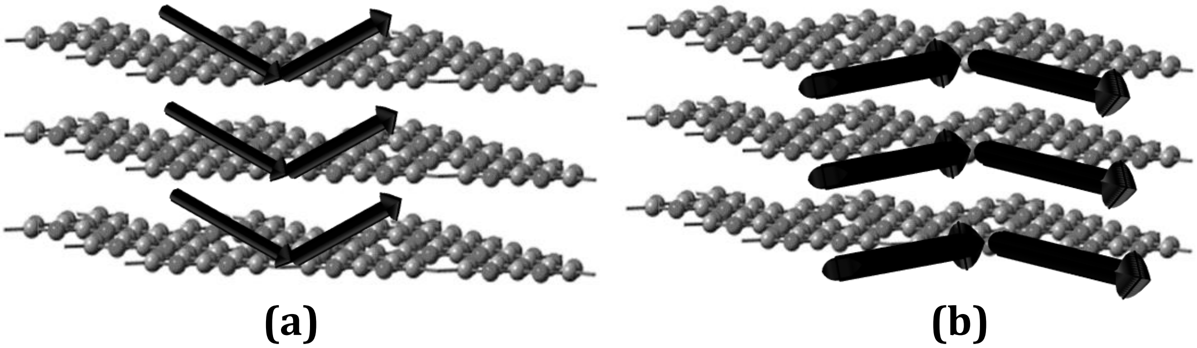

Fig. 4. 3 (a) Out-of-plane and (b) in-plane diffraction in g-C_3N_4

The information obtained from these XRD peaks is summarised in Table 4.2 below. Interestingly, the (002) graphite plane also exhibits a sharp diffraction peak at 2θ = 26.5° [180], which is relatively close to our g-C_3N_4 peak at 2θ = 27.4°. This confirms that g-C_3N_4 indeed has a graphitic-stacked structure. The other diffraction peak at 2θ = 13.0° has been obtained by several groups [181-186], and has been consistently attributed to the in-plane diffraction caused by repeating tri-s-triazine units. The foregoing points indicate that these two peaks are a unique fingerprint of g-C_3N_4 and can be used to positively confirm its successful formation.

XRD peak	Cause of peak	What we learn?
(100) at 13.0°	in-plane ordering of tri-s-triazine units (in-plane diffraction)	Indicates presence of tri-s-triazine (heptazine) units within each layer
(002) at 27.6°	interlayer-stacking peak (out-of-plane diffraction)	Confirms presence of graphite-like layered structures in g-C_3N_4

Table 4.2 Information obtained from XRD spectra of g-C_3N_4

To further clarify the chemical composition and bonding information of g-C_3N_4, we acquired its Fourier transform infrared (FTIR) spectra (Fig. 4.4).

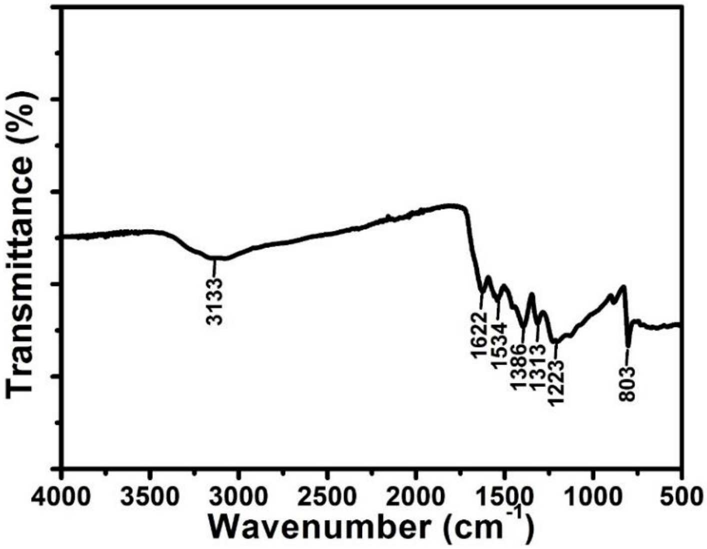

Fig. 4.4 FTIR spectra of g-C_3N_4.

The FTIR spectra exhibits 3 main groups of peaks: 2 solitary peaks at 803 and 3133 cm^{-1} and a cluster of peaks in the range of 1200 – 1600 cm^{-1}, as summarised in Table 4.3 below.

Wavenumber (cm^{-1})	Cause of peak	What we learn?
803	breathing modes of tri-s-triazine (i.e. heptazine) units	Confirms XRD (100) peak i.e. existence of tri-s-triazine
1200–1600	stretching vibrations of aromatic CN heterocycles	Confirms CN cyclic structure, a characteristic of g-C_3N_4
3000–3500	N–H stretching vibration modes	Existence of unreacted melamine precursors

Table 4.3 Information obtained from FTIR spectra of g-C_3N_4

The absorption peaks in the 1200–1600 cm^{-1} interval are assigned to various stretching modes of g-C_3N_4 heterocycles [187-190], whilst that at 803 cm^{-1} is attributed to the bending mode of tri-s-triazine rings [191-195]. Bending and stretching modes involve changes in the bond angle and bond length respectively. To rule out the possibility of this ring structure being graphene instead of tri-s-triazine, we note that the FTIR spectra of both graphite and graphene [196] possess no peak in the vicinity of 800 cm^{-1}, as per Fig. 4.5.

The solitary peak at 3133 cm^{-1} is assigned to residual N–H groups, which arises due to incomplete condensation of the melamine precursor [197-200]. This point will be elaborated upon at length under the analysis of XPS results.

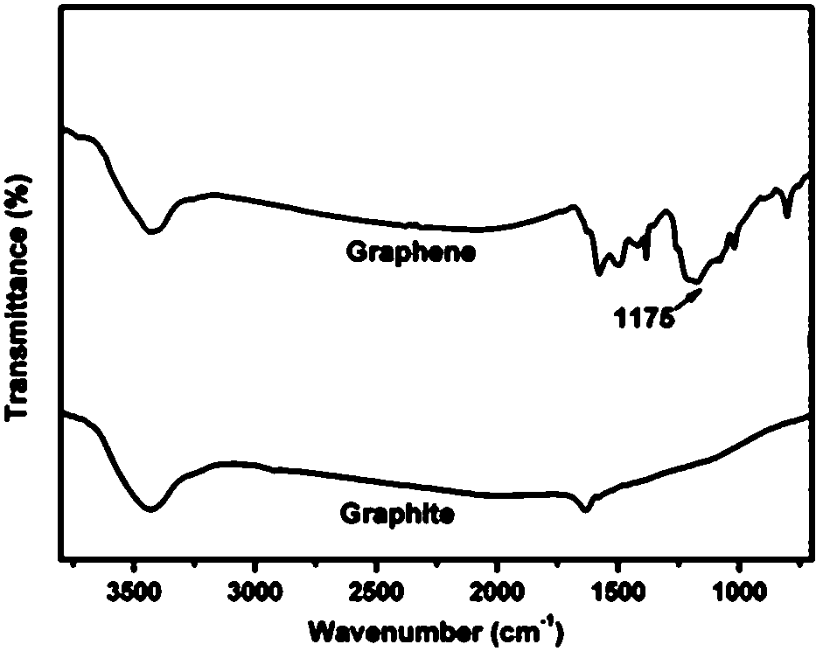

Fig. 4.5 FTIR spectra of graphite and graphene

4.2.2 Morphological Properties

The magnified transmission electron microscopy (TEM) image of as-synthesized g-C_3N_4 is displayed in Fig. 4.6(a). The energy-dispersive X-ray spectroscopy (EDS) elemental mapping images in Fig. 4.6(b) and (c) identify the distribution of carbon and nitrogen respectively as uniform and continuous. The SEM images in Fig 4.6 (d) – (g) show the particle morphology as generally rounded and somewhat elongated, with particles being approximately 0.8 to 1.2 μm in length.

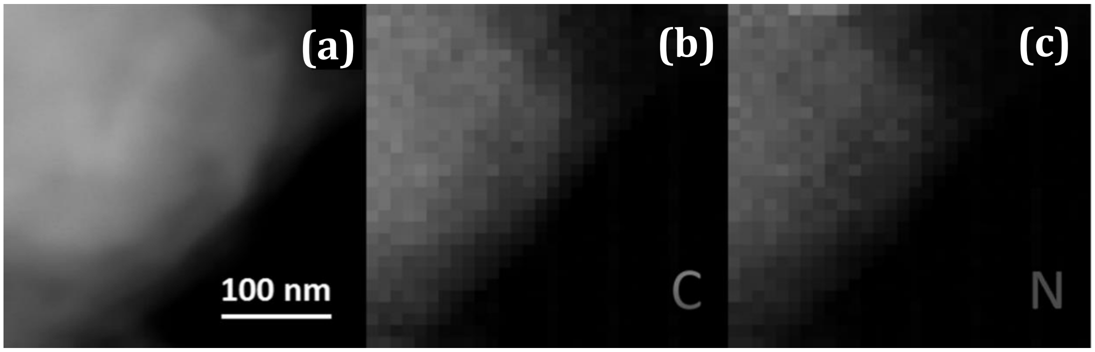

Fig. 4.6 TEM (a) and elemental mapping images – carbon (b) and nitrogen (c)

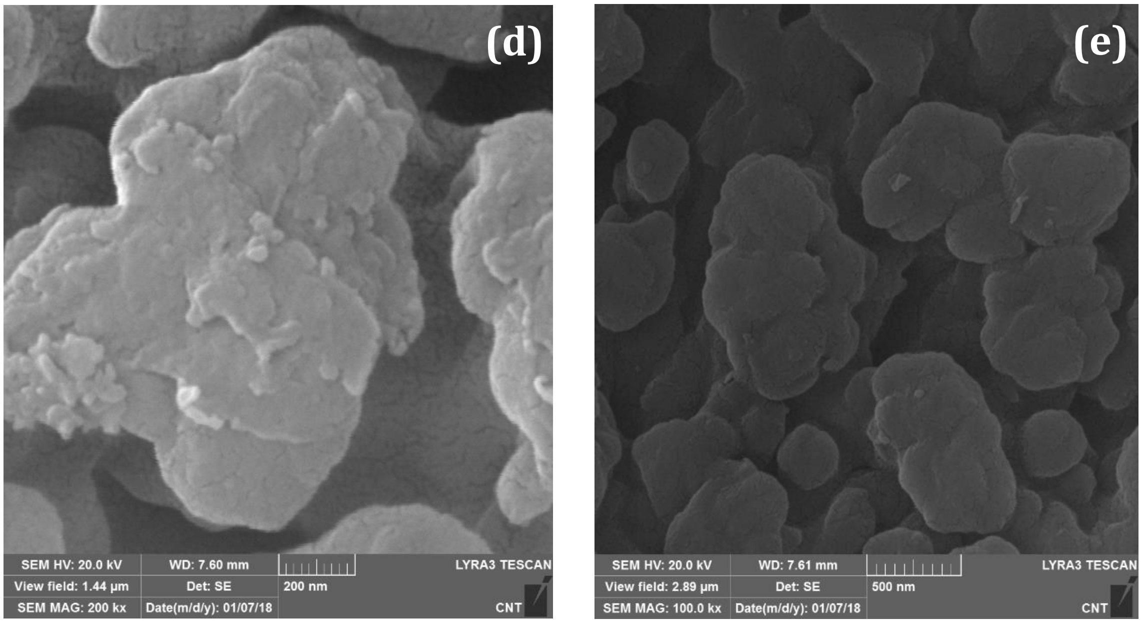

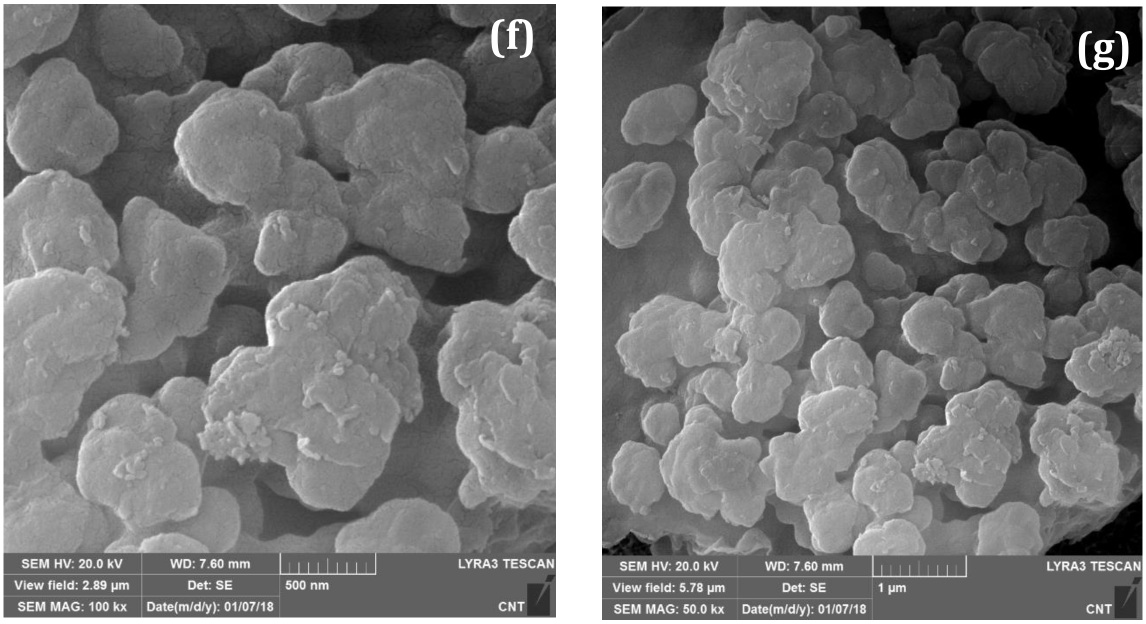

Fig. 4.6 (d) – (g) SEM images of as-synthesized g-C_3N_4 at various magnifications.

4.2.3 Electron Properties

X-ray photoelectron spectroscopy (XPS) characterization is shown in Fig. 4.7, where the survey scan in Fig. 4.7(a) indicates the presence of C, N and a small amount of O as evidenced by the weak O1s peak centered at 531.0 eV. This could be due to the presence of adsorbed oxygen molecules, adsorbed water, oxygen-containing terminal groups and/or oxides on the sample surface [201].

The deconvolution of the C 1s peak in Fig. 4.7(b) implies the existence of 2 carbon species, in which the peak centered at 283.4 eV is due to the sp^2 carbon atoms, which are bonded to nitrogen inside trigonal carbon configuration of the aromatic structures [202-205] and the peak centered at 286.1 eV is accounted for by carbon being in a tetrahedral configuration owing to sp^3-hybridization [206-208]. These 2 peaks are derived, respectively, from two-coordinated C2 and C1 atoms in tri-s-triazine rings. The deconvolution of N 1s shown in Fig. 4.3(c) exhibits two peaks, in which the one centered at 397.1 eV is due to tetrahedral dinitrogen (N_2) bonded to an sp^3-hybridized carbon in a heptazine unit (i.e. C–N–C groups) [209], and the other peak at 398.9 eV arises from tertiary nitrogen (i.e. $N–(C)_3$ groups) [210]. The integration of the carbon and nitrogen peak intensities yielded a C/N ratio of 0.69, which amounts to 8% excess of nitrogen, compared to the theoretical value of C/N = 0.75. This is due to the incomplete amine condensation when g-C_3N_4 is synthesized by heating melamine. The results are in good consonance with the FTIR spectra (Fig. 4.4), wherein the 3133 cm^{-1} peak was attributed to the amine N-H group. We now understand that this belongs to uncondensed amine groups. Thomas et al [211] observe that typical C/N values are 0.72, indicating great difficulty in fully eradicating the hydrogen content by simple heating beyond this limit. This indicates the existence of an energetic hindrance in the final elimination steps. Yan et al [212] agree that the C/N ratios of g-C_3N_4 obtained by heating melamine almost always falls short of the 0.75 expected for an ideal g-C_3N_4 sample. They also ascribe the excess nitrogen content to amine groups arising from incomplete condensation of melamine precursor. These residual amino groups indicate that it becomes increasingly difficult to completely eliminate the hydrogen content by simply heating melamine at ambient pressure, in agreement with the aforementioned conclusion arrived at by Thomas et al [211].

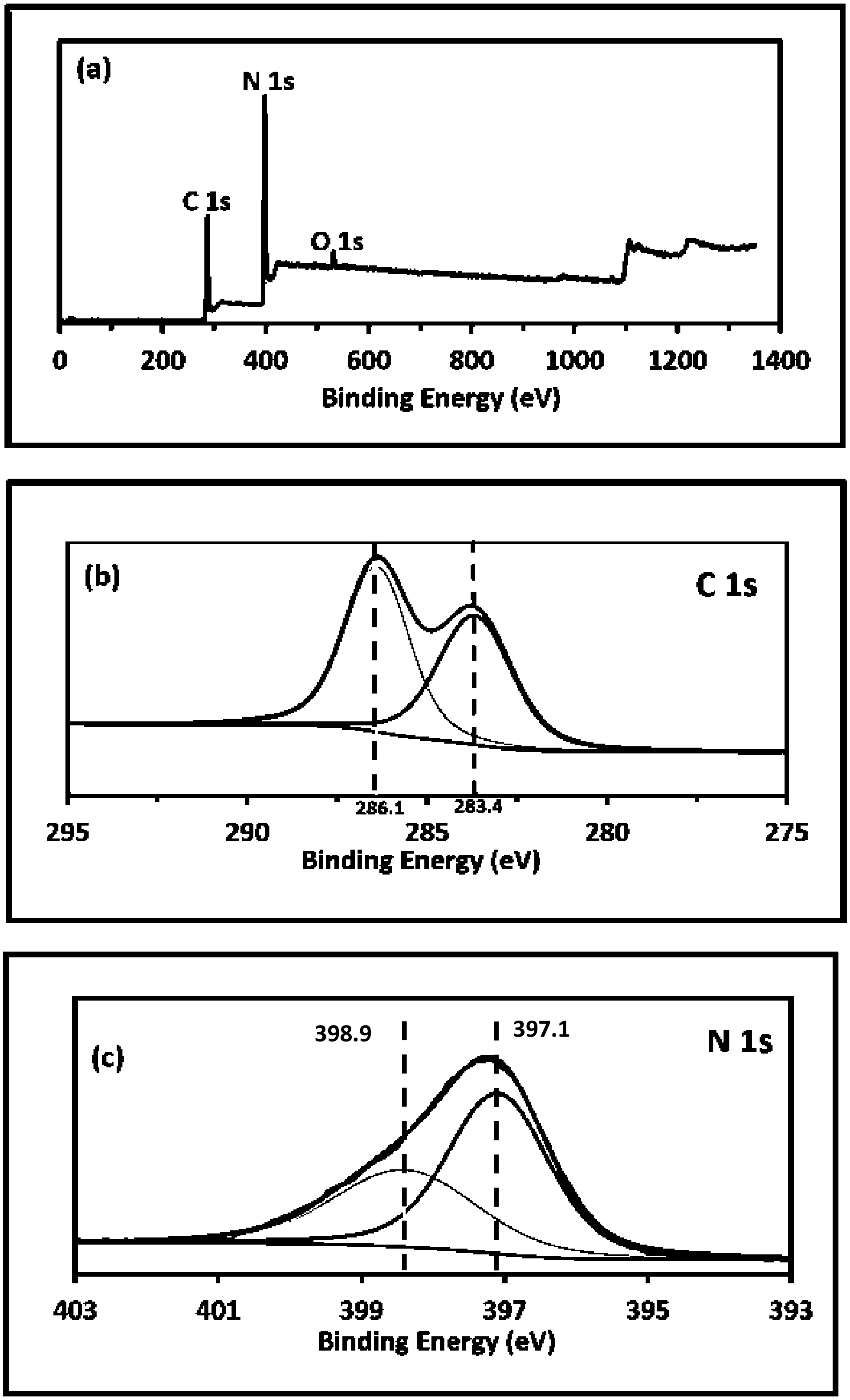

Fig. 4.7 XPS of g-C_3N_4 for the (a) survey scan, (b) C 1s and (c) N 1s orbitals

4.2.4 Optical Properties

Fig. 4.8 shows the absorption spectrum of g-C_3N_4 presented using the KM function, where it is seen that this material exhibits good light absorption in the UV-Visible region with the absorption peak centered at 396 nm. The absorption band in the visible region from 400 to 500 nm is in accordance with the literature [213-214], and is due to the electronic transition of π–π* or n–π* in the tri-s-triazine ring system [215]. The inset of Fig. 4.8 shows the Tauc plot for g-C_3N_4; the band gap energy is estimated to be 2.7 eV, which is in good agreement with the literature [216].

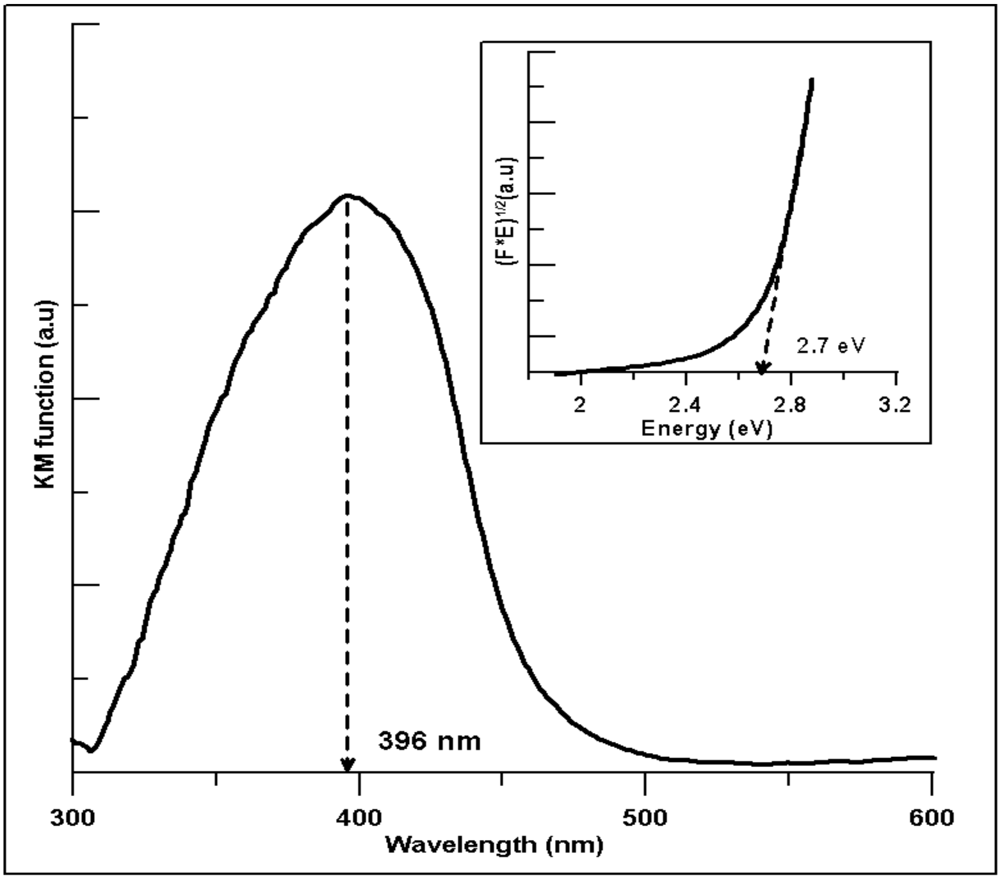

Fig. 4.8 Diffuse reflectance spectra represented as Kubelka–Munk function for g-C_3N_4. The inset contains the Tauc plot from which the band gap energy is enumerated.

4.3 Methanol selective Ag-loaded $NaNbO_3$

4.3.1 Structural Properties

The phase structures of both pure $NaNbO_3$ and Ag-loaded $NaNbO_3$ were studied by X-ray diffraction (XRD) analysis. As shown in Fig. 4.9, the as-prepared pure $NaNbO_3$ photocatalyst was well crystallized, as evidenced by most peaks being rather sharp and narrow. The excellent crystallinity is attributed to the high calcination temperature. All the peaks of pure $NaNbO_3$ are accounted for by the characteristic peaks of orthorhombic-phase $NaNbO_3$ (JCPDS card no. 01-072-7753 – Fig. 4.9). This indicates that no other crystalline phase was present, alluding to the high degree of phase purity of the as-synthesized $NaNbO_3$ samples. The aforementioned step confirms that the as-prepared photocatalyst is indeed pure $NaNbO_3$.

We next study the changes induced in the XRD spectra by loading silver onto $NaNbO_3$. Fig. 4.10 shows the XRD spectra of (a) pure $NaNbO_3$, (b) Ag-loaded $NaNbO_3$ and (c) their difference spectra. The difference spectra is simply an arithmetic subtraction of the pure spectra from the Ag-loaded one (i.e. XRD of Ag-loaded $NaNbO_3$ minus XRD of pure $NaNbO_3$), and it reveals two types of variations - oscillatory and non-oscillatory. Oscillatory variations are symptomatic of peaks shifting sideways, whilst non-oscillatory variations indicate the presence of new compounds/phases. These terms – oscillatory and non-oscillatory – are illustrated in Fig. 4.11. We first consider the oscillatory variations. When peaks shift sideways, there will inevitably be 2 angular ranges, in each of which one spectrum exceeds the other numerically.

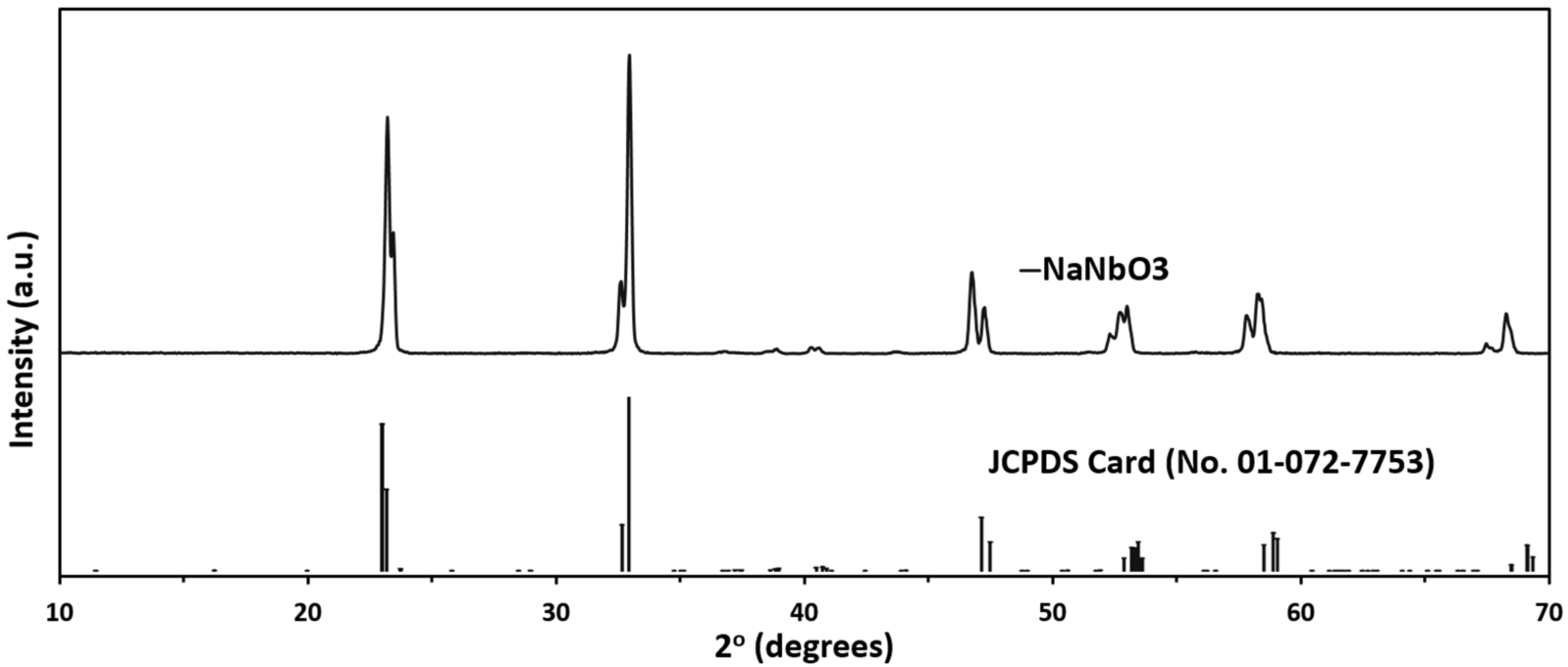

Fig. 4.9 X-ray diffraction results of pure $NaNbO_3$ and its matching JCPDS Card

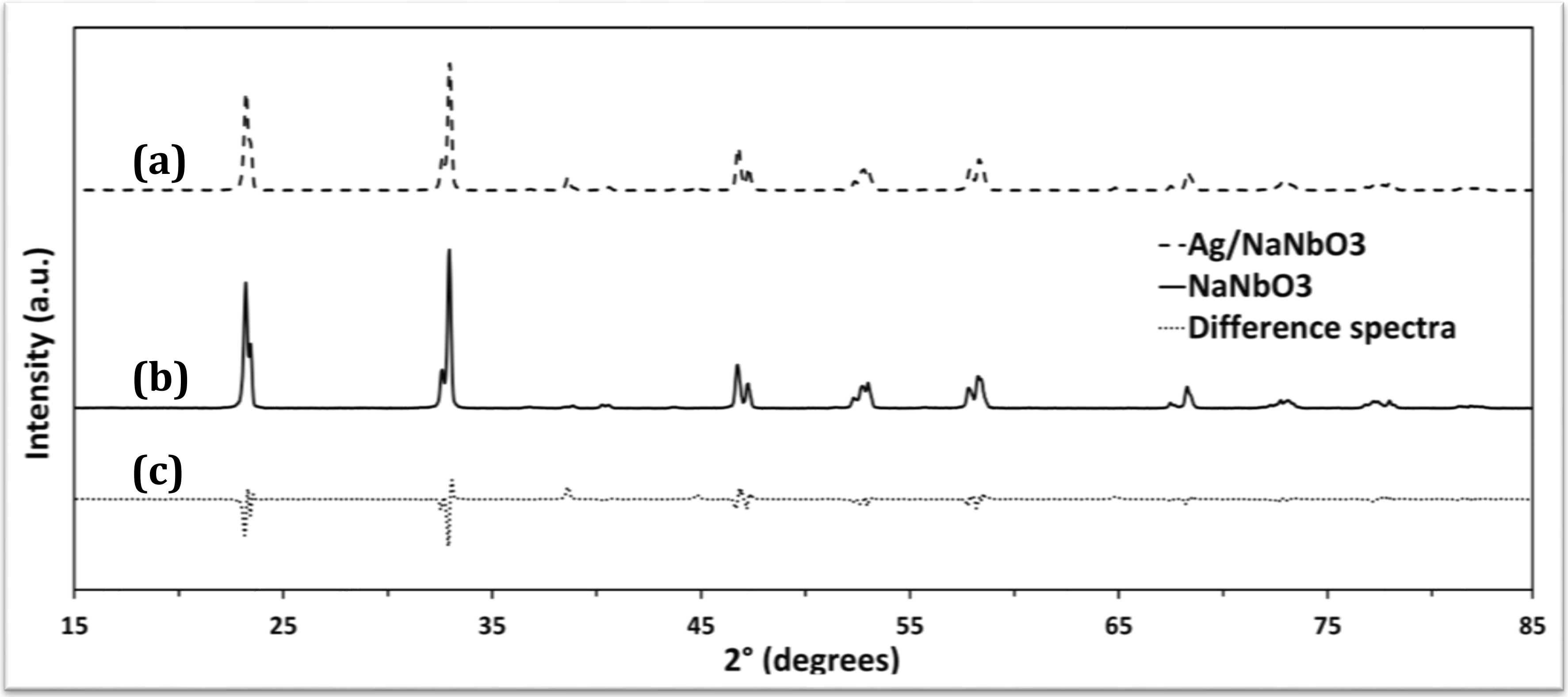

Fig. 4.10 XRD results of (a) Ag-loaded $NaNbO_3$, (b) pure $NaNbO_3$ and the (c) difference spectra

For instance, in Fig. 4.11(a), the two peaks intersect at 33°. Below 33°, the XRD spectrum of pure $NaNbO_3$ is numerically greater than $Ag/NaNbO_3$ and above 33°, the $Ag/NaNbO_3$ spectrum is higher than its pure counterpart. Hence, when the difference spectrum is computed, it will have a positive and negative segment, resulting in oscillatory behaviour about the horizontal axis, as per Fig. 4.11(a). In contrast, when a new peak appears in the Ag-loaded spectrum, which is absent in the corresponding pure $NaNbO_3$ spectra, the difference spectrum is simply a positive non-oscillatory spectrum as per Fig. 4.11(b).

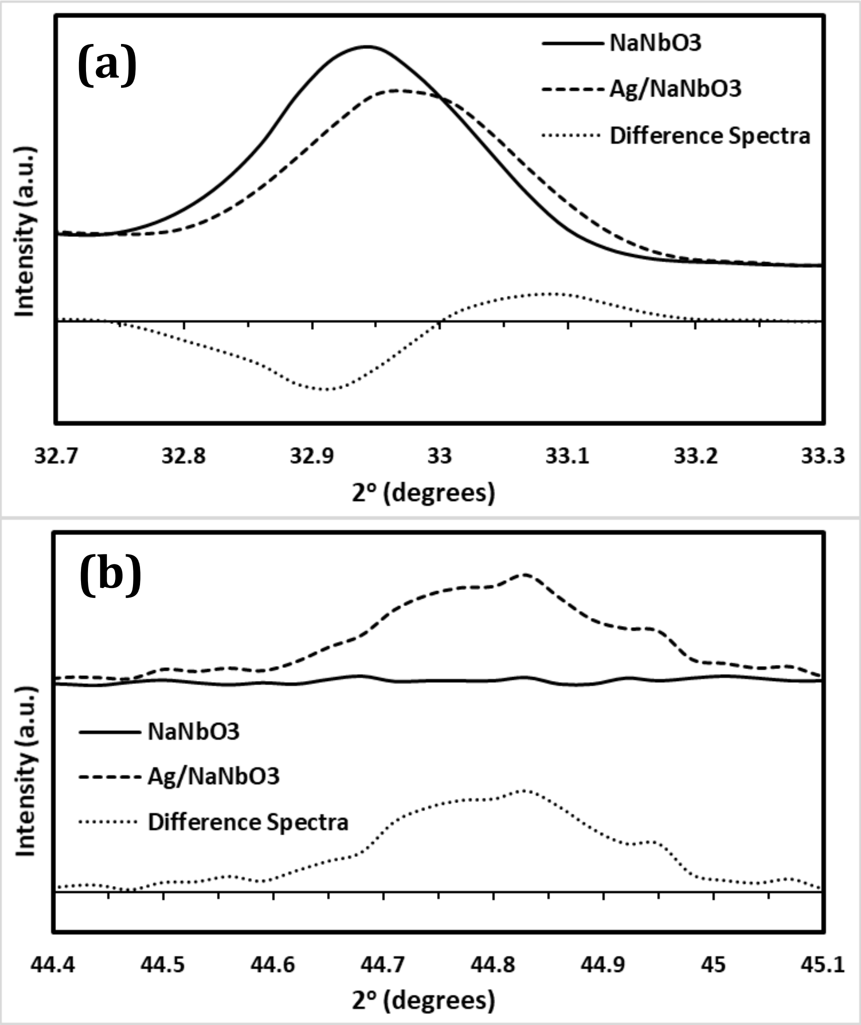

Fig. 4.11 An illustration of (a) oscillatory and (b) non-oscillatory variations

However, before any reliance can be placed on the peak shifts, it is necessary to ascertain that the shifting is exclusively caused by the silver loading and not by machine irreproducibility issues. This was investigated by repeating the XRD analysis of the pure $NaNbO_3$ sample thrice, which was recorded in Table 4.4. The angular values of the XRD peaks are highly reproducible with negligible variation over 3 repetitions. This offers convincing evidence that the peak shifts are indeed due to the silver loading and not due to irreproducibility issues. As a specific example of how Table 4.4 was obtained, the 3 runs of the 23.2° peak are shown in Fig. 4.12.

Run 1 (°)	**Run 2 (°)**	**Run 3 (°)**
23.20	23.20	23.20
32.96	32.96	32.96
47.26	47.26	47.26
52.72	52.74	52.72
58.38	58.36	58.36
68.28	68.28	68.28
72.76	72.76	72.78
77.96	77.96	77.98

Table 4.4 XRD results of pure and Ag-loaded $NaNbO_3$.

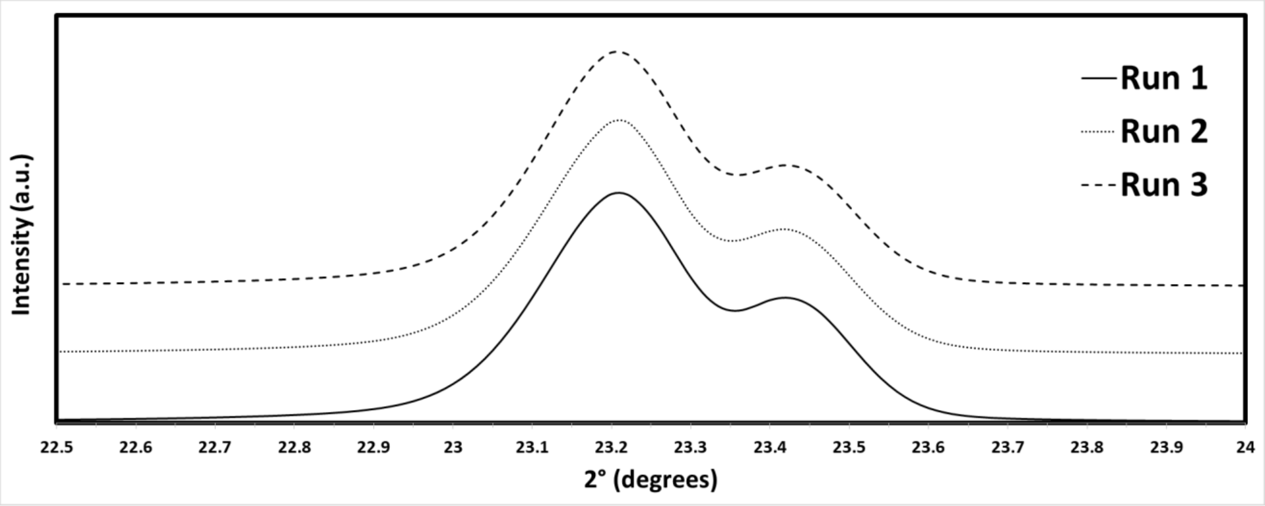

Fig. 4.12 X-ray diffraction results of pure and Ag-loaded $NaNbO_3$.

We now proceed with a detailed discussion regarding the oscillatory and non-oscillatory peaks. The former occurs at 23.20°, 32.96°, 47.26°, 52.9°, 58.3°, 68.3°, 72.8° and 78.0° (Fig. 4.13(a) – (h)) whilst the latter is seen at 38.6°, 44.8° and 64.8° (Fig. 4.14(a) – (c)).

Regarding the peak shifts, Qianqian Liu et al [221] have studied in detail the effect of doping pure $NaNbO_3$ nanowires and nanocubes with platinum nanoparticles (Pt NPs), resulting in the synthesis of Pt/$NaNbO_3$ nanowires and nanocubes respectively. From the XRD spectra, slight characteristic diffraction peak shifts were observed in Pt/$NaNbO_3$ nanowires, but not in the corresponding nanocubes. From this, they concluded that Pt NPs incorporate well into the $NaNbO_3$ nanowire lattice, but not into the $NaNbO_3$ nanocube lattice. Hence, XRD peak shifts are a suitable indicator of the degree of penetration of deposited metal particles into the crystal lattice of the primary photocatalyst.

From our difference spectra (Fig. 4.10(c)), we locate 8 diffraction angles (Fig. 4.13(a) – (h)) at which significant XRD peak shifting is observed, which demonstrates strong interaction between the Ag particles and the primary $NaNbO_3$ lattice. It is known that strong metal-catalyst interaction helps promote rapid electron transfer and further enhances the separation of electron-hole pairs, thus contributing to the enhancement of photocatalytic activity over Ag-loaded $NaNbO_3$ photocatalyst.

The non-oscillatory variations at 38.6°, 44.8° and 64.8° (Fig. 4.14(a) – (c)) indicate the presence of new crystal phases in Ag-loaded $NaNbO_3$, that are absent in pure $NaNbO_3$. Hence, these peaks belong to either pure Ag or its oxide Ag_2O. The peaks at 44.8° and 64.8° are known to belong to Ag [217] whilst the origin of the 38.6° peak is still ambiguous because there is both an Ag peak at 38.3° [217] and an Ag_2O peak at 38.5° [218]. If the peak belongs to elemental Ag, then its presence is self-explanatory. If it belongs to Ag_2O then its occurrence can be accounted for by studying the synthesis procedure. To produce elemental silver particles, silver nitrate is heated, whereby it decomposes as follows:

$$2\ AgNO_3(l) \rightarrow 2\ Ag(s) + O_2(g) + 2\ NO_2(g)$$

Qualitatively, decomposition is negligible below the $AgNO_3$ melting point (209.7 °C), but becomes appreciable around 250 °C and complete decomposition occurs at 440 °C [219]. This reaction must be performed under a fume hood because toxic nitrogen dioxide gas evolves during the reaction. However, the elemental silver formed can undergo oxidation at temperatures below 195° C, in the presence of atmospheric oxygen, as follows:

$$4Ag\ (s) + O_2\ (g) \rightarrow 2Ag_2O\ (s)$$

This explains the possible presence of Ag_2O peaks appearing in the XRD spectra of Ag-loaded $NaNbO_3$. Possibly, during the cool down procedure, the elemental silver reacted with atmospheric oxygen to form Ag_2O.

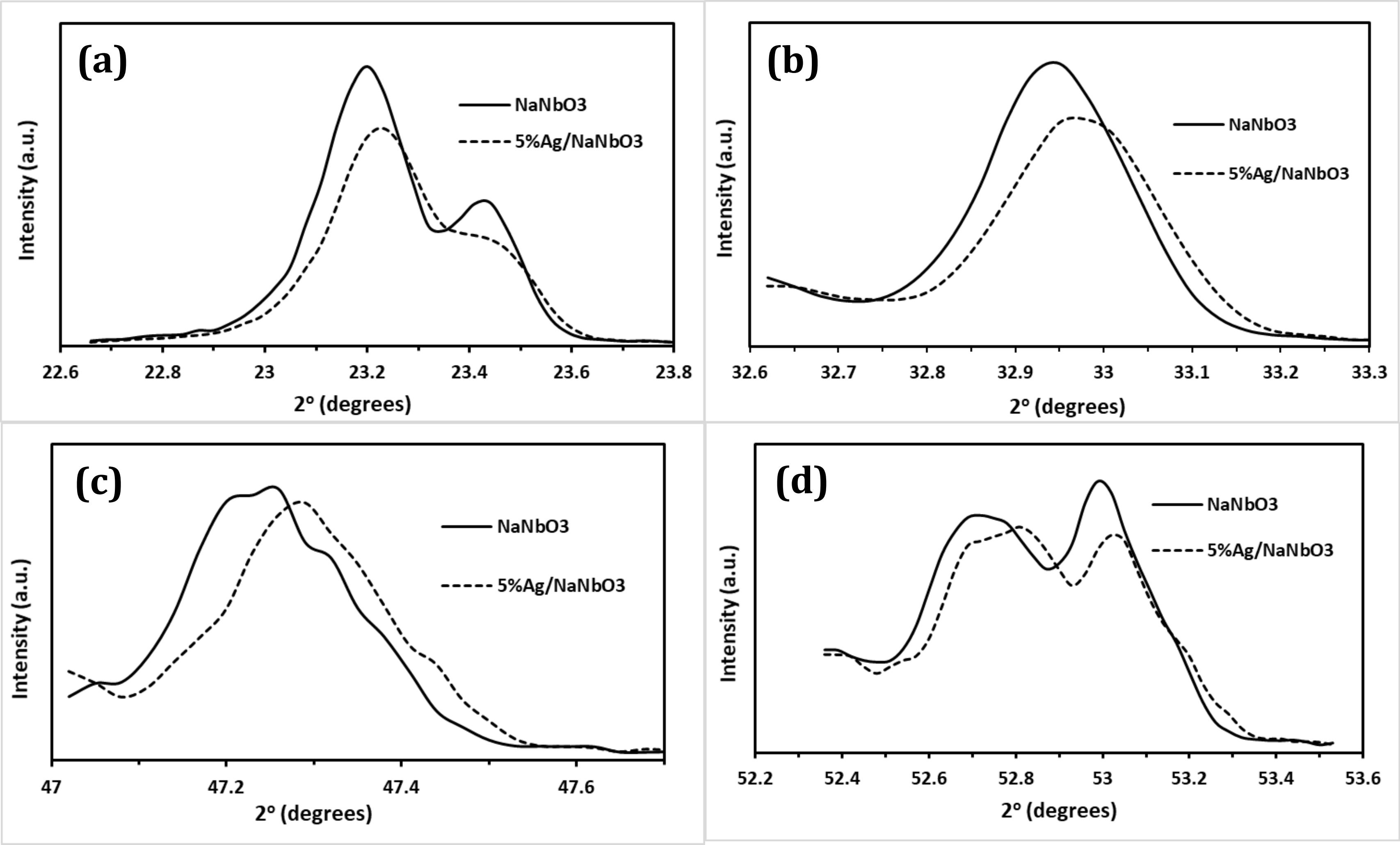

Fig. 4.13 (a) – (d) XRD spectra of pure and Ag-loaded NaNbO$_3$ showing lateral peak shifts at 23.2°, 32.95°, 47.3° and 52.9°

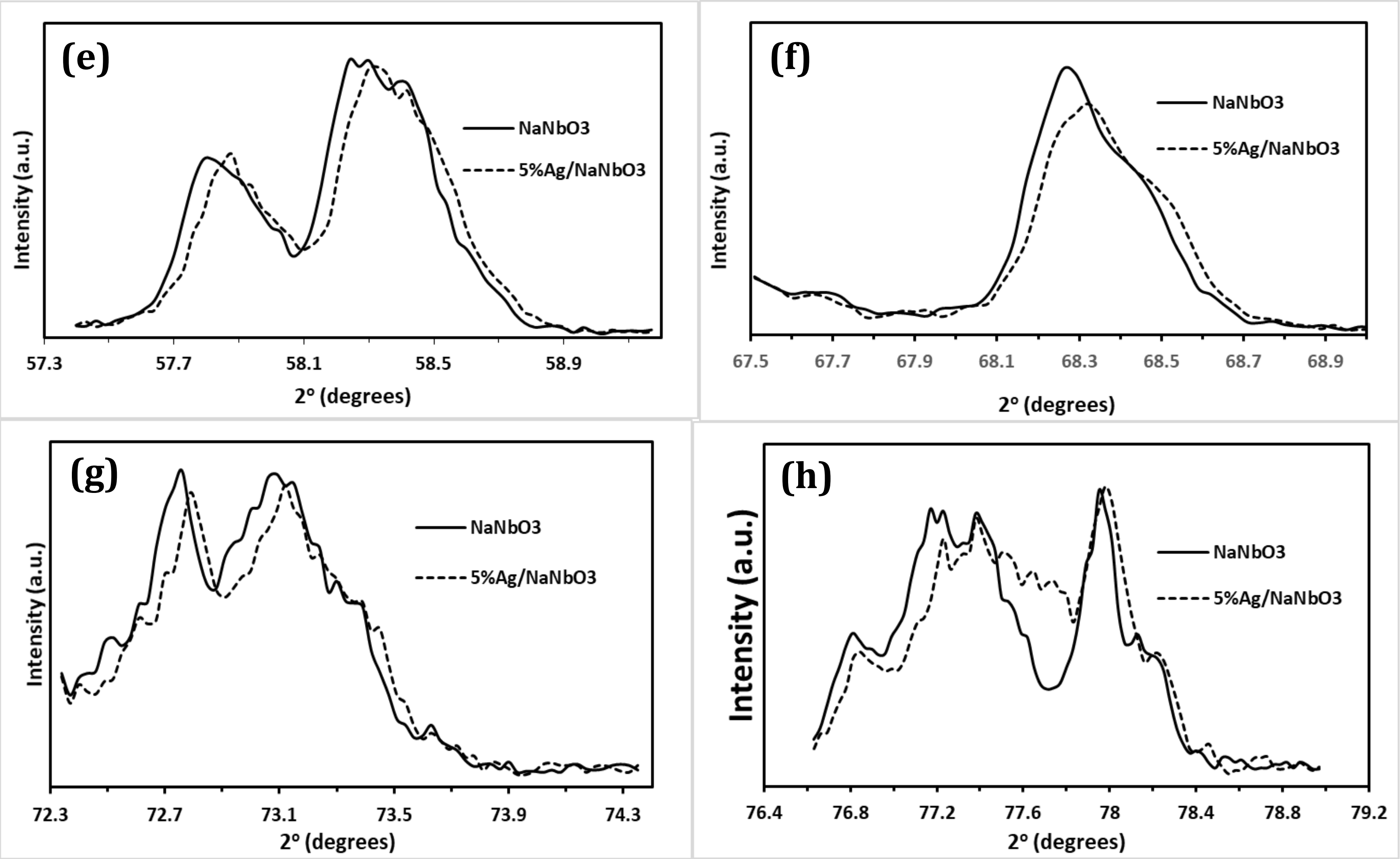

Fig. 4.13(e) – (h) XRD spectra of pure and Ag-loaded NaNbO$_3$ showing lateral peak shifts at 58.3^{o}, 68.3^{o}, 72.8^{o} and 78.0^{o}

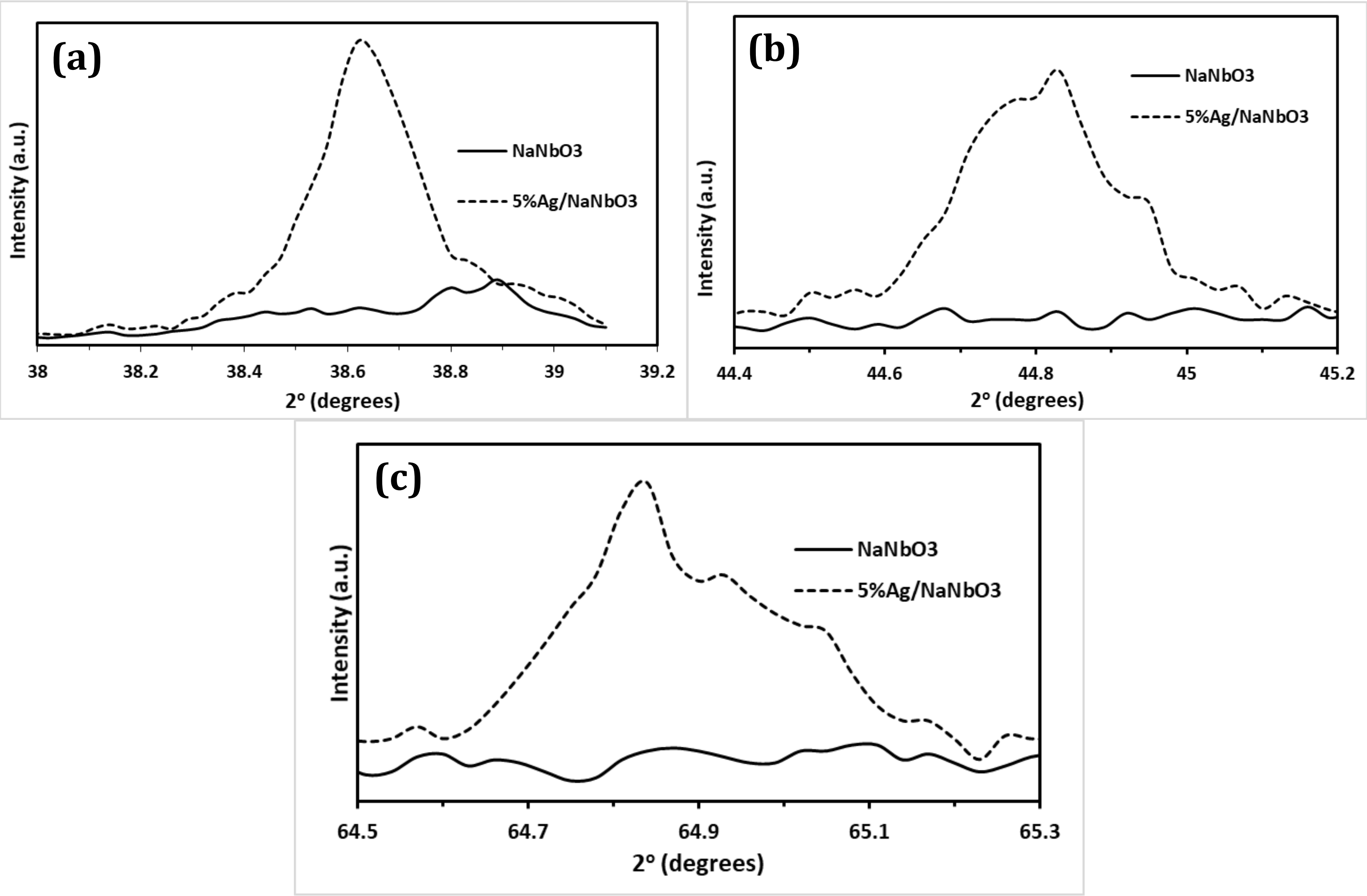

Fig. 4. 14 (a) – (c) XRD spectra of pure and Ag-loaded $NaNbO_3$ showing new peaks at 38.6°, 44.8° and 64.8°.

4.3.2 Morphological Properties

Fig. 4.15 and 4.16 shows the scanning electron microscope (SEM) images of pure and Ag-loaded $NaNbO_3$ respectively, at various magnification settings. The images show well-developed, somewhat rounded particles having an average size of 1 μm. The particle morphology is predominantly categorised by a rectanguloid shape with somewhat smoothened and flattened edges. The presence of silver is not obvious from the SEM images alone, hence we refer to the EDS elemental mapping of pure $NaNbO_3$ [Fig. 4.17(a) – (c)] and Ag-loaded $NaNbO_3$ [4.18(a) – (d)], which show excellent homogeneous distribution of the various elements (Na, Nb, O, Ag). More significantly, silver [Fig. 4.18(d)] is also well scattered throughout the area of observation, indicating the well-dispersed presence of silver in the $NaNbO_3$ lattice. The EDS elemental spectra confirm the presence of the expected elements in pure [Fig. 4.17(d)] and Ag-loaded $NaNbO_3$ [Fig. 4.18(e)], as shown by the various elemental peaks.

Table 4.5 gives the percentage elemental composition by mass for both pure and Ag-loaded $NaNbO_3$. There is good qualitative agreement between the theoretical (calculated from the stoichiometric formula) and experimental values obtained from EDS elemental analysis data. Most importantly, the actual, experimental silver loading by mass is approximately 5% in Ag-loaded $NaNbO_3$, which was indeed the stoichiometric loading during synthesis. This indicates that our Ag-loaded photocatalyst contains approximately 5% silver by mass.

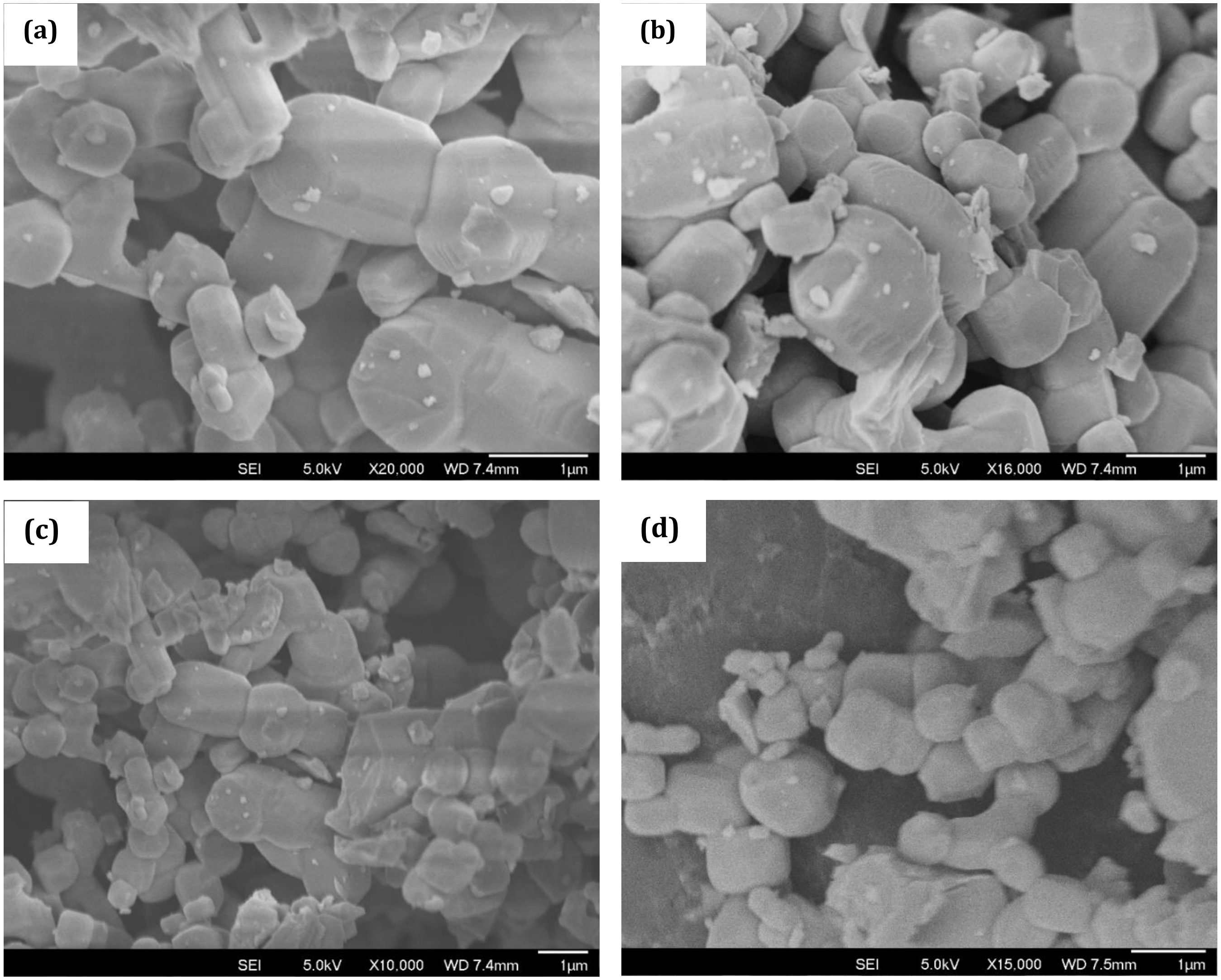

Fig. 4. 15 (a) – (d) Scanning electron microscopy images of pure $NaNbO_3$ at various magnification.

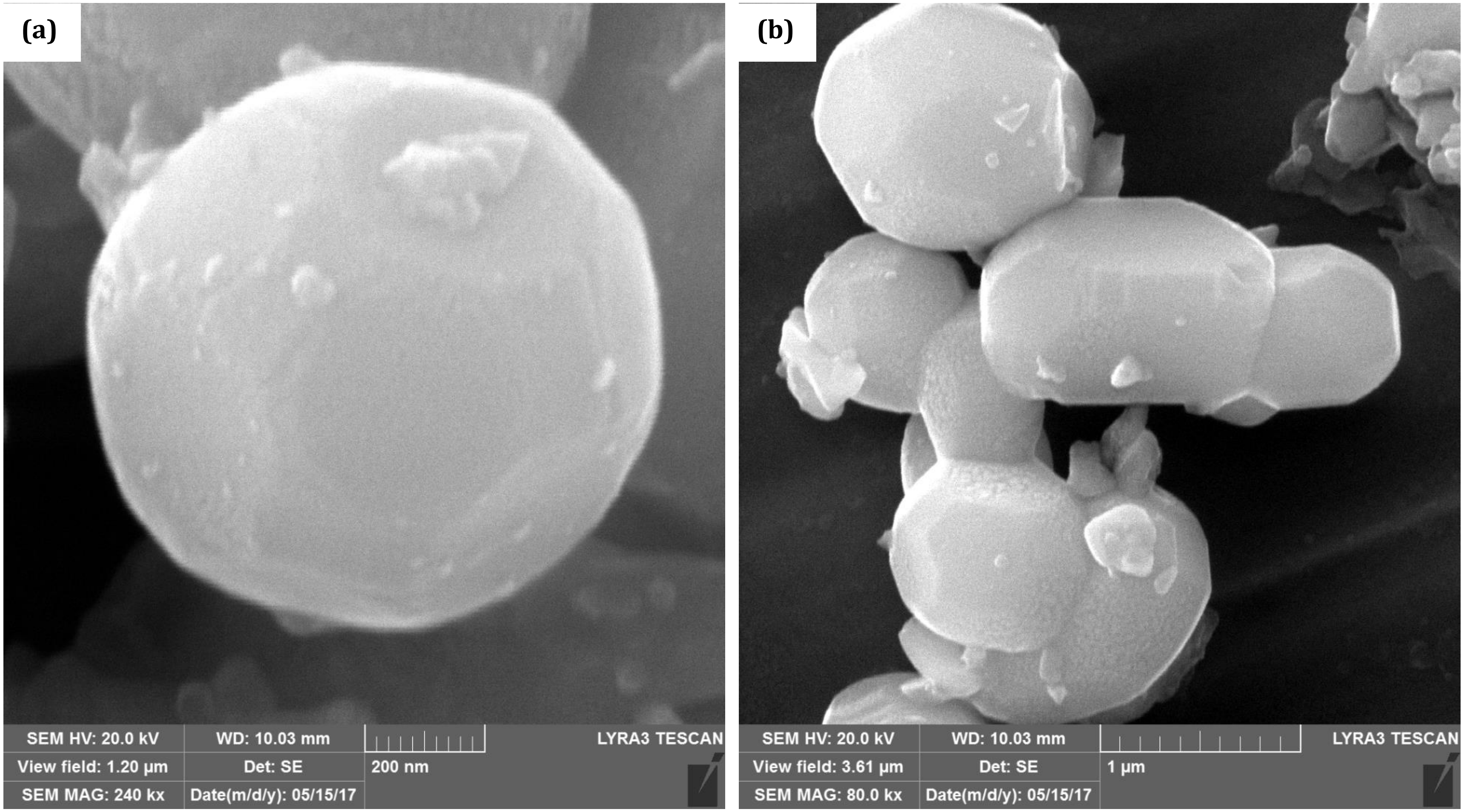

Fig. 4.16 (a) – (b) Scanning electron microscopy images of Ag-loaded $NaNbO_3$ at various magnifications.

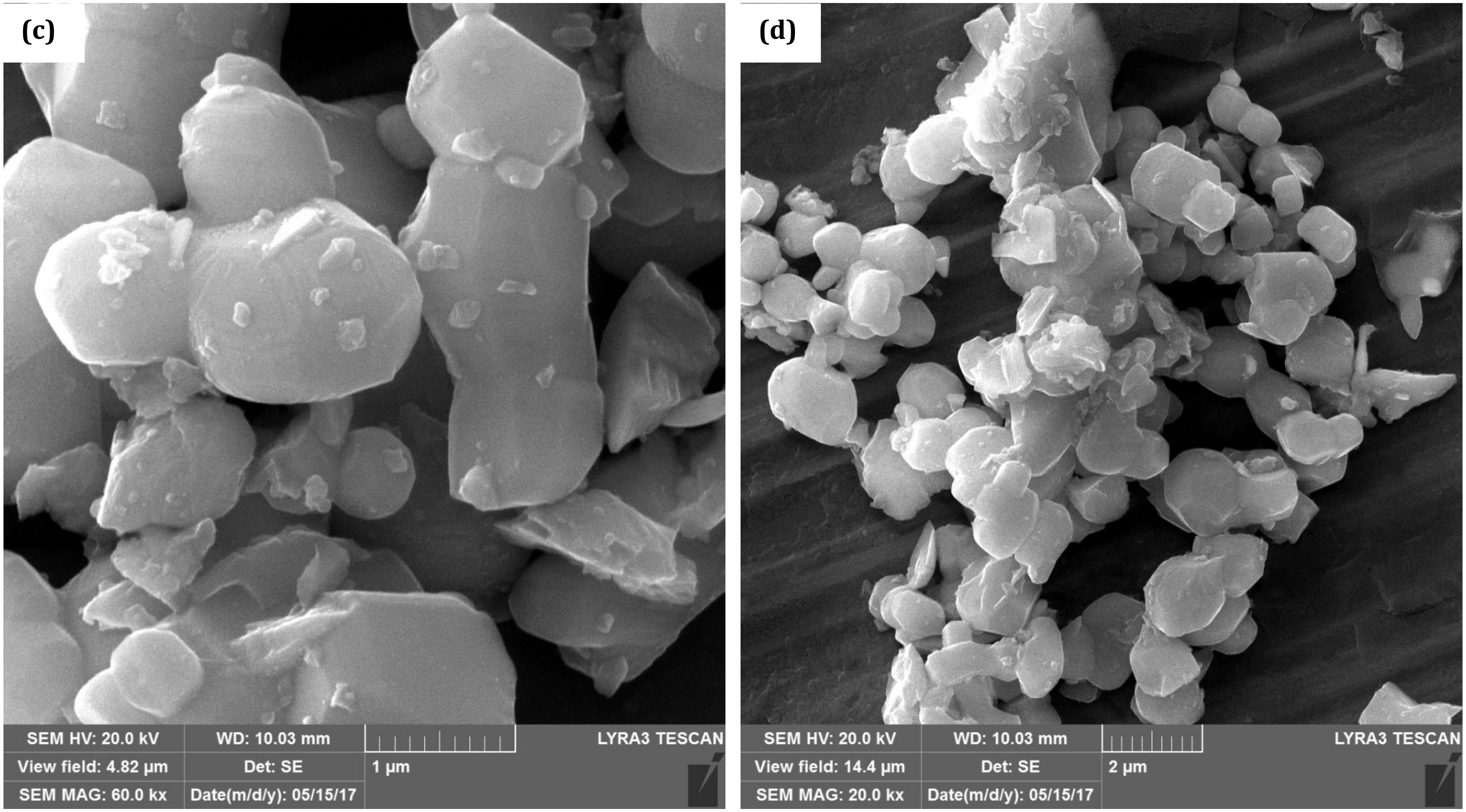

Fig. 4.16(c) – (d) Scanning electron microscopy images of Ag-loaded $NaNbO_3$ at various magnifications.

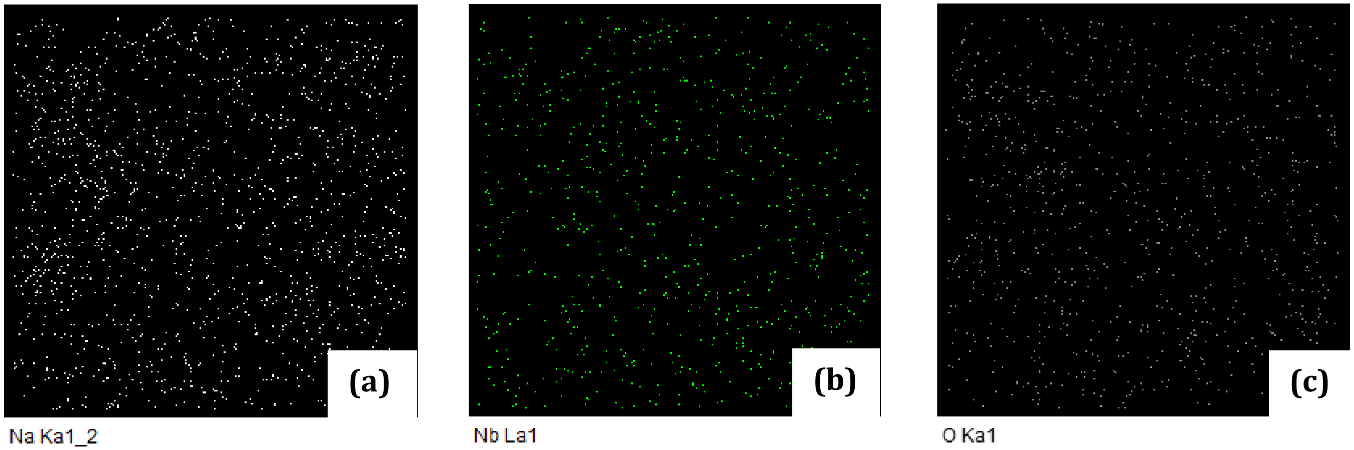

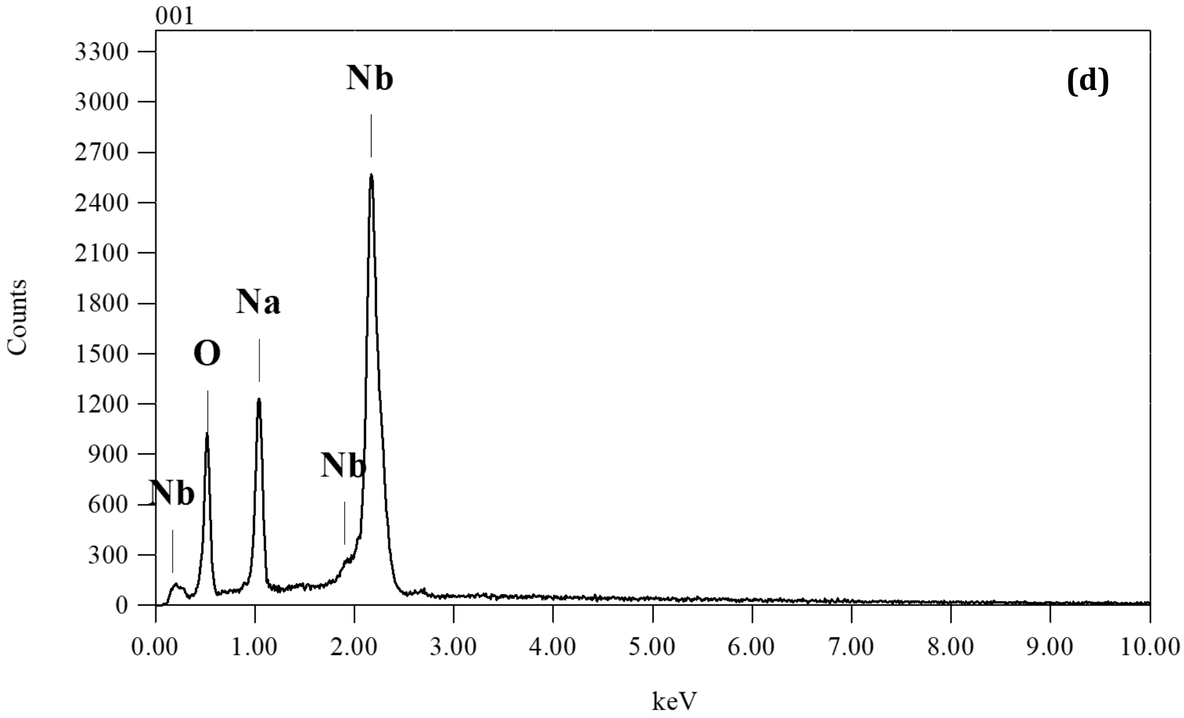

Fig. 4.17 Elemental mapping [(a) – (c)] and EDS elemental analysis (d) of pure $NaNbO_3$

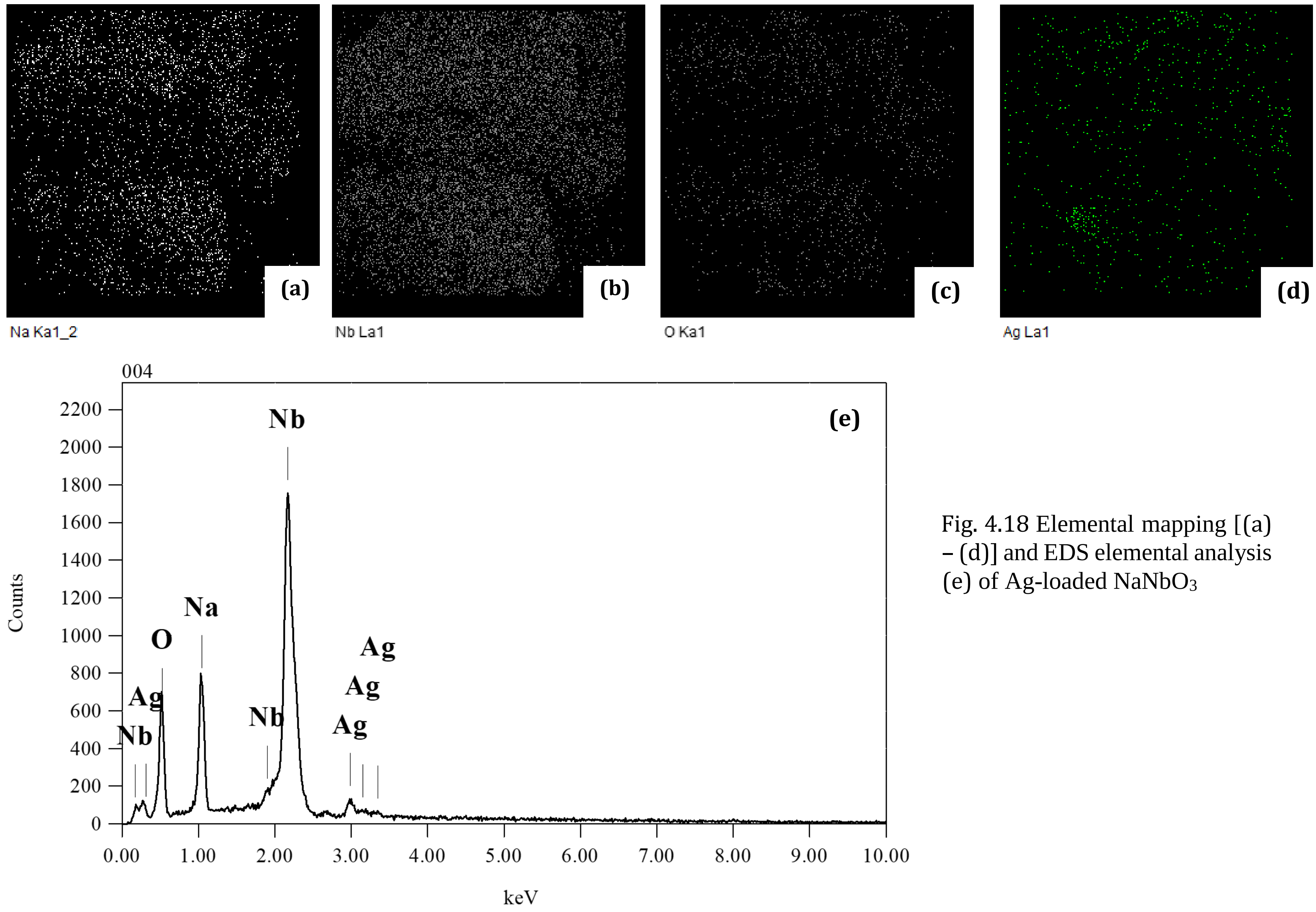

Fig. 4.18 Elemental mapping [(a) – (d)] and EDS elemental analysis (e) of Ag-loaded $NaNbO_3$

	O		Na		Nb		Ag	
	Theoretical	**Experimental**	**Theoretical**	**Experimental**	**Theoretical**	**Experimental**	**Theoretical**	**Experimental**
$NaNbO_3$	29.29	30.34	14.03	13.14	56.68	56.52	-	-
$Ag/NaNbO_3$	27.82	29.29	13.33	10.84	53.85	54.60	5.00	5.27

Table 4.5 Theoretically-calculated (based on stoichiometric formula) and experimentally-obtained (by EDX elemental analysis) composition of pure and Ag-loaded $NaNbO_3$ by mass

4.3.3 Electron Properties

To investigate the chemical state of the as-prepared samples, XPS measurements were carried out and the results are shown in Fig. 4.19, where the spectra results indicate the Na 1s, Nb 3d, O 1s and Ag 3d energy levels of pure and Ag-loaded $NaNbO_3$. As shown in Fig. 4.19(a), the peak located at 1072.5 eV corresponds to the binding energy of Na 1s in $NaNbO_3$ which is in agreement with the literature value of ~1071 eV [220].

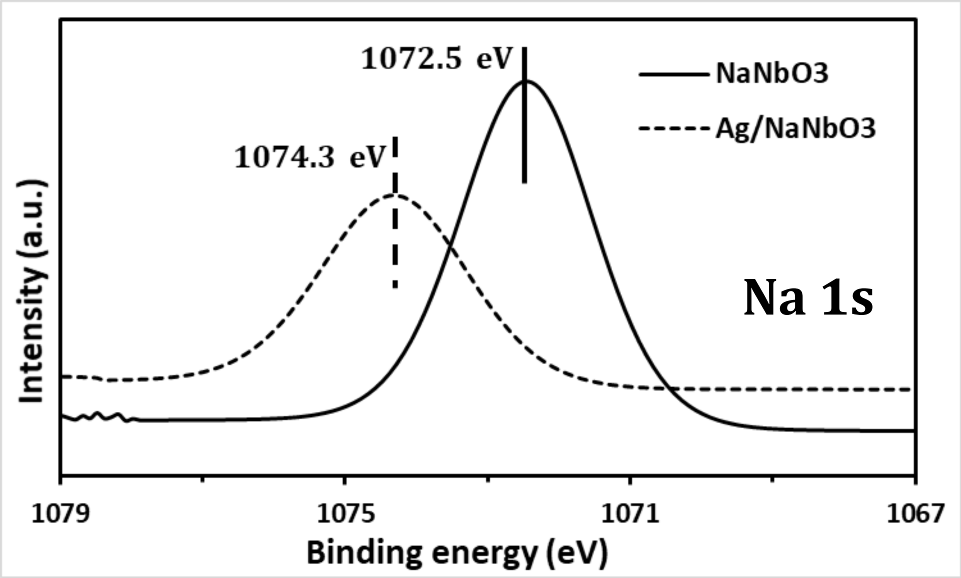

Fig. 4.19 (a) XPS Na 1s peak of pure and Ag-loaded $NaNbO_3$

For the Nb 3d peak doublet presented in Fig. 4.19(b), our results are 205.5 eV (Nb $3d_{5/2}$) and 208.0 eV (Nb $3d_{3/2}$), which represents a systematic deviation of 2.5 eV from the literature values of 208.0 eV (Nb $3d_{5/2}$) and 210.5 eV (Nb $3d_{3/2}$) [220]. Compared to those of pure $NaNbO_3$, the Nb 3d peaks of Ag-loaded $NaNbO_3$ migrate to the direction of stronger binding energy, indicating the strong interaction of silver particles with the $NaNbO_3$ lattice. This greatly facilitates the interfacial electrons transfer from the photocatalyst to the silver particles [221]. We have not thus far been able to ascertain the cause of this systematic deviation of 2.5 eV, and resolving it forms an integral part of our future plans.

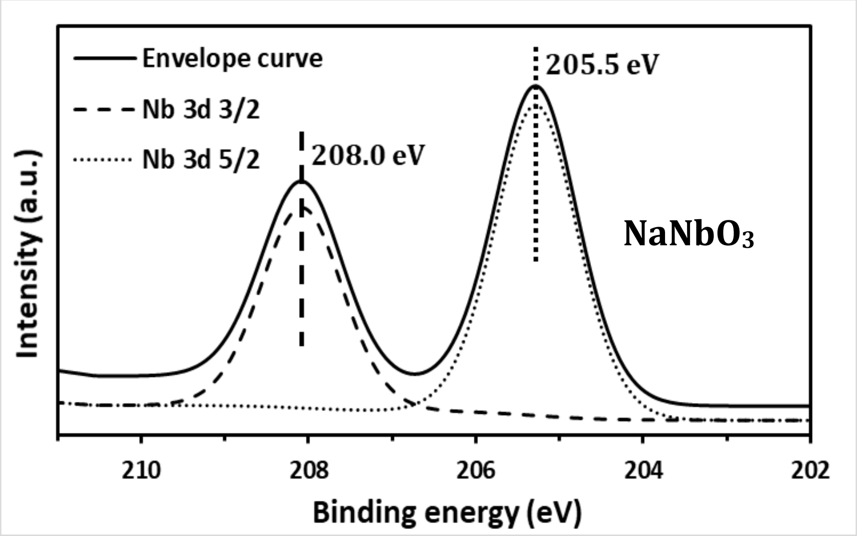

Fig. 4.19(b) XPS Nb 3d peak of pure $NaNbO_3$

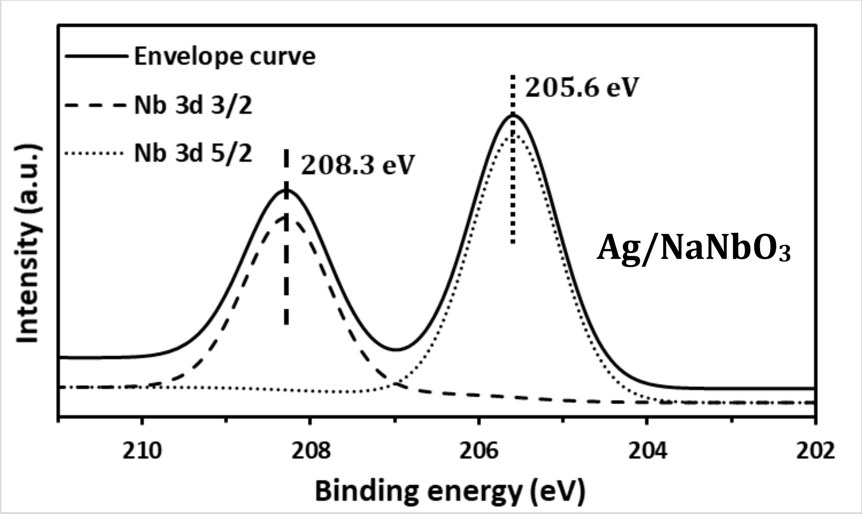

Fig. 4.19(c) XPS Nb 3d peak of Ag-loaded $NaNbO_3$

The O 1s can be deconvoluted by 2 curves (O 1s A & B – Fig. 4.19(d)) in the pure sample, and 3 curves (O 1s A, B & C – Fig. 4.19(e)) in the Ag-loaded one, indicating that oxygen exists in 2 and 3 oxidation states in the pure and Ag-loaded samples respectively. The 2 common peaklets (O 1s A and O 1s B) have almost the same binding energy (A: 531.9 vs 532.0 eV; B: 528.8 vs 528.9 eV) in both samples, implying self-consistent results. They are assigned to the oxygen in H_2O (adsorbed water) and $NaNbO_3$ respectively, which are 532.8 eV [222] and 529.7 eV [223]. The unique O 1s C peaklet at 530.5 eV, which exists only in Ag-loaded $NaNbO_3$, is assigned to Ag_2O, whose binding energy is roughly 530.9 eV [224]. This concurs with the hypothesis under the XRD results, which alluded to the presence of Ag_2O.

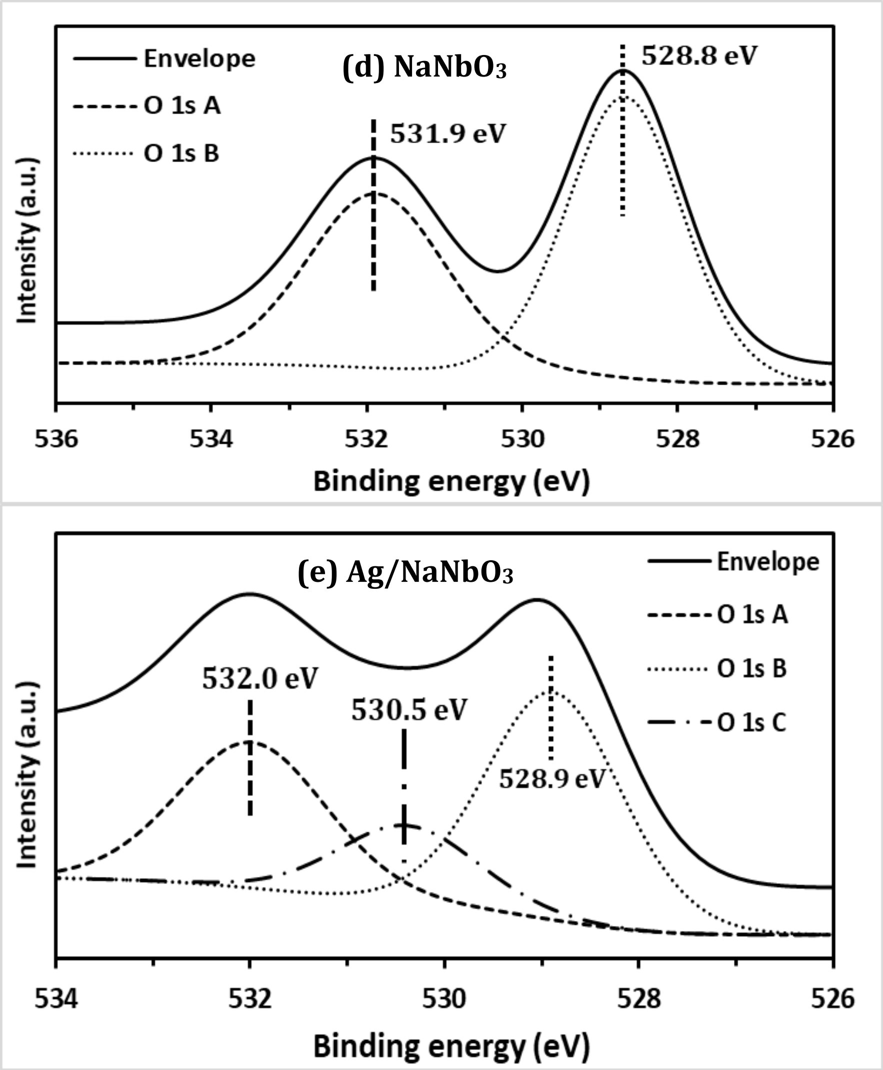

Fig. 4.19 (d), (e): XPS O 1s peak of (d) pure $NaNbO_3$ and (e) Ag/$NaNbO_3$

The assignment of the Ag 3d orbitals (Fig. 4.19(f)) is far less trivial; hence, we referred to the NIST XPS database [225]. The database values for both orbitals ($3d_{5/2}$, $3d_{3/2}$) are given for all realistic options (Ag, AgO, Ag2O). It is clear that there is significant variance even in the database values for each orbital, hence exact values are difficult to attain in XPS analysis. Based on the database values, and keeping in mind the previous observation that there is an underestimate of ∼ 1–3 eV in our XPS values, we arrive at Table 4.6, where we offer postulated assignments for 3 of our peaklets (B, C and D). No suitable assignments were found for peaklet A till date. In retrospect, the assignment of the Ag 3d orbitals is still far from complete, and completing this assignment forms part of our plans for continued research in this exciting endeavour.

Formula	Orbital	NIST Database (eV)	Possible matches
Ag	$3d_{5/2}$	367.9 – 368.4	D (363.7 eV)
Ag	$3d_{3/2}$	373.4 – 374.2	B (372.3 eV)
AgO	$3d_{5/2}$	367.3 – 368.1	C (366.3 eV)
AgO	$3d_{3/2}$	Data not available	–
Ag_2O	$3d_{5/2}$	367.7 – 368.4	C (366.3 eV)
Ag_2O	$3d_{3/2}$	373.9	B (372.3 eV)

Table 4. 6 Postulated assignment of XPS Ag 3d peaks of Ag-loaded $NaNbO_3$

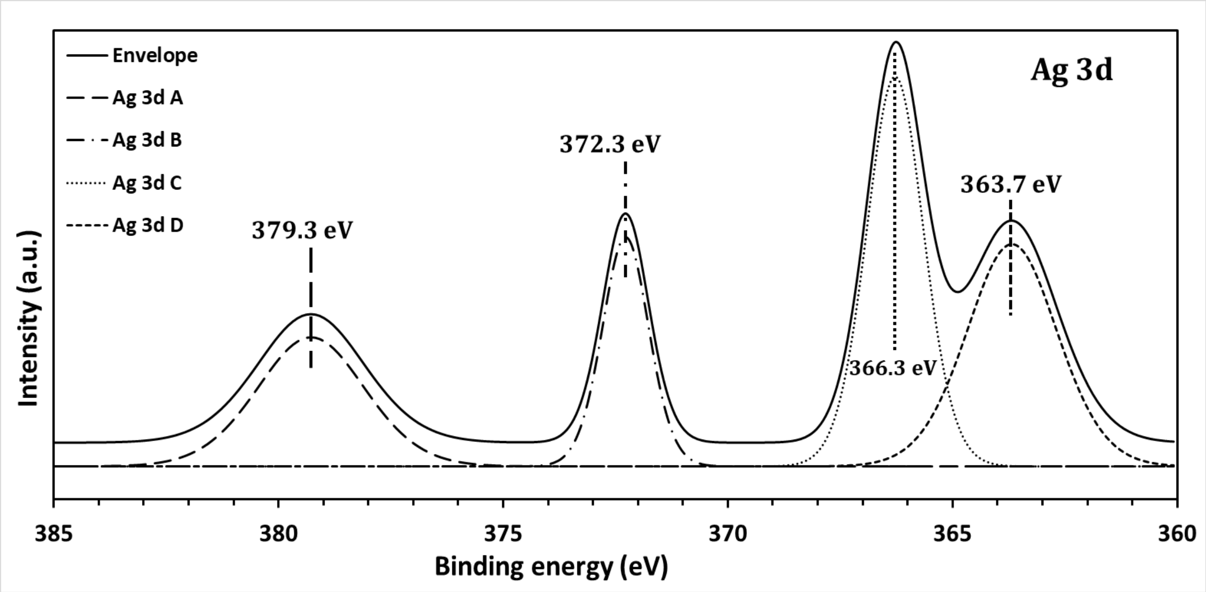

Fig. 4.19(f) XPS O 1s peak of Ag-loaded $NaNbO_3$

4.3.4 Optical Properties

Photoluminescence (PL) spectroscopy has been investigated to verify the separation efficiency of the photoinduced electron−hole charge carrier pairs. The theory connecting PL spectroscopy and electron−hole recombination is as follows. When a photon strikes a photocatalyst, an electron is promoted from the valence band to the conduction band, leaving a hole in the valence band. This electron – hole pair causes reduction and oxidation reactions to occur, respectively, on the photocatalyst surface, provided the electron can migrate to the surface rapidly enough where it catalyses, say, CO_2 reduction. However, if the electron mobility is too low, instead of migrating to the surface, it may de-excite back to the valence band and recombine with the hole therein [226]. This downward electron transition results in a photon emission, which is measured by the PL spectrometer. Hence, a lower PL output corresponds to a lower rate of electron – hole recombination.

For this purpose, the PL spectra of pure and Ag-loaded $NaNbO_3$ were recorded and are shown in Fig. 4.20, where both samples exhibit similar emission profiles (similar shapes and peaks positions) under an excitation wavelength of 300 nm. The main part of the spectra is composed of a broad emission band in the 370–460 nm region, as is generally observed in ABO_3 perovskites [227], and is formed by several contributions related to excitons and oxygen vacancies [228].

In agreement with the aforementioned theory, several groups observe that a higher PL intensity implies greater recombination of electron−hole pairs, leading to lower photocatalytic activities [229-231]. Remarkably for Ag/$NaNbO_3$, the PL emission intensity was lower than that of pure $NaNbO_3$ at similar emission wavelengths. The spectra presented in Fig. 4.20 are based on the absolute numbers obtained directly from the spectrometer, without performing any artificial rescaling or shifting, to ensure that the 2 spectra can be fairly compared against each other. Based on this information, we can conclude that the Ag-loaded $NaNbO_3$ has a substantially lower recombination rate of photogenerated charge carriers, which possibly originates from the rapid charge transfer between the silver and $NaNbO_3$. Owing to the superior conductivity of silver, there is excellent electron transport across the metal-semiconductor interface, which facilitates the charge transfer process [232]. Silver particles possibly act as electron-trapping centres, whereby electrons are momentarily stabilized within the silver lattice and thus prevented from recombination, leading to enhanced electron density on the silver particle surface. This point, on enhanced electron density, will be investigated more deeply in sub-section 5.3.2.2.

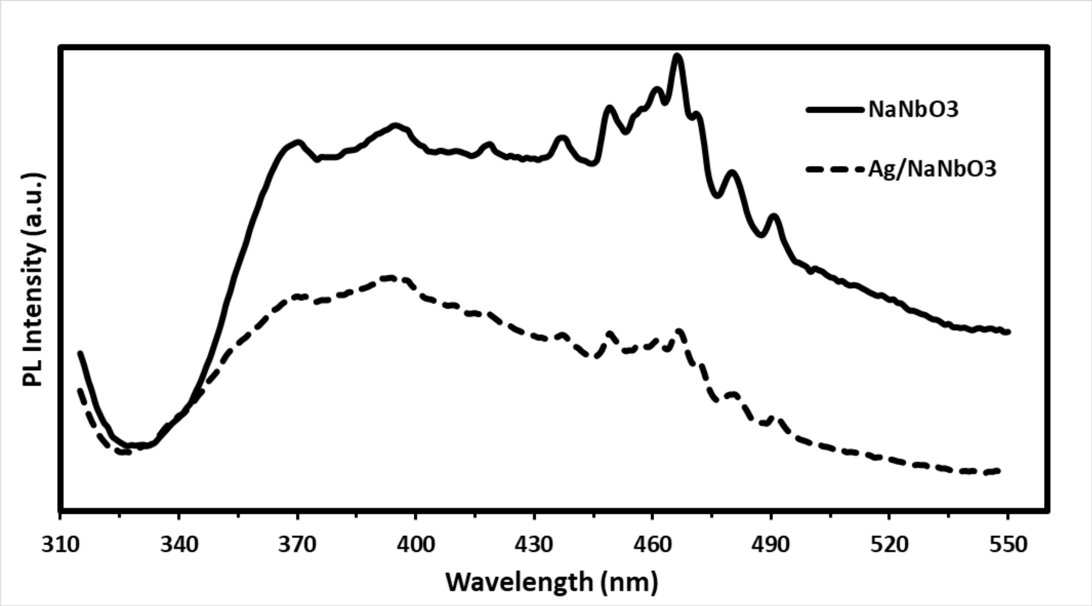

Fig. 4.20 PL spectra of pure and Ag-loaded $NaNbO_3$

Raman spectroscopy has been investigated to verify changes in vibrational modes arising from the silver loading. The strong Raman band at ~600cm^{-1} corresponds to the stretching mode of NbO_6 octahedron [233]. After Ag particles were incorporated into the $NaNbO_3$ lattice, this characteristic band shifts to a lower wavenumber and is remarkably broadened (Fig. 4.21). To understand the physical interpretation of Raman band broadening/shifting, we refer to the literature. Qianqian Liu et al [221] observe that the "shift and broadening [of the Raman spectra] can be assigned to the incorporation of Pt nanoparticles into the $NaNbO_3$ lattice", which is consistent with our Raman spectra. Unfortunately, the detailed underlying mechanism of why metal dopants cause Raman peaks to broaden has not been clarified in the literature yet. Nonetheless, we hypothesize that the peak broadening arises due to the energy level transitions losing its discreteness. In general, as is well known, sharp, narrow peaks correspond to discrete energy level gaps. Conversely a broadened peak implies that the initial and/or final energy levels have smeared out, or become less discrete, leading to broadened Raman peaks. The exact reason why adding metal atom causes the peaks to lose discreteness is not clear yet, and understanding it forms part of our plans for future research.

In addition, it is known that the Raman shifts near 600 cm^{-1} is closely related to the Nb-O bond lengths in crystalline inorganic niobate compounds. A lower wavenumber for the Raman stretching bands corresponds to longer Nb-O bond lengths [234]. Thus, the observed shifts can be ascribed to changes in the Nb-O bond lengths Again, the detailed physical reason for the increased bond length has not been expounded upon yet in the literature. However, we hypothesize that the difference in atomic radii between silver and the original atoms (Na, Nb, O) perturbs the pure $NaNbO_3$ lattice, causing its atoms to be pushed further apart, which increases the equilibrium bond length. This hypothesis can be tested by performing numerical computations that calculate the bond length of $NaNbO_3$ from first principles, and then studying the effect of adding dopant silver atoms on the bond length values. This is a suitable test for the above hypothesis.

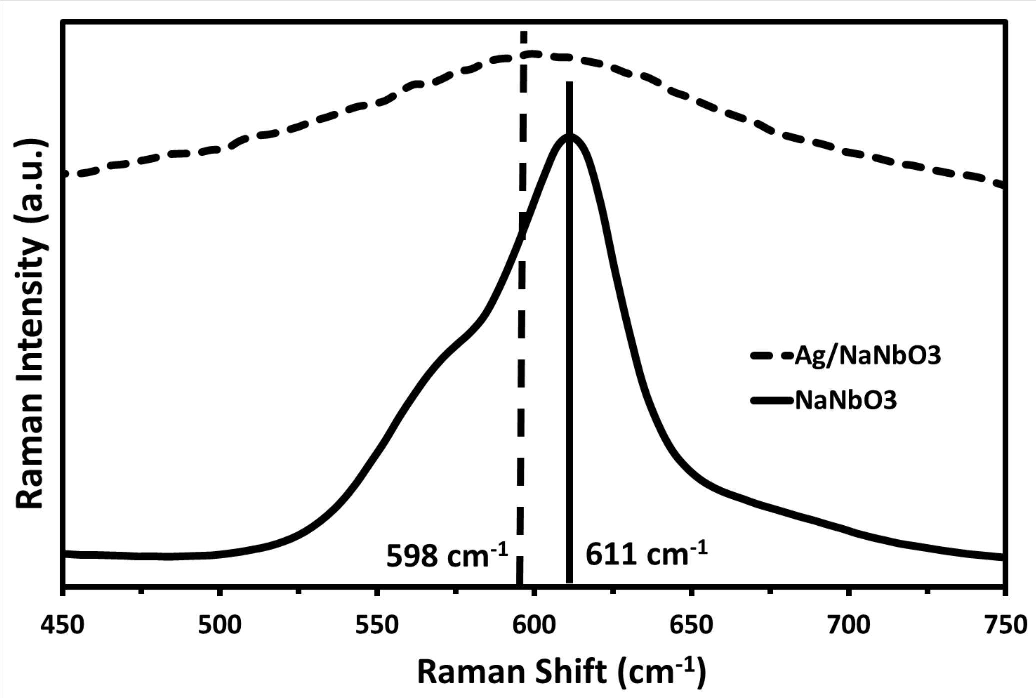

Fig. 4.21 Raman spectra of pure and Ag-loaded $NaNbO_3$

Moving on, it has also been reported that the O 2p and Nb 4d orbitals mainly contribute to the formation of the valence and conduction bands of $NaNbO_3$ respectively [235]. Therefore, the changes in the NbO_6 octahedral local structure, such as Nb-O bond lengths, may influence the band structure of $NaNbO_3$, thus resulting in the variation of the optical band gap, which will be discussed in the UV-vis results part hereunder.

The optical absorption properties of pure and Ag-loaded $NaNbO_3$ were measured by UV–vis diffuse reflectance spectra analysis using the Kubelka-Munk function, which has been elaborated upon in section 4.2. As shown in Fig. 4.22, pure $NaNbO_3$ absorbs incident radiation mainly in the near UV region, with an absorption edge of approximately 365 nm, which is consistent with other reports [236]. Compared with pure $NaNbO_3$, the Ag-loaded $NaNbO_3$ exhibits enhanced photoabsorption in the whole visible light region (400–800 nm), along with a marginally reduced band gap (3.3 → 3.2 eV). This can be attributed to the strong interaction between the metal particles and the semiconductor photocatalyst $NaNbO_3$, which has already been suggested by XRD and Raman spectroscopy. The decreased band gap of Ag-loaded $NaNbO_3$ means that more lower-energy radiation can stimulate the photocatalysts to generate electron–hole pairs. Therefore, better photocatalytic performance of the composite can be expected by longer-wavelength electromagnetic radiation.

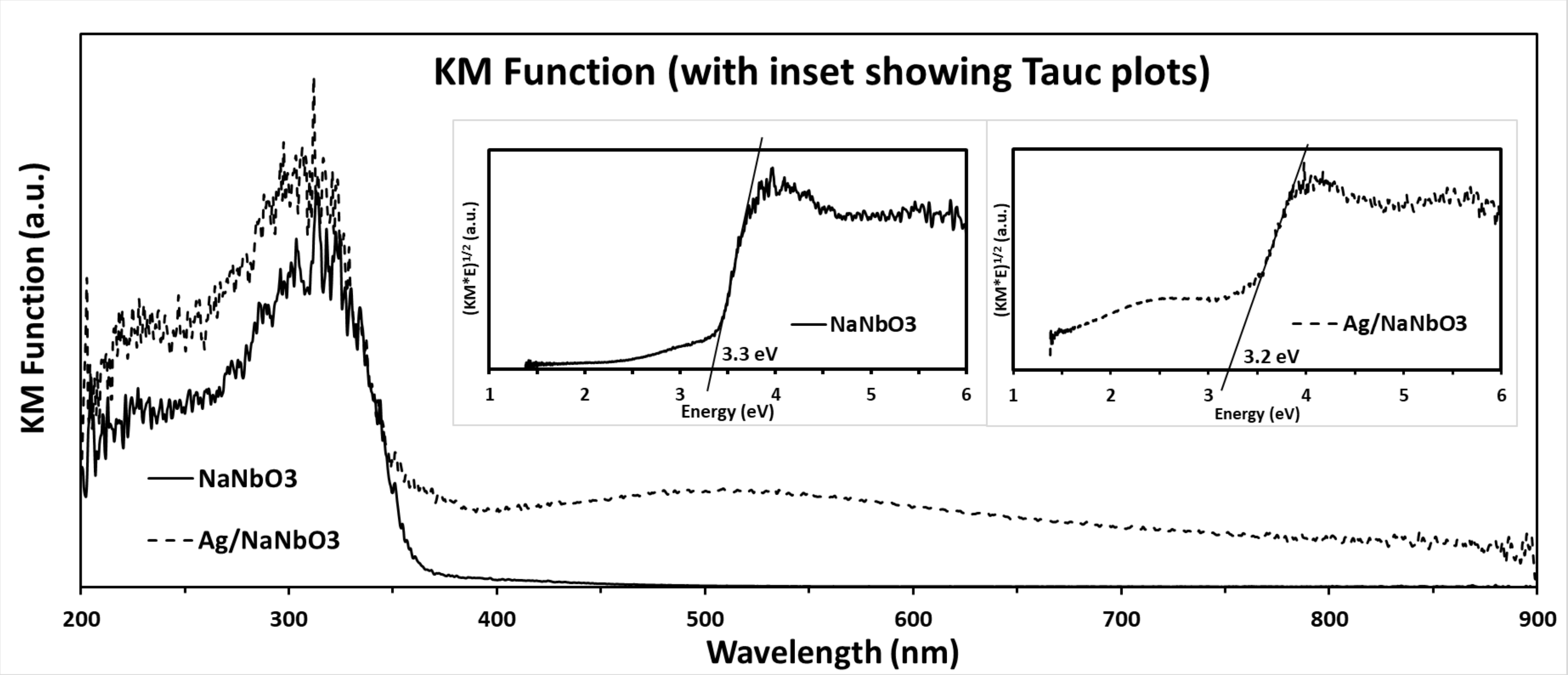

Fig. 4. 22 Kubelka-Munk functions of pure and Ag-loaded $NaNbO_3$ (with Tauc plots as insets)

CHAPTER 5

Photocatalytic CO_2 conversion to fuels

5.1 Overview of results

In this chapter, we present the photocatalytic CO_2 conversion to fuel results pertaining to the following photocatalysts:

(a) graphitic carbon nitride (g-C_3N_4) as the solar-harvesting photocatalyst (section 5.2), and

(b) Ag-loaded $NaNbO_3$ as the methanol-selective photocatalyst (section 5.3).

5.2 Solar harvesting graphitic carbon nitride

5.2.1 Methanol production yield

Using the visible-light responsive, solar-harvesting graphitic carbon nitride, we conducted CO_2 photocatalytic reduction reactions using three radiations and the results are presented in Fig. 5.1. The radiation sources are as follows: (i) 355-nm pulsed laser beam, which is the third harmonic of the Spectra Physics (Model GCR 250) Nd: YAG laser; (ii) Newport Xe–Hg lamp; and (iii) natural solar radiation. All other variables (CO_2 concentration, catalyst loading, illumination time, reactor geometry etc.) were kept constant for this part, and only the illumination source – the independent variable – was varied for this experiment.

From Fig. 5.1, we observe that, for all three radiation sources, the methanol yield initially increases with irradiation time, reaches a maximum and then starts to decline. For the laser radiation, the maximum methanol yield achieved is 510 μmol g^{-1} after 40 minutes of irradiation, and the corresponding values for solar radiation and the UV lamp are 130 μmol g^{-1} and 40 μmol g^{-1} respectively. The best-performing laser radiation is due to its characteristically high photon intensity and high beam collimation. However, the most encouraging result achieved with g-C_3N_4 is its capability reduce CO_2 to methanol using inexpensive and abundant solar radiation. To place these figures in a broader context, the methanol yield achieved by our catalyst is much higher than the reported values using Ag-doped TiO_2 (1.5 wt% Ag), Ag-doped AgCl and Cu-In_2O_3/TiO_2 with the methanol yields of 4 μmol g^{-1} h^{-1} [237], 38 μmol g^{-1} h^{-1} [238] and 40 μmol g^{-1} h^{-1} [239] respectively. Hence, this indicates that graphitic carbon nitride is potentially a suitable photocatalyst for large-scale solar harvesting. There are many requisites a catalyst must satisfy before it can be considered for industrial-scale photocatalysis of CO_2 to fuels, of which one is that the photocatalyst must be solar-responsive, so that it can utilise the abundant and ubiquitous solar radiation to convert CO_2 into fuels. The successful testing of the graphitic carbon nitride catalyst using natural solar radiation above indicates that it can potentially be used for large scale solar harvesting.

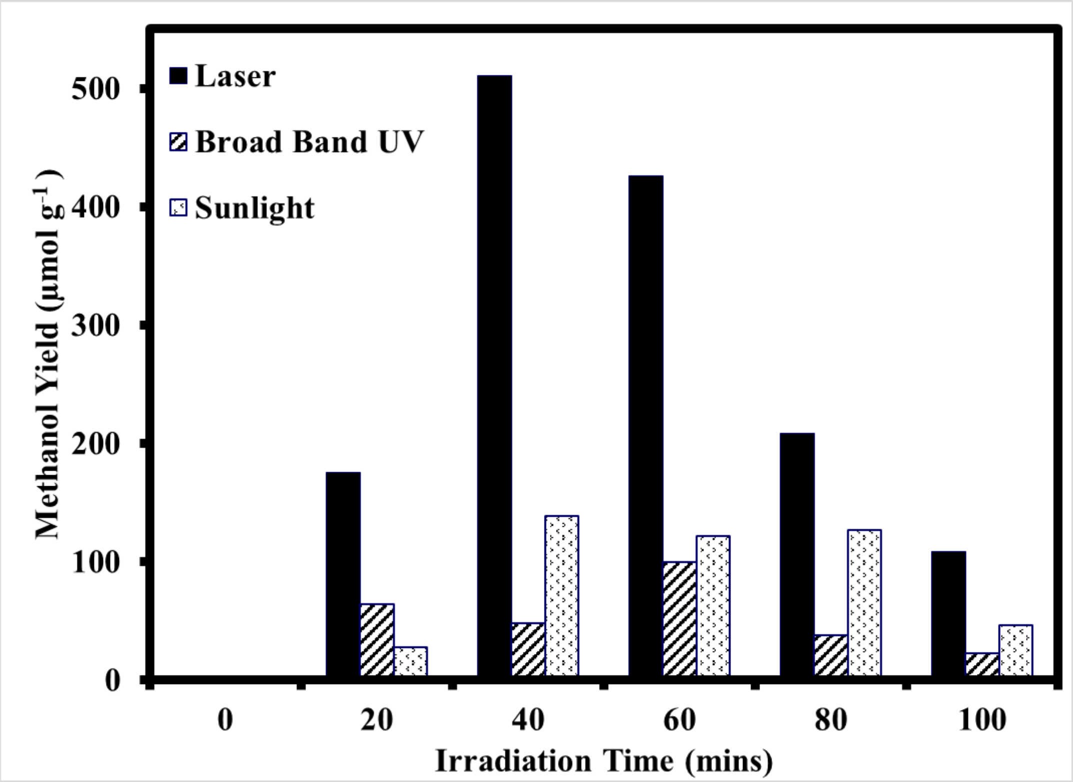

Fig. 5.1 Methanol yield at different irradiation times.

The decreasing methanol yield, after 40 minutes of irradiation (see Fig. 5.1), can be attributed to the photo-catalytic oxidation (or degradation) of methanol back to CO_2, which has reportedly been used to test the performance of a photocatalyst [240]. This undesired back reaction occurs because hydrocarbon products like methanol have higher solubility and reactivity in water than CO_2. Methanol has higher reactivity than CO_2 because methanol oxidation (Equation 5.2) is thermodynamically favourable (exothermic) whilst CO_2 reduction (Equation 5.1) is thermodynamically unfavourable (endothermic).

$$2CO_2 + 4H_2O \longrightarrow 2CH_3OH + 3O_2 \qquad (5.1)$$

$$2CH_3OH + 3O_2 \longrightarrow 2CO_2 + 4H_2O \qquad (5.2)$$

Hence, for batch-phase experiments, the methanol formed is eventually expected to degrade back to CO_2, unless it is simultaneously harvested during production, i.e. removed from the reactor before it can undergo degradation to CO_2. This necessitates research in the field of continuous-flow photoreactors, whereby the products formed are removed without degrading. This forms part of our future plans for further research.

As for the dependence of methanol yield on various light sources, the 2 primary factors are the geometric and spectral characteristics of the illuminations source. Firstly, the illumination source must have a large intensity in the high-photon-energy region, to ensure that the maximum amount of photons can be utilised by the photocatalyst. The threshold wavelength for graphitic carbon nitride is 458 nm (corresponding to 2.7 eV); hence, only photons having energy in excess of this threshold figure can effect photocatalytic conversion of CO_2 to fuels. We hypothesize that the laser has the largest integrated power in the ultraviolet region ($\lambda < 458$ nm), followed by the sun and lastly the UV lamp. This hypothesis can be tested by using an electromagnetic spectrum analyser to find the integrated power ($\lambda < 458$ nm) for each illumination source.

Secondly, geometric factors also play a part in affecting the methanol yield. Since the laser radiation is highly collimated, it is able to illuminate the entire reactor volume more effectively, compared to the UV lamp and sun, whose beams undergo substantial divergence and thus may not be able to illuminate the entire reactor volume as completely as in the case of the laser beam.

5.2.2 Quantum efficiency

Quantum efficiency is a benchmark parameter commonly used to evaluate the efficiency of any photochemical reaction. It represents the ratio of the desired product of the photochemical process to the amount of incident photons. Several definitions exist in the literature, but the one recommended by the International Union of Pure and Applied Chemistry is [241]:

$$\Phi = \frac{\text{amount (mole) of methanol formed}}{\text{number of incident photons}}$$

The numerator term is easily available from the quantity of methanol produced, and denominator term for the laser beam can be reasonably estimated from the laser pulse energy, photon energy, and the duration of laser irradiation.

The variation of quantum efficiency with irradiation time, depicted in Fig. 5.2, is only for the laser radiation (we could not ascertain the denominator values for solar and broadband UV lamp to a reasonable degree of precision due to the broadband nature of their spectrum; hence, the values were not pursued further); the quantum efficiency starts from zero, attains a maximum value of 0.44% after 40 min of irradiation, starts to decrease, and finally, reaches 0.04% after 100 min of irradiation. A considerable methanol production yield with g-C_3N_4 in the presence of solar radiation is an encouraging result as the production of methanol can be achieved from abundant solar radiation, and this production yield might be further improved by proper materials engineering. However, the decline of the methanol production after certain duration of irradiation, because of the back-reaction, is a big challenge to be faced. Ideally, the quantum efficiency should remain constant for a long time in order to carry on this photochemical reaction uninterrupted, but because of the drop in quantum efficiency and consequent decline in the methanol yield, the reaction needs to be restarted quite frequently, which is not practical for mass production. Our future focus in this area of research is to explore the field of continuous-flow photoreactors, whereby the methanol formed is simultaneously harvested before degrading.

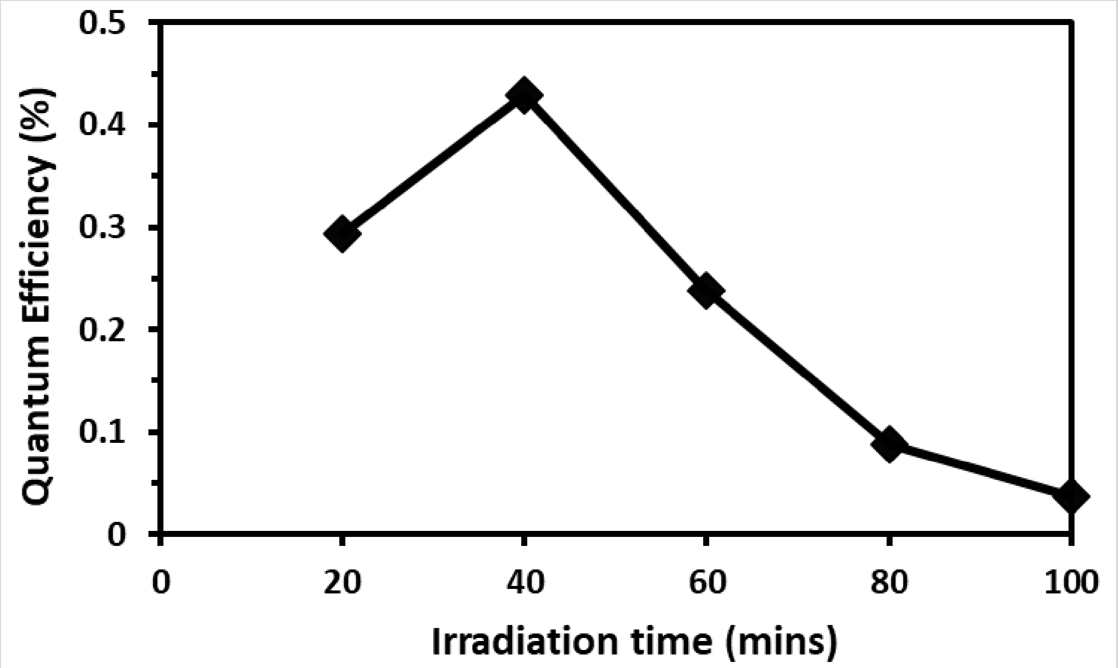

Fig. 5.2 Quantum efficiency of the photocatalytic process at different irradiation times.

5.3 Methanol selective Ag-loaded $NaNbO_3$

5.3.1 Hydrocarbon production yield

Using both pure and silver-loaded $NaNbO_3$ photocatalyst, 2 main products were observed, formic acid (Fig. 5.3) and methanol (Fig. 5.4). In general, both products displayed increasing yield as a function of time. However, the rate of increase slowed down with time and the concentrations appeared to approach a stationary state, possibly due to the back-reactions described in the previous section under graphitic carbon nitride. The most noteworthy trend is that silver loading tends to suppress the formic acid yield (by 40.1%) and enhance the methanol yield (by 60.2%). In other words the methanol product selectivity over formic acid is preferentially enhanced by adding silver. This will be addressed in detail in the subsequent sections.

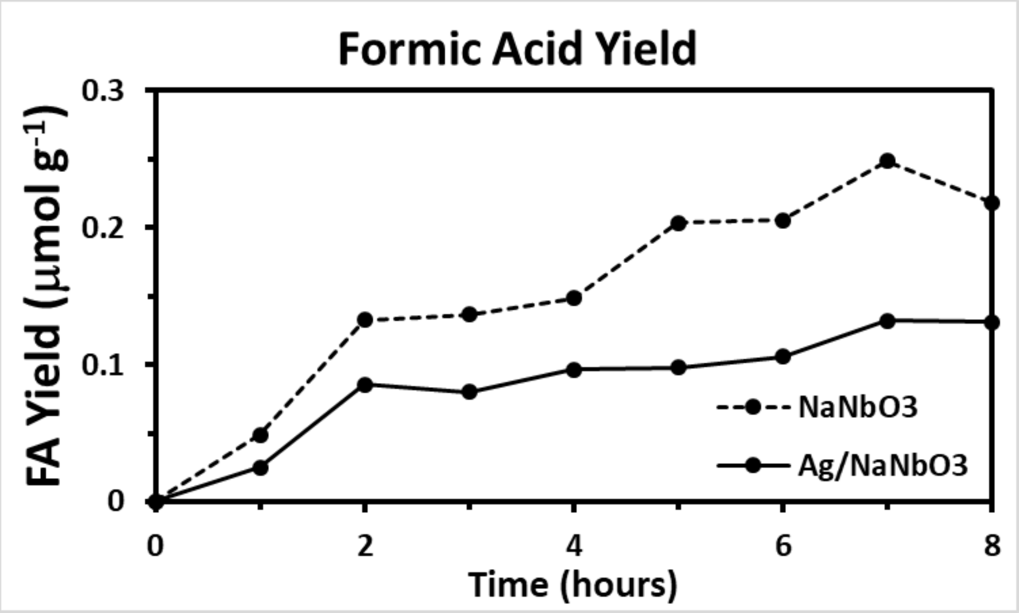

Fig. 5.3 Formic acid yield with respect to time.

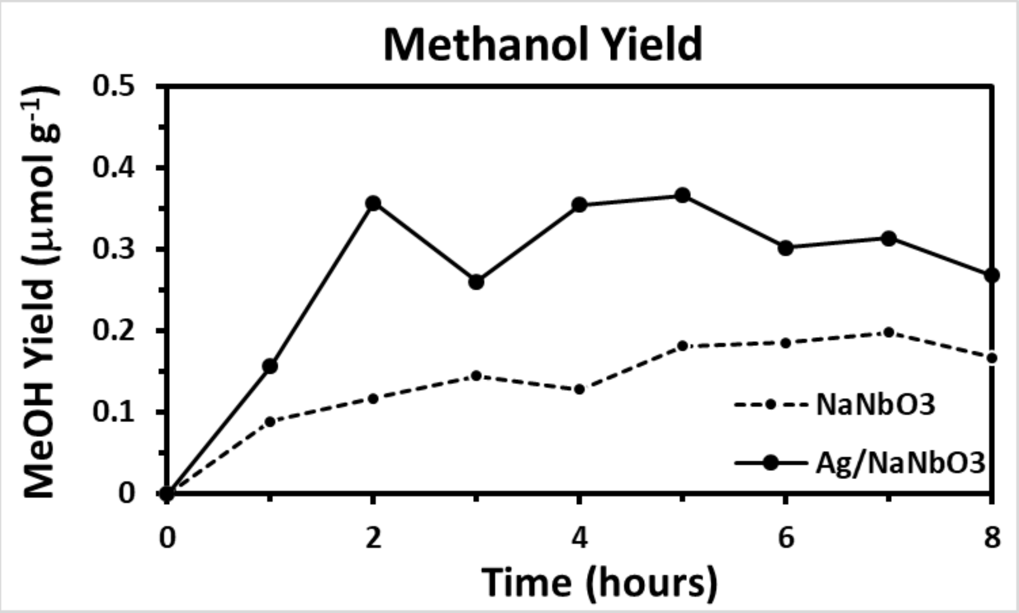

Fig. 5.4 Methanol yield with respect to time.

5.3.2 Theoretical investigation for enhanced methanol selectivity

It is very interesting to note that there has been a significant enhancement of the methanol product selectivity over formic acid upon loading silver particles onto the primary photocatalyst, $NaNbO_3$. A detailed explanation from first principles necessitates a rigorous understanding of the underlying reaction mechanism, which has eluded photocatalyst researchers thus far. We have conducted extensive literature review – which would be listed in the subsequent sub-sections – and have obtained 3 plausible reasons that account for the enhanced methanol product selectivity upon silver loading. In brief, the reasons pertain to silver:

(1) increasing the surface hydrophobicity,
(2) enhancing the electron density and
(3) changing the reactant binding mode.

These postulated causes have already been reported in connection with enhanced methanol product selectivity. Of course, which one, or perhaps even a combination of the above, applies to the specific case of silver loading onto $NaNbO_3$, is still uncertain, since the particular Ag-loaded $NaNbO_3$ photocatalyst has not been studied thus far. Further research using advanced empirical and computational techniques could be able to elucidate the atomic-level mechanism further, which would hopefully illuminate the real reason why silver improves the methanol product selectivity.

5.3.2.1 Surface hydrophobicity

The presence of metallic atoms can influence the product selectivity. Yamashita and co-workers [242] demonstrated improved selectivity for methanol formation with the addition of fluorine in titanium catalyst supported on mesoporous silica. Fluorination increases hydrophobicity of the photocatalyst surface, altering the product selectivity. Hydrophobic photocatalyst exhibited higher selectivity for longer chain hydrocarbons. For instance, hydrophilic Ti-Beta(OH) zeolites showed higher selectivity for CH_4, but hydrophobic Ti-Beta(F) zeolites demonstrated higher activity for the production of CH_3OH [243-245].

However, whilst the phenomenon of increasing hydrophobicity leading to enhanced product selectivity has been well-reported, the same cannot be said regarding the detailed reaction mechanism underlying this observation. Many groups note that hydrophobic photocatalysts hinder the access of water (lower H_2O) to the photocatalytic active site and thus increase the CO_2/H_2O ratio on the catalytic surface. Apparently, an excess of H_2O and a deficiency of CO_2 (that is a lower CO_2/H_2O ratio) is not effective for the formation of long chain hydrocarbons. For instance, Anpo and Chiba note that “in the case of high values for the H_2O/CO_2 ratio, the selectivity for the formation of CH_3OH became lower [246]. An insightful observation by Yamashita et al is that “the competitive co-adsorption of H_2O and CO_2” on the catalytic surface is crucial for photocatalytic reaction to occur [247]. Since a hydrophilic surface would be more prone to wetting by water, the CO_2/H_2O ratio would be unfavourably low, thus not allowing sufficient CO_2 molecules to be present on the catalytic sites for the formation of long chain hydrocarbons. However it is clear that a detailed first-principles reaction mechanism has not been derived for the photocatalytic CO_2 reduction process, without which it would be impossible to understand exactly why excessive water on the catalytic surface hinders the formation of long chain hydrocarbons.

To conclude, we end off with the remarks proffered by Ikeue et al [248], i.e. "the hydrophilic-hydrophobic properties were found to be the deciding factor controlling the reactivity and selectivity in the photocatalytic reduction of CO_2 with H_2O."

To investigate changes in surface hydrophobicity upon loading silver onto $NaNbO_3$, we performed contact angle measurements to understand the hydrophobic nature of both photocatalytic samples. From Fig. 5.5 and 5.6, we observe that the contact angle increases slightly after silver loading, corresponding to an increased surface hydrophobicity. The pure $NaNbO_3$ surface has almost perfect wettability with a negligible contact angle (Fig. 5.5). After silver loading, there is a small contact angle (Fig. 5.6) that was approximately 6.7°. Based on the aforementioned observation, this is one possible factor that accounts for the enhanced methanol selectivity.

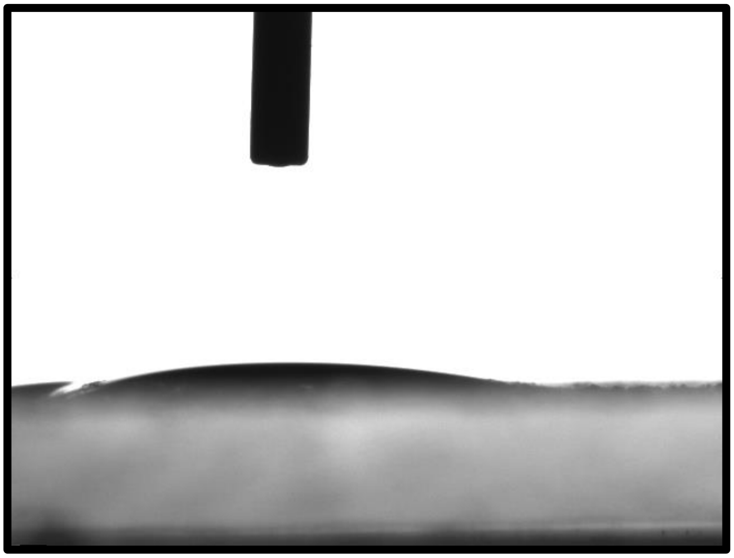

Fig. 5.5 Contact angle measurement of pure $NaNbO_3$

Fig. 5. 6 Contact angle measurement of Ag-loaded $NaNbO_3$

5.3.2.2 Enhanced electron density

Loading of metals like silver can extract photogenerated electrons and extend the electron lifetime to catalyse CO_2 reduction reactions. In addition, electron accumulation on metals allow the discharge of more than one electron at a time, facilitating the multi-electron CO_2 reduction processes [249]. This phenomenon of metal atom dopants causing electron trapping has been noted by several groups, for various metals. Tsai et al noted that metallic nickel (Ni) can trap electrons [250]; likewise, Ola et al also used Ni to enhance CO_2 reduction, and this improvement was ascribed to the electron-trapping property of nickel, leading to suppressed electron-hole recombination and effective charge separation [251]. Gupta and co-workers found a significant enhancement in the photocatalytic reduction of CO_2 by co-loading Ag–Pt bimetallic nanoparticles onto TiO_2. They proposed that Ag–Pt co-catalysts trapped electrons and accelerated the transfer of electrons to CO_2 for reduction [252]. Murakami photodeposited Ag and Au nanoparticles on TiO_2 and obtained increased methanol production, which they attribute to the metal dopants functioning as reductive sites for the multi-electron reduction of CO_2 to methanol [253]. From these reports, we infer that silver can play the role of an electron-trapping centre. The enhanced electron availability on silver is likely to facilitate multi-electron transfers more easily, which explains why methanol, which requires 6 electrons per molecule, is produced with greater selectively than formic acid, which needs only two electrons per molecule formed, as per the reduction equations 5.3 and 5.4 below.

$$\mathbf{CO_2 + 6H^+ + 6e^- \rightarrow CH_3OH + H_2O} \qquad (5.3)$$

$$\mathbf{CO_2 + 2H^+ + 2e^- \rightarrow HCOOH} \qquad (5.4)$$

Also, the photoluminescence (PL) spectroscopy results are relevant in this context. By minimizing the electron-hole recombination rate, electron availability is guaranteed to increase with a longer electron lifetime. Usually, the PL results are interpreted to mean an increase in yield of all products due to enhanced electron availability. Whilst this is certainly the usual explanation, we interpret things slightly unconventionally and observe that an increased electron density is also likely to selectively promote multi-electrons products. All these factors collectively increase the electron availability, encouraging multi-electron reactions preferentially, for reasons mentioned in the aforementioned paragraph. This explains why methanol would be selectively formed over formic acid upon silver loading.

5.3.2.3 Binding mode variations

There are three possible ways in which a CO_2 molecule binds to the photocatalyst surface. They are: carbon, oxygen and mixed coordination, as depicted in Fig. 5.7. Depending on which binding mode is favoured for a particular photocatalyst, the final product distribution will be affected accordingly. The first step in the photo-catalytic reduction of CO_2 is the adsorption and activation of CO_2 on the surface of a heterogeneous catalyst, to enable the transfer of electrons from the catalyst to the CO_2 molecule.

For the oxygen coordination mode shown in Fig. 5.7(a), the following reaction step is the preferential binding between the carbon atom in CO_2 and a hydrogen atom to form $HCOO^-$, which can subsequently combine with a proton to produce HCOOH (equations (5.5)–(5.7)).

$$\bullet\, COO^-_{ads} + H^+ \rightarrow HCOO^\bullet_{ads} \qquad (5.5)$$

$$HCOO^\bullet_{ads} + e^- \rightarrow HCOO^- \qquad (5.6)$$

$$HCOO^- + H^+ \rightarrow HCOOH \qquad (5.7)$$

The hydrogen atom can originate from a conduction-band electron reducing a free proton. The breaking of the C–O bond in the CO_2 molecule does not occur in this situation. The final product is formic acid, and methanol production is generally not favoured for the oxygen coordination mode [254].

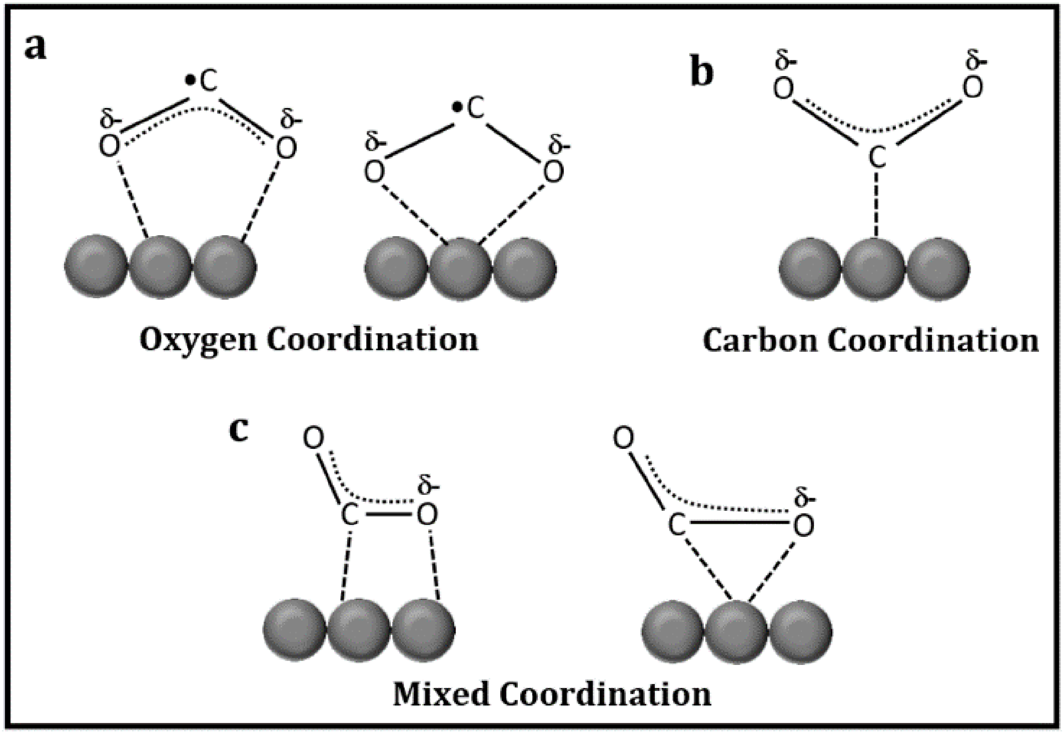

Fig. 5.7 CO_2 adsorption modes on catalyst surface.

In the case of carbon and carbon–oxygen adsorption modes, shown in Fig. 5.7(b) and 5.7(c) respectively, the process of hydrogenation is not typically favoured due to the attached carbon atom on the surface of the catalyst and as a result, one oxygen atom in CO_2• – combines with a hydrogen atom to form a carboxyl radical •COOH as depicted in equation (5.8). The •COOH thus formed could serve as a precursor for the formation of formic acid after combining with a hydrogen radical in the highly polar water medium. However there is a possibility of conversion of CO_2• – into carbon monoxide, when a hydrogen atom gets attached to the carbon atom resulting in the breaking of carbon–oxygen bond in CO_2• $^-$. The produced carbon monoxide is adsorbed on the surface of the catalyst as shown in equation (5.9) [255].

$$\bullet\, \mathrm{COO}^-_{\mathrm{ads}} + \mathrm{H}^+ \rightarrow \bullet\, \mathrm{COOH}_{\mathrm{ads}} \qquad (5.8)$$

$$\bullet\, \mathrm{COOH}_{\mathrm{ads}} + \mathrm{e}^- \rightarrow \mathrm{CO}_{\mathrm{ads}} + \mathrm{OH}^- \qquad (5.9)$$

Now comes the crucial part: if the CO-catalyst bond is weak, the carbon monoxide desorbs from the catalytic surface, and the final reaction product will be just carbon monoxide [256]. On the other hand, if the CO-catalyst bond is relatively strong, a carbon radical is formed by attracting additional electrons and subsequently combining with four H• radicals to form a series of products like carbene and/or a methyl radical, which eventually leads to the formation of methane [257]. During this chemical process, if the produced methyl radical combines with a hydroxyl radical instead of a hydrogen radical, the final product is a methanol molecule.

Since we obtain enhanced methanol production activity after silver loading, we hypothesize that there may be changes in binding modes (from oxygen coordination to either carbon or mixed coordination) owing to the deposited silver particles. The detailed mechanism for the selective formation of CH_3OH using $NaNbO_3$ photocatalyst is not well understood, and needs further research. Hence, our immediate future plan is to use DFT computation to study the binding modes of CO_2 molecule on the $NaNbO_3$ photocatalytic surface.

5.3.2.4 Summary

In retrospect, we hypothesize that the most likely cause is possibly the enhanced electron density. Silver being a metal with excellent conductivity naturally accumulates a large free electron density on its surface, thus playing the role of a charged trapping centre and facilitating the production of multi electron reduction products like methanol. This hypothesis can be tested by calculating the electron density of states (DOS) at the conduction band level for both the pure and Ag-loaded $NaNbO_3$, and checking if there is any enhancement in the DOS after silver loading. An increased DOS implies greater electron availability for effecting photocatalytic reduction of CO_2 to methanol, which would support the hypothesis proposed above.

5.3.3 Experimental parameters

In this section, we will explore the effect of various experimental parameters on the methanol production yield. They are: temperature, hole scavenger, basicity of medium and catalyst concentration. In any experiment, there is only one independent variable to be varied. Hence, the catalyst will be kept fixed as the Ag-loaded $NaNbO_3$, and each experimental run is for a fixed time interval of 4 hours. Of course, the lamp and all other variables must also be kept constant and only the parameter under study must be varied to ensure scientifically-rigorous results. Also, to simplify the analysis, we will focus only on one high value product, namely methanol. The methanol production yield has been normalised to unity (one i.e. 1) at its highest point, since we are simply trying to deduce the relative trends by varying the parameters, and these trends are more easily grasped using a normalised vertical scale, which makes for convenient reading. The following sections present the results pertaining to the experimental parameters' influence on the methanol yield.

5.3.3.1 Temperature

In this section, we investigate the effect of temperature on the methanol production yield. The temperature was varied by using a digital stirrer/heater, on which the reactor was placed. The temperature reading displayed by the stirrer is not an accurate indication of the true liquid temperature inside the reactor volume. Hence, before commencing temperature dependence studies, a calibration curve was prepared to relate the temperature readout on the stirrer/heater's LCD panel to the actual temperature inside the reactor. A high-sensitivity thermocouple thermometer was employed for this purpose and the calibration curve is shown in Fig. 5.8. From this, we observe that the actual temperature inside the reactor is always substantially lower than that shown on the stirrer/heater's display panel, since the stirrer/heater is exposed to the environment resulting in heat loss, and only a small fraction of the heat generated by the stirrer/heater actually goes towards heating the reactor volume. Hence, the actual temperature attained inside the reactor will always be less than that displayed by the stirrer heater.

As shown in Fig. 5.9, there is decreasing methanol production yield as the temperature increases from 20 to 50 °C. In Section 2.3.1, the effect of temperature on methanol yield has been thoroughly examined. To summarise, higher temperatures improve catalyst availability (by encouraging product desorption) and increase the reaction rate constant (by increasing the molecular collision frequency) but worsens the CO_2 solubility and the reactant adsorption (because thermal agitation may desorb reactants like CO_2). Based on our experience, the most significant factor is the decreased CO_2 solubility. As temperature rises less dissolved CO_2 remains in the water (see Table 5.1), and this was very clearly observed in the form of small bubbles effervescing out of the reaction medium. With less dissolved CO_2 there is less reactant concentration available leading to a decrease in the methanol yield.

Temperature (°C)	CO_2 solubility (g/L of water)
20	1.71
30	1.24
40	0.97
50	0.79

Table 5.1 Solubility of CO_2 in water as a function of temperature [258]

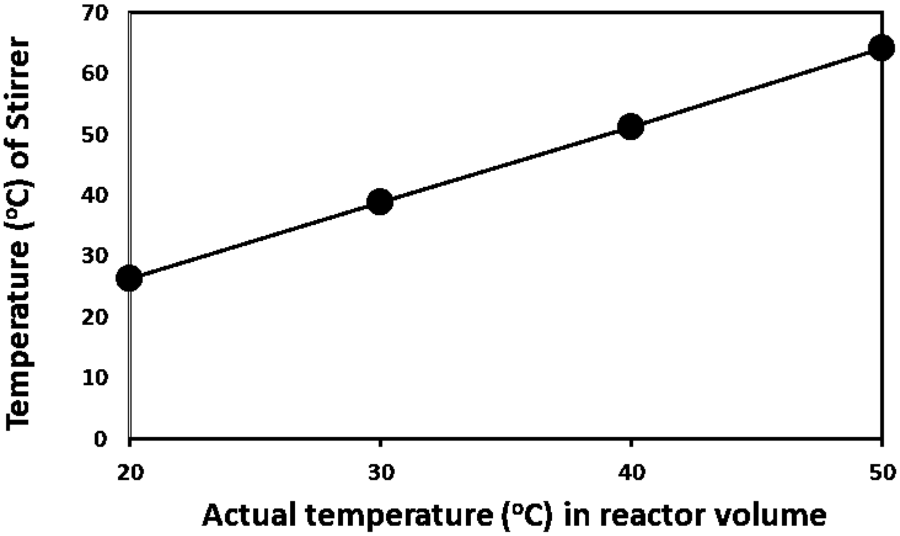

Fig. 5.8 Temperature calibration curve that relates actual reactor temperature to stirrer/heater display temperature

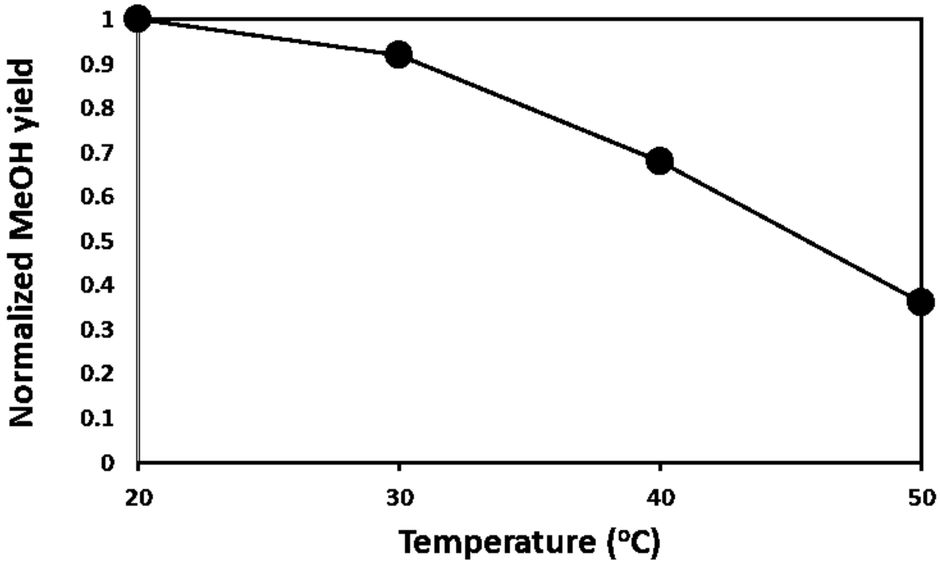

Fig. 5.9 Methanol yield as a function of temperature, using Ag-loaded $NaNbO_3$

5.3.3.2 Hole scavenger

The addition of hole scavengers is another experimental parameter that affects the methanol production yield. This was easily accomplished by adding fixed amounts of sodium sulphite (Na_2SO_3), which is a well-established hole scavenger, into the reaction medium before commencing irradiation. Four fixed concentrations (0.25, 0.5, 0.75 and 1.0 mol/dm^3) were chosen to study the effect of adding hole scavengers on the methanol production yield. As shown in Fig. 5.10, as the hole scavenger concentration increased, the methanol production yield also increased. The detailed mechanism has been elaborated in section 2.3. Since the methanol production process is electron-driven, reducing the hole concentration lowers the electron-hole recombination, leading to a higher electron density available for CO_2 reduction, resulting in an enhanced methanol production yield. To summarise, we note that hole scavengers consume free holes and thus enhance the electron density available for photocatalytic CO_2 reduction to methanol.

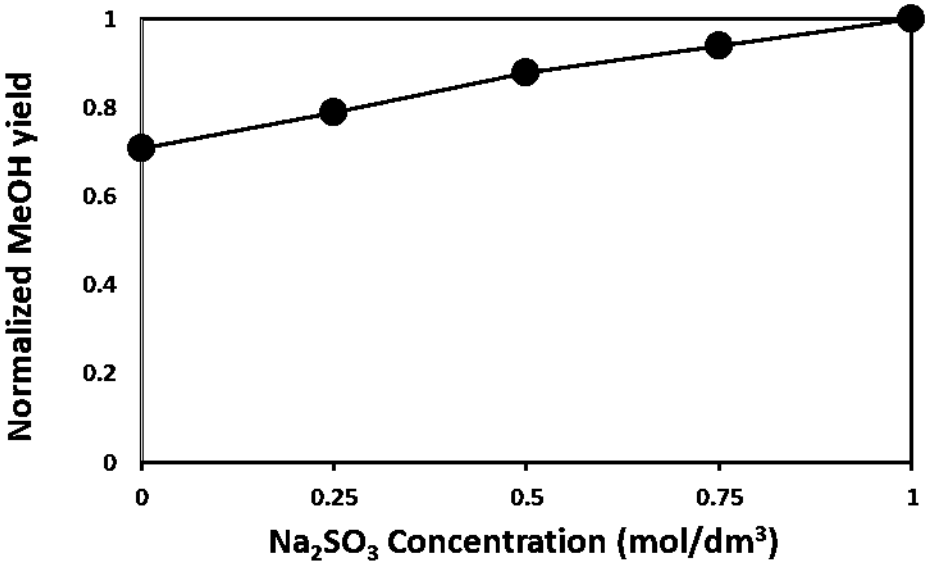

Fig. 5.10 Methanol yield as a function of hole scavenger concentration, using Ag-loaded $NaNbO_3$

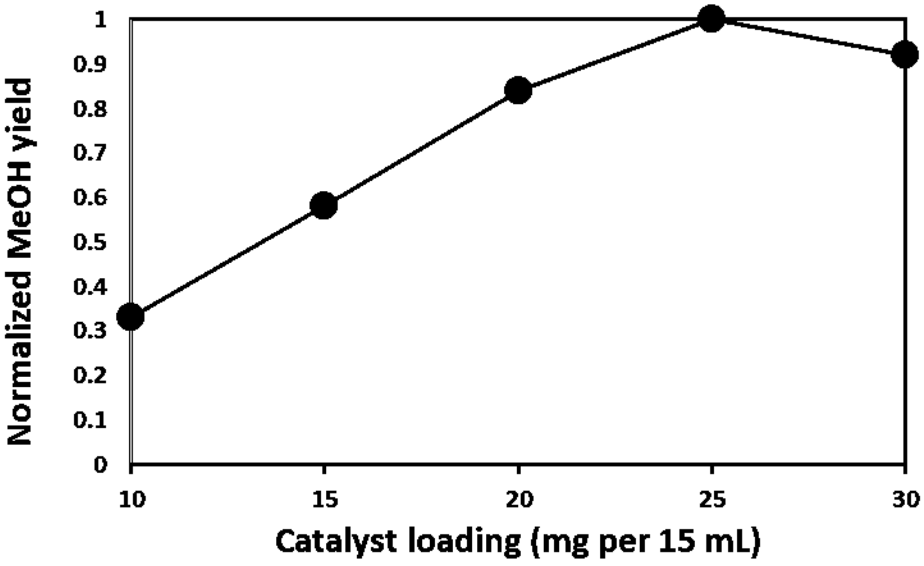

Fig. 5.11 Methanol yield as a function of catalyst concentration, using Ag-loaded $NaNbO_3$

5.3.3.3 Catalyst concentration

The catalyst loading (i.e. concentration) is another parameter that affects the methanol production yield. This parameter is again straightforward to control, by simply adding varying amounts of photocatalysts to achieve the desired concentration. Naturally, as the catalyst concentration increased, the methanol production yield also increased drastically (Fig. 5.11) due to the substantial increase in the availability of active catalytic sites. However, it is interesting to note that the increase is not continual, but rather peaks off at 25 mg of catalyst per 15 ml of solvent (Fig. 5.11). The reason has already been elaborated upon in section 2.3; basically, beyond a certain limiting concentration, there is excessive scattering and dispersion of the incident photons by the photocatalyst particles, which results in insufficient reactor volume illumination leading to reduced methanol yields.

5.3.3.4 Basic solvent medium

The basicity of the solvent medium which is experimentally controlled by adding sodium hydroxide (NaOH) is another experimental parameter that affects the methanol production yield,. The NaOH concentration is easily manipulated by dissolving NaOH pellets into the reactor medium prior to commencing illumination. We observe that increased NaOH concentrations result in enhanced methanol yields (Fig. 5.12), and this trend is consistently observed over the entire range of values tested (up to 1 mol/dm^3). In fact, it is possible that greater NaOH concentrations (> 1 mol/dm^3) may improve the yield even further. However, this option was not pursued to restrict the possibility of damage being caused to the sensitive chromatographic column owing to the strongly basic solution. Within the range of values tested (0 – 1 mol/dm^3), we observed a positive correlation which was accounted for in section 2.3. Increased basicity results in improved CO_2 solubility together with enhanced hole-scavenging capability offered by the hydroxide anions. These two factors collectively result in an enhanced methanol production yield with increasing NaOH concentration.

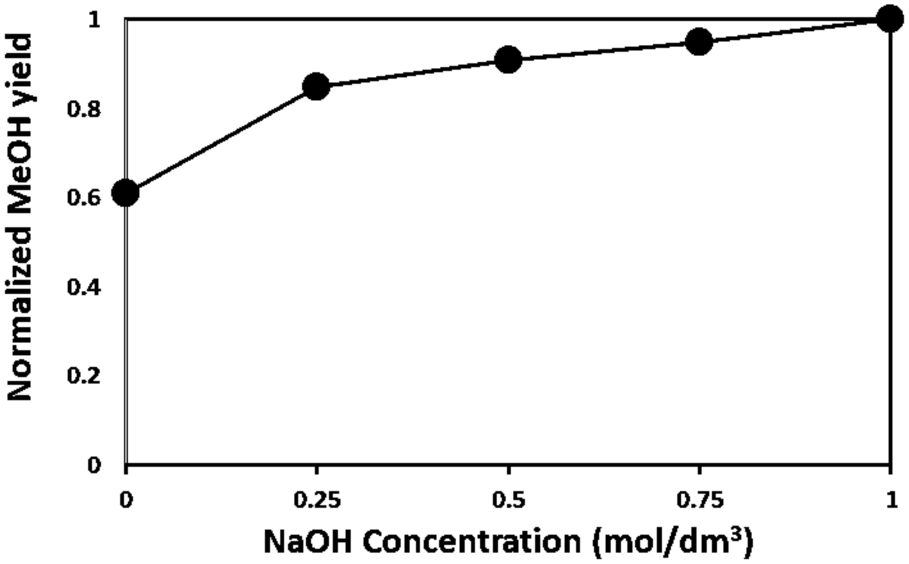

Fig. 5. 12 Methanol yield as a function of [NaOH] using Ag-loaded $NaNbO_3$

5.3.3.5 Overview of parameters

In this section, we have investigated a few experimental parameters that were technically feasible in our laboratory. It is clear from section 2.3 that there are several other interesting parameters that also affect the methanol production yield, but we have not been able to study these due to time and technical constraints. It would certainly be a priority to pursue some of these untested parameters, to study their effect on the methanol production yield, since the long-term goal of CO_2 photocatalytic reduction is to maximize methanol production. That would be our plan for future study.

CHAPTER 6

Conclusion

In this work, we have successfully synthesized a solar-harvesting semiconductor photocatalyst (g-C_3N_4) and a methanol-selective photocatalyst (Ag-loaded $NaNbO_3$). The performance of these photocatalyst was tested by the photocatalytic reduction of CO_2 to value-added hydrocarbon fuels, especially methanol.

Firstly, the as-synthesized photocatalysts were extensively characterized by XPS, XRD, UV-Vis, FT-IR, PL, Raman and FESEM to study their crystallographic, optical, electronic and morphological properties. These properties determine the level of photocatalytic performance, and dictate whether a particular photocatalyst will be suitable for a specific application. For instance, the optical band-gap energy data gives vital information pertaining to the spectral absorbance (whether visible or UV) of the photocatalyst, thus determining the suitability of a particular photocatalyst as a solar harvesting material.

Subsequently, both photocatalysts were tested for photocatalytic CO_2 reduction into fuels such as methanol. The first photocatalyst, graphitic carbon nitride – a visible-light sensitive photocatalyst, was tested under three distinct radiation sources: pulsed laser, UV broadband lamp and natural sunlight. It gave peak methanol yield of 510, 110 and 130 μmol g^{-1} respectively. Whilst the laser gives the highest yield of 510 μmol g^{-1} owing to its superior spectral and geometric characteristics, the most encouraging results are those obtained using natural sunlight (130 μmol g^{-1}) as it could potentially pave the way for a large-scale solar-driven CO_2-to-methanol system that would simultaneously absorb harmful atmospheric carbon dioxide and produce a relatively clean fuel (methanol) for meeting humanity's energy needs.

The second photocatalyst, a semiconductor metal oxide photocatalyst $NaNbO_3$, was loaded with silver particles which significantly improved the methanol product selectivity over formic acid. This agrees with the general understanding that metal dopants can alter the product distribution from CO_2 reduction. For this study, the following three reasons have been proposed to explain the aforementioned observation: increased surface hydrophobicity, enhanced surface electron density and change in binding modes.

However, there is still plenty of ambiguity with respect to the underlying reaction mechanism as well as the role of the metal atoms in enhancing methanol selectivity. We plan to study binding mode variation using advanced DFT computational techniques, because DFT codes are well suited for these types of analysis. It can calculate the most stable binding modes for the CO_2 molecule on any photocatalyst surface, thereby predicting the likely products to be obtained from CO_2 reduction. Also, we plan to conduct electrochemical impedance spectroscopy (EIS) to study if the impedance of the Ag-loaded photocatalyst is indeed lower than its pure counterpart. A lower impedance translates into higher conductance, which implies a larger surface electron density thus leading to the preferential formation of multi-electron reduction products such as methanol. These two issues constitute our plans for future research to continue this exciting journey that has enthralled us for the past 2 years.

References

1. Friedman A, Reverdin G, Khodri M, Gastineau G (2017) A new record of Atlantic sea surface salinity since 1896 reveals the influence of climate variability and global warming. EGU Gen Assem Conf Abstr 19:14989
2. Huang J, Yu H, Dai A, Wei Y, Kang L (2017) Drylands face potential threat under 2° C global warming target. Nat Clim Change 7:417-422
3. Malm A (2016) Fossil capital: The rise of steam power and the roots of global warming. Verso Books
4. Mills M, Mazur B, Frost T, Mullins D, Sinks C (2017) Global Warming: A Hot Topic.
5. IPCC (2007) Summary for Policymakers. In: Climate Change 2007: The Physical Science Basis. Contribution of Working Group I to the Fourth Assessment Report of the Intergovernmental Panel on Climate Change [Solomon, S., D. Qin, M. Manning, Z. Chen, M. Marquis, K.B. Averyt, M.Tignor and H.L. Miller (eds.)]. Cambridge University Press, Cambridge, United Kingdom and New York, NY, USA.
6. Raftery AE, Zimmer A, Frierson DM, Startz R, Liu P (2017) Less than 2 °C warming by 2100 unlikely. Nat Clim Change 7:nclimate3352
7. Ritz C, Pattyn F (2017) Impact of 1.5° C global warming on the Greenland and Antarctic ice sheets. EGU Gen Assem Conf Abstr 19:18601
8. Emanuel K (2017) Will Global Warming Make Hurricane Forecasting More Difficult? B Am Meteorol Soc 98:495-501
9. Smith IM, Thambimuthu KV (1993) Greenhouse gas emissions, abatement and control: the role of coal. Energ Fuel 7:7-13
10. IPCC (2014) Climate Change 2014: Synthesis Report. Contribution of Working Groups I, II and III to the Fifth Assessment Report of the Intergovernmental Panel on Climate Change [Core Writing Team, R.K. Pachauri and L.A. Meyer (eds.)]. IPCC, Geneva, Switzerland, 151 pp.
11. Jones N (2013) Troubling milestone for CO_2. Nat Geosci 6:589
12. USEPA, E. (2017). Inventory of US Greenhouse Gas Emissions and Sinks: 1990–2015. Washington, DC, USA, EPA.

13. Schöttl, P., Nitz, P., Fluri, T., & Steinfeld, A. (2016). Simulation and optimization of solar tower plant receivers. 12th SOLLAB Doctoral Colloqium, Rodalquilar, Almería, Spain, June 6-8, 2016: Book of Abstracts, 35-35.
14. Jemli, M. R., Naili, N., Farhat, A., & Guizani, A. (2017). Experimental investigation of solar tower with chimney effect installed in CRTEn, Tunisia. International Journal of Hydrogen Energy, 42(13), 8650-8660.
15. González-Roubaud, E., Pérez-Osorio, D., & Prieto, C. (2017). Review of commercial thermal energy storage in concentrated solar power plants: Steam vs. molten salts. Renewable and Sustainable Energy Reviews, 80, 133-148.
16. Islam, R., Bhuiyan, A. N., & Ullah, M. W. (2017, February). An overview of Concentrated Solar Power (CSP) technologies and its opportunities in Bangladesh. In Electrical, Computer and Communication Engineering (ECCE), International Conference on (pp. 844-849). IEEE.
17. Kumar, A., Prakash, O., & Dube, A. (2017). A review on progress of concentrated solar power in India. Renewable and Sustainable Energy Reviews, 79, 304-307.
18. Flesch, R., Frantz, C., Quinto, D. M., & Schwarzbözl, P. (2017). Towards an optimal aiming for molten salt power towers. Solar Energy, 155, 1273-1281.
19. González-Roubaud, E., Pérez-Osorio, D., & Prieto, C. (2017). Review of commercial thermal energy storage in concentrated solar power plants: Steam vs. molten salts. Renewable and Sustainable Energy Reviews, 80, 133-148.
20. Stein, W. H., & Buck, R. (2017). Advanced power cycles for concentrated solar power. Solar Energy, 152, 91-105.
21. Martín, F., Wiesenberg, R., & Santana, D. (2017, June). Solar thermal power & gas turbine hybrid design with molten salt storage tank. In AIP Conference Proceedings (Vol. 1850, No. 1, p. 160017). AIP Publishing.
22. Wang, K., He, Y. L., & Zhu, H. H. (2017). Integration between supercritical CO_2 Brayton cycles and molten salt solar power towers: A review and a comprehensive comparison of different cycle layouts. Applied Energy, 195, 819-836.
23. https://www.engineeringtoolbox.com/sensible-heat-storage-d_1217.html

24. Chen D, Zhang X, Lee AF (2015) Synthetic strategies to nanostructured photocatalysts for CO_2 reduction to solar fuels and chemicals. J Mater Chem A 3:14487-14516
25. Ganesh, I (2011) Conversion of carbon dioxide to methanol using solar energy-a brief review. Mater Sci Appl 2:1407.
26. Habisreutinger SN, Schmidt-Mende L, Stolarczyk J K (2013) Photocatalytic reduction of CO_2 on TiO_2 and other semiconductors. Angew Chem Int Edit 52:7372-7408
27. Izumi Y (2013) Recent advances in the photocatalytic conversion of carbon dioxide to fuels with water and/or hydrogen using solar energy and beyond. Coordin Chem Rev 257:171-186
28. Li K, An X, Park KH, Khraisheh M, Tang J (2014a) A critical review of CO_2 photoconversion: catalysts and reactors. Catal Today 224:3-12
29. Li X, Wen J, Low J, Fang Y, Yu J (2014b) Design and fabrication of semiconductor photocatalyst for photocatalytic reduction of CO_2 to solar fuel. Sci China Mater 57:70-100
30. Li K, Peng B, Peng T (2016) Recent advances in heterogeneous photocatalytic CO_2 conversion to solar fuels. ACS Catal. DOI: 10.1021/acscatal.6b02089
31. Liu X, Inagaki S, Gong J (2016) Heterogeneous molecular systems for photocatalytic CO_2 reduction with water oxidation. Angew Chem Int Edit
32. Nahar S, Zain MFM, Kadhum AAH, Hasan HA, Hasan MR (2017) Advances in Photocatalytic CO_2 Reduction with Water: A Review. Mater 10:629
33. Neațu Ș, Maciá-Agulló JA, Garcia H (2014) Solar light photocatalytic CO_2 reduction: general considerations and selected bench-mark photocatalysts. Int J Mol Sci 15:5246-5262
34. Nikokavoura A, Trapalis C (2017) Alternative photocatalysts to TiO_2 for the photocatalytic reduction of CO_2. Appl Surf Sci 391:149-174
35. Tu W, Zhou Y, Zou Z (2014) Photocatalytic Conversion of CO_2 into Renewable Hydrocarbon Fuels: State-of-the-Art Accomplishment, Challenges, and Prospects. Adv Mater 26: 4607-4626
36. Wang WN, Soulis J, Yang YJ, Biswas P (2014b) Comparison of CO_2 photoreduction systems: a review. Aerosol Air Qual Res 14:533-549

37. Su TM, Qin, ZZ, Ji HB, Jiang YX, Huang G (2016) Recent advances in the photocatalytic reduction of carbon dioxide. Environ Chem Lett 14:99-112
38. Tahir M, Amin NS (2013) Advances in visible light responsive titanium oxide-based photocatalysts for CO_2 conversion to hydrocarbon fuels. Energ Convers Manage 76:194-214
39. Yuan L, Xu YJ (2015) Photocatalytic conversion of CO_2 into value-added and renewable fuels. Appl Surf Sci 342:154-167
40. Cheng, W. H. (Ed.). (1994). Methanol production and use. CRC Press.
41. http://www.southernchemical.com/wp/products/methanol/principle-uses
42. http://www.methanol.org/chemical/
43. Samimi, F., & Rahimpour, M. R. (2017). Direct Methanol Fuel Cell. In Methanol (pp. 381-397).
44. Masdar, M. S., Zainoodin, A. M., Rosli, M. I., Kamarudin, S. K., & Daud, W. R. W. (2017). Performance and stability of single and 6-cell stack passive direct methanol fuel cell (DMFC) for long-term operation. International Journal of Hydrogen Energy, 42(14), 9230-9242.
45. Kim, S., Park, J. E., Hwang, W., Cho, Y. H., & Sung, Y. E. (2017). A hierarchical cathode catalyst layer architecture for improving the performance of direct methanol fuel cell. Applied Catalysis B: Environmental, 209, 91-97.
46. Ong, B. C., Kamarudin, S. K., Masdar, M. S., & Hasran, U. A. (2017). Applications of graphene nano-sheets as anode diffusion layers in passive direct methanol fuel cells (DMFC). International Journal of Hydrogen Energy, 42(14), 9252-9261.
47. Wan, N. (2017). High performance direct methanol fuel cell with thin electrolyte membrane. Journal of Power Sources, 354, 167-171.
48. Kireeti, K. V., & Jha, N. (2017). Surface tailored single walled carbon nanotubes as catalyst support for direct methanol fuel cell. Journal of Power Sources, 364, 392-399.
49. Gang, M., He, G., Li, Z., Cao, K., Li, Z., Yin, Y., ... & Jiang, Z. (2016). Graphitic carbon nitride nanosheets/sulfonated poly (ether ether ketone) nanocomposite membrane for direct methanol fuel cell application. Journal of Membrane Science, 507, 1-11.

50. Yola, M. L., Eren, T., Atar, N., Saral, H., & Ermiş, İ. (2016). Direct-methanol Fuel Cell Based on Functionalized Graphene Oxide with Mono-metallic and Bi-metallic Nanoparticles: Electrochemical Performances of Nanomaterials for Methanol Oxidation. Electroanalysis, 28(3), 570-579.
51. Chen, X., Li, T., Shen, J., & Hu, Z. (2017). From structures, packaging to application: A system-level review for micro direct methanol fuel cell. Renewable and Sustainable Energy Reviews, 80, 669-678.
52. Mallick, R. K., Thombre, S. B., & Shrivastava, N. K. (2016). Vapor feed direct methanol fuel cells (DMFCs): a review. Renewable and Sustainable Energy Reviews, 56, 51-74.
53. Munjewar, S. S., Thombre, S. B., & Mallick, R. K. (2017). A comprehensive review on recent material development of passive direct methanol fuel cell. Ionics, 1-18.
54. Nichols, R. J. (2003). The methanol story: a sustainable fuel for the future.
55. Liang, B., Ge, Y., Tan, J., Han, X., Gao, L., Hao, L., ... & Dai, P. (2013). Comparison of PM emissions from a gasoline direct injected (GDI) vehicle and a port fuel injected (PFI) vehicle measured by electrical low pressure impactor (ELPI) with two fuels: Gasoline and M15 methanol gasoline. Journal of Aerosol Science, 57, 22-31.
56. Zhen, X., & Wang, Y. (2015). An overview of methanol as an internal combustion engine fuel. Renewable and Sustainable Energy Reviews, 52, 477-493.
57. Liu, H., Wang, Z., & Wang, J. (2014). Methanol-gasoline DFSI (dual-fuel spark ignition) combustion with dual-injection for engine knock suppression. Energy, 73, 686-693.
58. Wang, X., Ge, Y., Liu, L., Peng, Z., Hao, L., Yin, H., ... & Wang, J. (2015). Evaluation on toxic reduction and fuel economy of a gasoline direct injection-(GDI-) powered passenger car fueled with methanol–gasoline blends with various substitution ratios. Applied Energy, 157, 134-143.
59. Alberico, E., & Nielsen, M. (2015). Towards a methanol economy based on homogeneous catalysis: methanol to H_2 and CO_2 to methanol. Chemical Communications, 51(31), 6714-6725.
60. Goeppert, A., Olah, G. A., & Prakash, G. S. (2017). Toward a Sustainable Carbon Cycle: The Methanol Economy. In Green Chemistry (pp. 919-962).

61. Stephan, D. W. (2013). Catalysis: a step closer to a methanol economy. Nature, 495(7439), 54-55.

62. Quintero JCC, Xu YJ (Eds.). (2015). Heterogeneous Photocatalysis: From Fundamentals to Green Applications. Springer

63. Gondal MA, Ali MA, Chang XF, Shen K, Xu QY, Yamani ZH (2012) Pulsed laser-induced photocatalytic reduction of greenhouse gas CO_2 into methanol: A value-added hydrocarbon product over SiC. J Environ Sci Heal A, Part A 47:1571-1576.

64. An C, Wang J, Jiang W, Zhang M, Ming X, Wang S, Zhang Q (2012) Strongly visible-light responsive plasmonic shaped AgX: Ag (X= Cl, Br) nanoparticles for reduction of CO_2 to methanol. Nanoscale 4:5646-5650

65. Chen D, Yoo SH, Huang Q, Ali G, Cho SO (2012) Sonochemical Synthesis of Ag/AgCl Nanocubes and Their Efficient Visible-Light-Driven Photocatalytic Performance. Chem-Eur J 18:5192-5200

66. Jiang J, Zhang L (2011) Rapid Microwave-Assisted Nonaqueous Synthesis and Growth Mechanism of AgCl/Ag, and Its Daylight-Driven Plasmonic Photocatalysis. Chem-Eur J 17:3710-3717

67. Chang X, Zheng J, Gondal MA, Ji G (2015) Photocatalytic conversion of CO_2 into value-added hydrocarbon (methanol) with high selectivity over ZnS nanoparticles driven by 355-nm pulsed laser. Res Chem Intermediat 41:739-747

68. Kočí K, Reli M, Kozák O, Lacný Z, Plachá D, Praus P, Obalová L (2011) Influence of reactor geometry on the yield of CO_2 photocatalytic reduction. Catal Today 176:212-214

69. Li X, Chen J, Li H, Li J, Xu Y, Liu Y, Zhou J (2011) Photoreduction of CO_2 to methanol over Bi_2S_3/CdS photocatalyst under visible light irradiation. J Nat Gas Chem 20:413-417

70. Li X, Liu H, Luo D, Li J, Huang Y, Li H, Fang Y, Xu Y, Zhu L (2012) Adsorption of CO_2 on heterostructure CdS(Bi_2S_3)/TiO_2 nanotube photocatalysts and their photocatalytic activities in the reduction of CO_2 to methanol under visible light irradiation. Chem Eng J 180:151-158

71. Prasad DMR, Rahmat NSB, Ong HR, Cheng CK, Khan MR, Sathiyamoorthy D (2016) Preparation and Characterization of Photocatalyst for the Conversion of Carbon

Dioxide to Methanol. World Academy of Science, Engineering and Technology, Int J Chem Mol Nucl Mater Metall Eng 10:552-555

72. Reli M, Šihor M, Kočí K, Praus P, Kozák O, Obalová L (2012) Influence of Reaction Medium on CO_2 Photocatalytic Reduction Yields Over Zns-MMT. GeoScience Eng 58:34-42
73. Kočí K, Matějů K, Obalová L, Krejčíková S, Lacný Z, Plachá D, Čapek L, Hospodková A, Šolcová O (2010) Effect of silver doping on the TiO_2 for photocatalytic reduction of CO_2. Appl Catal B-Environ 96:239-244
74. Liu E, Hu Y, Li H, Tang C, Hu X, Fan J, Chen Y, Bian, J (2015) Photoconversion of CO_2 to methanol over plasmonic Ag/TiO_2 nano-wire films enhanced by overlapped visible-light-harvesting nanostructures. Ceram Int 41:1049-1057
75. Liu E, Qi L, Bian J, Chen Y, Hu X, Fan J, Liu H, Zhu C Wang, Q (2015) A facile strategy to fabricate plasmonic Cu modified TiO_2 nano-flower films for photocatalytic reduction of CO_2 to methanol. Mater Res Bull 68:203-209 Luo et al. 2011;
76. Wang J, Ji G, Liu Y, Gondal MA, Chang X (2014) Cu_2O/TiO_2 heterostructure nanotube arrays prepared by an electrodeposition method exhibiting enhanced photocatalytic activity for CO_2 reduction to methanol. Catal Commun 46:17-21
77. Xiong Z, Zhao Y, Zhang J, Zheng C (2015) Efficient photocatalytic reduction of CO_2 into liquid products over cerium doped titania nanoparticles synthesized by a sol–gel auto-ignited method. Fuel Processing Technology, 135, 6-13.
78. Yahaya AH, Gondal MA, Hameed A (2004) Selective laser enhanced photocatalytic conversion of CO_2 into methanol. Chem Phys Lett 400:206-212
79. Yu B, Zhou Y, Li P, Tu W, Li P, Tang L, Ye J, Zou Z (2016) Photocatalytic reduction of CO_2 over Ag/TiO_2 nanocomposites prepared with a simple and rapid silver mirror method. Nanoscale 8:11870-11874
80. Adekoya DO, Tahir M, Amin NAS (2015) Copper modified TiO_2 and g-C_3N_4 catalysts for photoreduction of CO_2 to methanol using different reaction mediums. Mal J Fund Appl Sci 11
81. Adekoya DO, Tahir M, Amin NAS (2017) gC_3N_4/(Cu/TiO_2) nanocomposite for enhanced photoreduction of CO_2 to CH_3OH and HCOOH under UV/visible light. J of CO_2 Utilization 18:261-274.

82. Gondal MA, Lais A, Dastageer MA, Yang D, Shen K, Chang X (2017) Photocatalytic conversion of CO_2 into methanol using graphitic carbon nitride under solar, UV laser and broadband radiations. Int J Energy Res. DOI: 10.1002/er.3777
83. He Y, Wang Y, Zhang L, Teng B, Fan M (2015) High-efficiency conversion of CO_2 to fuel over ZnO/gC_3N_4 photocatalyst. Appl Catal B-Environ 168:1-8
84. Mao J, Peng T, Zhang X, Li K, Ye L, Zan L (2013) Effect of graphitic carbon nitride microstructures on the activity and selectivity of photocatalytic CO_2 reduction under visible light. Catal Sci Technol 3: 1253-1260
85. Ohno T, Murakami N, Koyanagi T, Yang Y (2014) Photocatalytic reduction of CO_2 over a hybrid photocatalyst composed of WO_3 and graphitic carbon nitride (gC_3N_4) under visible light. J CO_2 Util 6:17-25
86. Wang K, Li Q, Liu B, Cheng B, Ho W, Yu J (2015) Sulfur-doped gC_3N_4 with enhanced photocatalytic CO_2-reduction performance. Appl Catal B-Environ 176:44-52
87. Ye S, Wang R, Wu MZ, Yuan YP (2015) A review on gC_3N_4 for photocatalytic water splitting and CO_2 reduction. Appl Surf Sci358:15-27
88. Yu J, Wang K, Xiao W, Cheng B (2014) Photocatalytic reduction of CO_2 into hydrocarbon solar fuels over gC_3N_4–Pt nanocomposite photocatalysts. Phys Chem Chem Phys 16:11492-11501
89. Gusain R, Kumar P, Sharma OP, Jain SL, Khatri OP (2016) Reduced graphene oxide–CuO nanocomposites for photocatalytic conversion of CO_2 into methanol under visible light irradiation. Appl Catal B-Environ 181:352-362
90. Lv XJ, Fu WF, Hu CY, Chen Y, Zhou WB (2013) Photocatalytic reduction of CO_2 with H_2O over a graphene-modified NiO_x–Ta_2O_5 composite photocatalyst: coupling yields of methanol and hydrogen. RSC Adv 3:1753-1757
91. Zhang N, Zhang Y, Xu YJ (2012) Recent progress on graphene-based photocatalysts: current status and future perspectives. Nanoscale 4:5792-5813
92. Zhang L, Li N, Jiu H, Qi G, Huang Y (2015) ZnO-reduced graphene oxide nanocomposites as efficient photocatalysts for photocatalytic reduction of CO_2. Ceram Int 41:6256-6262

93. Hsu HC, Shown I, Wei HY, Chang YC, Du HY, Lin YG, Tseng CA, Wang CH, Chen LC, Lin YC, Chen KH (2013) Graphene oxide as a promising photocatalyst for CO_2 to methanol conversion. Nanoscale 5:262-268
94. Kumar P, Mungse HP, Cordier S, Boukherroub R, Khatri OP, Jain SL (2015) Hexamolybdenum clusters supported on graphene oxide: Visible-light induced photocatalytic reduction of carbon dioxide into methanol. Carbon 94:91-100
95. Shown I, Hsu HC, Chang YC, Lin CH, Roy PK, Ganguly A, Wang CH, Chang JK, Wu CI, Chen LC, Chen KH (2014) Highly efficient visible light photocatalytic reduction of CO_2 to hydrocarbon fuels by Cu-nanoparticle decorated graphene oxide. Nano Lett 14:6097-6103
96. Centi G, Perathoner S (2010) Problems and perspectives in nanostructured carbon-based electrodes for clean and sustainable energy. Catal Today 150:151-162
97. Malik MI, Malaibari ZO, Atieh M, Abussaud B (2016) Electrochemical reduction of CO_2 to methanol over MWCNTs impregnated with Cu_2O. Chem Eng Sci 152:468-477
98. Saleh TA (2013) The role of carbon nanotubes in enhancement of photocatalysis. In Syntheses and Applications of Carbon Nanotubes and Their Composites. InTech 21:479-493
99. Li H, Zhang X, MacFarlane, DR (2015) Carbon Quantum Dots/Cu2O Heterostructures for Solar-Light-Driven Conversion of CO_2 to Methanol. Adv Energy Mater 5
100. Bhattacharya AK, Mallick KK, Hartridge A (1997) Phase transition in $BiVO_4$. Mater Lett 30:7-13
101. Lim AR, Choh SH, Jang MS (1992) Nuclear magnetic resonance of ^{209}Bi in a $BiVO_4$ single crystal. J Phys-Condens Mat 4:1607
102. Lim AR, Choh SH, Jang MS (1995) Prominent ferroelastic domain walls in $BiVO_4$ crystal. J Phys-Condens Mat 7:7309
103. Kudo A, Omori K, Kato H (1999) A novel aqueous process for preparation of crystal form-controlled and highly crystalline $BiVO_4$ powder from layered vanadates at room temperature and its photocatalytic and photophysical properties. J Am Chem Soc 121:11459-11467

104. Tokunaga S, Kato H, Kudo A (2001) Selective preparation of monoclinic and tetragonal $BiVO_4$ with scheelite structure and their photocatalytic properties. Chem Mater 13: 4624-4628

105. Yu J, Kudo A (2005) Hydrothermal synthesis of nanofibrous bismuth vanadate. Chem Lett 34:850-851

106. Zhang L, Chen D, Jiao X (2006) Monoclinic structured $BiVO_4$ nanosheets: hydrothermal preparation, formation mechanism, and coloristic and photocatalytic properties. J Phys Chem B 110: 2668-2673

107. Zhou L, Wang W, Zhang L, Xu H, Zhu W (2007) Single-crystalline $BiVO_4$ microtubes with square cross-sections: microstructure, growth mechanism, and photocatalytic property. J Phys Chem C 111:13659-13664

108. Mao J, Peng T, Zhang X, Li K, Zan L (2012) Selective methanol production from photocatalytic reduction of CO_2 on $BiVO_4$ under visible light irradiation. Catal Commun 28:38-41

109. Liu Y, Huang B, Dai Y, Zhang X, Qin X, Jiang M, Whangbo M H (2009) Selective ethanol formation from photocatalytic reduction of carbon dioxide in water with $BiVO_4$ photocatalyst. Catal Commun 11:210-213

110. Liang L, Lei F, Gao S, Sun Y, Jiao X, Wu J, Qamar S, Xie Y (2015) Single unit cell bismuth tungstate layers realizing robust solar CO_2 reduction to methanol. Angew Chem Int Edit 54:13971-13974

111. Sun Z, Yang Z, Liu H, Wang H, Wu Z (2014) Visible-light CO_2 photocatalytic reduction performance of ball-flower-like Bi2WO6 synthesized without organic precursor: Effect of post-calcination and water vapor. Appl Surf Sci 315:360-367

112. Zhou Y, Tian Z, Zhao Z, Liu Q, Kou J, Chen, X, Gao J, Yan S, Zou Z (2011) High-yield synthesis of ultrathin and uniform Bi2WO6 square nanoplates benefitting from photocatalytic reduction of CO_2 into renewable hydrocarbon fuel under visible light. ACS Appl Mater Interfaces 3:3594–3601

113. Cheng H, Huang B, Liu Y, Wang Z, Qin X, Zhang X, Dai Y (2012) An anion exchange approach to Bi2WO6 hollow microspheres with efficient visible light photocatalytic reduction of CO_2 to methanol. Chem Commun 48:9729-9731

114. Dai W, Xu H, Yu J, Hu X, Luo X, Tu X, Yang L (2015) Photocatalytic reduction of CO_2 into methanol and ethanol over conducting polymers modified Bi2WO6 microspheres under visible light. Appl Surf Sci 356:173-180

115. Xiao X, Wei J, Yang Y, Xiong R, Pan C, Shi J (2016) Photoreactivity and mechanism of g-C_3N_4 and Ag co-modified Bi2WO6 microsphere under visible light irradiation. ACS Sustain Chem Eng 4:3017-3023

116. Dandia A, Jain AK, Sharma S (2013) $CuFe_2O_4$ nanoparticles as a highly efficient and magnetically recoverable catalyst for the synthesis of medicinally privileged spiropyrimidine scaffolds. RSC Adv 3:2924-2934

117. Wu R, Qu J, He H, Yu Y (2004) Removal of azo-dye Acid Red B (ARB) by adsorption and catalytic combustion using magnetic $CuFe_2O_4$ powder. Appl Catal B-Environ 48:49-56

118. Yang H, Yan J, Lu Z, Cheng X, Tang Y (2009) Photocatalytic activity evaluation of tetragonal $CuFe_2O_4$ nanoparticles for the H_2 evolution under visible light irradiation. J Alloy Compd 476:715-719

119. Tao S, Gao F, Liu X, Sørensen OT (2000) Preparation and gas-sensing properties of $CuFe_2O_4$ at reduced temperature. Mater Sci Eng B-Adv 77:172-176

120. Sun Z, Liu L, Zeng JD, Pan W (2007) Simple synthesis of $CuFe_2O_4$ nanoparticles as gas-sensing materials. Sensor Actuat B-Chem 125:144-148

121. Uddin MR, Khan MR, Rahman MW, Yousuf A, Cheng CK (2015) Photocatalytic reduction of CO_2 into methanol over $CuFe_2O_4/TiO_2$ under visible light irradiation. React Kinet Mech Cat 116:589-604

122. Kim KJ, Lee JH, Lee SH (2004) Magneto-optical investigation of spinel ferrite $CuFe_2O_4$: observation of Jahn–Teller effect in Cu^{2+} ion. J Magn Magn Mater 279:173-177

123. Teraoka Y, Kagawa S (1998) Simultaneous catalytic removal of NO_x and diesel soot particulates. Catal Surv Asia 2:155-164

124. Yang H, Yan J, Lu Z, Cheng X, Tang Y (2009) Photocatalytic activity evaluation of tetragonal $CuFe_2O_4$ nanoparticles for the H_2 evolution under visible light irradiation. J Alloy Compd 476:715-719

125. Nabiyouni G, Ghanbari DA, Yousofnejad AS, Seraj MI, Mirdamadian, ZA (2013). Microwave-Assisted Synthesis of CuFe2O4 Nanoparticles and Starch-Based Magnetic Nanocomposites. J Nanostructures, 3(2), 155-160.

126. Liu Q, Chai Y, Zhang L, Ren J, Dai WL (2017) Highly efficient Pt/$NaNbO_3$ nanowire photocatalyst: Its morphology effect and application in water purification and H2 production. Appl Catal B-Environ 205:505-513

127. Shi H, Chen G, Zhang C, Zou Z (2014) Polymeric g-C_3N_4 coupled with $NaNbO_3$ nanowires toward enhanced photocatalytic reduction of CO_2 into renewable fuel. ACS Catal 4:3637-3643

128. Kumar S, Khanchandani S, Thirumal M, Ganguli AK (2014) Achieving enhanced visible-light-driven photocatalysis using type-II $NaNbO_3$/CdS core/shell heterostructures. ACS Appl Mater Inter 6:13221-13233

129. Shi H, Li X, Iwai H, Zou Z, Ye J (2009) 2-Propanol photodegradation over nitrogen-doped $NaNbO_3$ powders under visible-light irradiation. J Phys Chem Solids 70:931-935

130. Baeissa ES (2016) Photocatalytic degradation of malachite green dye using Au/$NaNbO_3$ nanoparticles. J Alloy Compd 672:564-570

131. Xu J, Zhang F, Sun B, Du Y, Li G, Zhang W (2015) Enhanced photocatalytic property of Cu doped sodium niobate. Int J Photoenergy. DOI: 10.1155/2015/846121

132. Zielińska B, Borowiak-Palen E, Kalenczuk RJ (2011) Preparation, characterization and photocatalytic activity of metal-loaded $NaNbO_3$. J Phys Chem Solids 72:117-123

133. Li P, Ouyang S, Xi G, Kako T, Ye J (2012a) The effects of crystal structure and electronic structure on photocatalytic H2 evolution and CO_2 reduction over two phases of perovskite-structured $NaNbO_3$. J Phys Chem C 116:7621-7628

134. Fresno F, Jana P, Reñones P, Coronado JM, Serrano DP, de la Peña O'Shea VA (2017) CO_2 reduction over $NaNbO_3$ and $NaTaO_3$ perovskite photocatalysts. Photoch Photobio Sci 16:17-23

135. Lichtfouse, E., Schwarzbauer, J. and Robert, D. eds. CO_2 sequestration, biofuels and depollution (Vol. 5). Springer 2015, pp.94-95

136. Anpo, M., Yamashita, H., Ichihashi, Y. and Ehara, S. Photocatalytic reduction of CO_2 with H_2O on various titanium oxide catalysts. Journal of Electroanalytical Chemistry 1995; 396(1-2), pp.21-26.

137. Nasution, H.W., Purnama, E., Kosela, S. and Gunlazuardi, J. Photocatalytic reduction of CO_2 on copper-doped Titania catalysts prepared by improved-impregnation method. Catalysis Communications 2005; 6(5), pp.313-319.

138. Kočí, K., Obalová, L., Plachá, D. and Lacný, Z. Effect of temperature, pressure and volume of reacting phase on photocatalytic CO_2 reduction on suspended nanocrystalline TiO_2. Collection of czechoslovak chemical communications 2008; 73(8), pp.1192-1204.

139. Herrmann, J.M. Heterogeneous photocatalysis: fundamentals and applications to the removal of various types of aqueous pollutants. Catalysis today 1999; 53(1), pp.115-129.

140. Yamashita, H., Shiga, A., Kawasaki, S.I., Ichihashi, Y., Ehara, S. and Anpo, M. Photocatalytic synthesis of CH_4 and CH_3OH from CO_2 and H_2O on highly dispersed active titanium oxide catalysts. Energy conversion and management 1995; 36(6), pp.617-620.

141. Tahir, M. and Amin, N.S. Recycling of carbon dioxide to renewable fuels by photocatalysis: Prospects and challenges. Renewable and Sustainable Energy Reviews 2013; 25, pp.560-579.

142. Neațu, Ș., Maciá-Agulló, J.A. and Garcia, H. Solar light photocatalytic CO_2 reduction: general considerations and selected bench-mark photocatalysts. International journal of molecular sciences 2014; 15(4), pp.5246-5262.

143. Tahir, M. and Amin, N.S. Advances in visible light responsive titanium oxide-based photocatalysts for CO_2 conversion to hydrocarbon fuels. Energy conversion and management 2013; 76, pp.194-214.

144. Gonell, F., Puga, A.V., Julián-López, B., García, H. and Corma, A. Copper-doped titania photocatalysts for simultaneous reduction of CO_2 and production of H_2 from aqueous sulfide. Applied Catalysis B: Environmental 2016; 180, pp.263-270.

145. Tseng, I.H., Chang, W.C. and Wu, J.C. Photoreduction of CO_2 using sol–gel derived titania and titania-supported copper catalysts. Applied Catalysis B: Environmental 2002; 37(1), pp.37-48.
146. Yan, X., Bao, R., Yu, S., Li, Q. and Jing, Q. The roles of hydroxyl radicals, photo-generated holes and oxygen in the photocatalytic degradation of humic acid. Russian Journal of Physical Chemistry A, Focus on Chemistry 2012; 86(9), pp.1479-1485.
147. Marszewski, M., Cao, S., Yu, J. and Jaroniec, M. Semiconductor-based photocatalytic CO_2 conversion. Materials Horizons 2015; 2(3), pp.261-278.
148. Matthews, R.W. and McEvoy, S.R. A comparison of 254 nm and 350 nm excitation of TiO_2 in simple photocatalytic reactors. Journal of Photochemistry and Photobiology A: Chemistry 1992; 66(3), pp.355-366.
149. Kočí, K., Zatloukalová, K., Obalová, L., Krejčíková, S., Lacný, Z., Čapek, L., Hospodková, A. and Šolcová, O. Wavelength effect on photocatalytic reduction of CO_2 by Ag/TiO_2 catalyst. Chinese Journal of Catalysis 2011; 32(5), pp.812-815.
150. Lingampalli, S.R., Ayyub, M.M. and Rao, C.N.R. Recent Progress in the Photocatalytic Reduction of Carbon Dioxide. ACS Omega, 2017; 2(6), pp.2740-2748.
151. Kamat, P.V. Photochemistry on nonreactive and reactive (semiconductor) surfaces. Chemical Reviews 1993; 93(1), pp.267-300.
152. Dey, G.R. Transformation of Carbon Dioxide to Useable Products through Free Radical-Induced Reactions. Green Carbon Dioxide: Advances in CO Utilization 2014, pp.25-50.
153. Li, H., Li, C., Han, L., Li, C. and Zhang, S. Photocatalytic reduction of CO_2 with H_2O on CuO/TiO_2 catalysts. Energy Sources, Part A: Recovery, Utilization, and Environmental Effects 2016; 38(3), pp.420-426.
154. Wu, J.C., 2010. Renewable Energy from the Photocatalytic Reduction of CO_2 with H_2O. In Environmentally Benign Photocatalysts (pp. 673-696). Springer New York.
155. Kiesgen de_Richter, R., Ming, T. and Caillol, S. Fighting global warming by photocatalytic reduction of CO_2 using giant photocatalytic reactors. Renewable and Sustainable Energy Reviews 2013; 19, pp.82-106.

156. Liu, S., Zhao, Z. and Wang, Z. Photocatalytic reduction of carbon dioxide using sol–gel derived titania-supported CoPc catalysts. Photochemical & Photobiological Sciences 2007; 6(6), pp.695-700.

157. Braham, R.J. and Harris, A.T. Review of major design and scale-up considerations for solar photocatalytic reactors. Industrial & Engineering Chemistry Research 2009; 48(19), pp.8890-8905.

158. Wirth, J., Neumann, R., Antonietti, M., & Saalfrank, P. (2014). Adsorption and photocatalytic splitting of water on graphitic carbon nitride: a combined first principles and semiempirical study. Physical Chemistry Chemical Physics, 16(30), 15917-15926.

159. Fresno, F., Jana, P., Reñones, P., Coronado, J. M., Serrano, D. P., & de la Peña O'Shea, V. A. (2017). CO 2 reduction over $NaNbO_3$ and $NaTaO_3$ perovskite photocatalysts. Photochemical & Photobiological Sciences, 16(1), 17-23.

160. Yan, S. C., Li, Z. S., & Zou, Z. G. (2009). Photodegradation performance of g-C_3N_4 fabricated by directly heating melamine. Langmuir, 25(17), 10397-10401.

161. Eckert, M. (2012). Max von Laue and the discovery of X-ray diffraction in 1912. Annalen der Physik, 524(5).

162. Moore, D. M., & Reynolds, R. C. (1989). X-ray Diffraction and the Identification and Analysis of Clay Minerals (Vol. 378, p. 155). Oxford: Oxford university press.

163. Waseda, Y., Matsubara, E., & Shinoda, K. (2011). X-ray diffraction crystallography: introduction, examples and solved problems. Springer Science & Business Media.

164. Reichelt, R. (2007). Scanning electron microscopy. In Science of microscopy (pp. 133-272). Springer, New York, NY.

165. http://photometrics.net/field-emission-scanning-electron-microscopy-fesem/

166. Brodusch, N., Demers, H., & Gauvin, R. (2017). Field Emission Scanning Electron Microscopy: New Perspectives for Materials Characterization. Springer.

167. Goodhew, P. J., Humphreys, J., & Beanland, R. (2000). Electron microscopy and analysis. CRC Press.

168. Watts, J. F., & Wolstenholme, J. (2003). An introduction to surface analysis by XPS and AES.

169. Brigg, D., & Seah, M. P. (1995). Practical Surface Analysis: Auger and X-Ray Photoelectron Spectroscopy, vol. 1.

170. Van der Heide, P. (2011). X-ray photoelectron spectroscopy: an introduction to principles and practices. John Wiley & Sons.

171. Hofmann, S. (2012). Auger-and X-ray photoelectron spectroscopy in materials science: a user-oriented guide (Vol. 49). Springer Science & Business Media.

172. https://xpssimplified.com/whatisxps.php

173. Kubelka, P., & Munk, F. (1931). An article on optics of paint layers. Z. Tech. Phys, 12(593-601).

174. Tauc, J. (1968). Optical properties and electronic structure of amorphous Ge and Si. Materials Research Bulletin, 3(1), 37-46.

175. Kumar, C. S. (Ed.). (2013). UV-VIS and photoluminescence spectroscopy for nanomaterials characterization (pp. 231-285). Berlin, Heidelberg: Springer.

176. Kumar, C. S. (Ed.). (2012). Raman spectroscopy for nanomaterials characterization. Springer Science & Business Media.

177. https://chem.libretexts.org/Core/Physical_and_Theoretical_Chemistry/Spectroscopy/Vibrational_Spectroscopy/Infrared_Spectroscopy/How_an_FTIR_Spectrometer_Operates

178. https://www.thermofisher.com/sa/en/home/industrial/spectroscopy-elemental-isotope-analysis/spectroscopy-elemental-isotope-analysis-learning-center/molecular-spectroscopy-information/ftir-information/ftir-basics.html

179. Wang M, Wu Z, Dai L. Graphitic carbon nitrides supported by nitrogen-doped graphene as efficient metal-free electrocatalysts for oxygen reduction. Journal of Electroanalytical Chemistry 2015; 753:16–20

180. Naebe, M., Wang, J., Amini, A., Khayyam, H., Hameed, N., Li, L.H., Chen, Y. and Fox, B., 2014. Mechanical property and structure of covalent functionalised graphene/epoxy nanocomposites. Scientific reports, 4.

181. Wang, X., Blechert, S., & Antonietti, M. (2012). Polymeric graphitic carbon nitride for heterogeneous photocatalysis. ACS Catalysis, 2(8), 1596-1606.

182. Mao, J., Peng, T., Zhang, X., Li, K., Ye, L., & Zan, L. (2013). Effect of graphitic carbon nitride microstructures on the activity and selectivity of photocatalytic CO_2 reduction under visible light. Catalysis Science & Technology, 3(5), 1253-1260.

183. Adekoya, D. O., Tahir, M., & Amin, N. A. S. (2017). $gC_3N_4/(Cu/TiO_2)$ nanocomposite for enhanced photoreduction of CO_2 to CH 3 OH and HCOOH under UV/visible light. Journal of CO_2 Utilization, 18, 261-274.

184. Cao, S.W., Liu, X.F., Yuan, Y.P., Zhang, Z.Y., Liao, Y.S., Fang, J., Loo, S.C.J., Sum, T.C. and Xue, C., 2014. Solar-to-fuels conversion over In2O3/gC_3N_4 hybrid photocatalysts. Applied Catalysis B: Environmental, 147, pp.940-946.

185. Xia, P., Zhu, B., Yu, J., Cao, S., & Jaroniec, M. (2017). Ultra-thin nanosheet assemblies of graphitic carbon nitride for enhanced photocatalytic CO_2 reduction. Journal of Materials Chemistry A, 5(7), 3230-3238.

186. He, Y., Wang, Y., Zhang, L., Teng, B., & Fan, M. (2015). High-efficiency conversion of CO_2 to fuel over ZnO/gC_3N_4 photocatalyst. Applied Catalysis B: Environmental, 168, 1-8.

187. Zhang, J., Zhang, G., Chen, X., Lin, S., Möhlmann, L., Dołęga, G., Lipner, G., Antonietti, M., Blechert, S. and Wang, X., 2012. Co‐Monomer Control of Carbon Nitride Semiconductors to Optimize Hydrogen Evolution with Visible Light. Angewandte Chemie, 124(13), pp.3237-3241.

188. Chen, Y., Li, J., Hong, Z., Shen, B., Lin, B., & Gao, B. (2014). Origin of the enhanced visible-light photocatalytic activity of CNT modified gC_3N_4 for H_2 production. Physical Chemistry Chemical Physics, 16(17), 8106-8113.

189. Dong, F., Wu, L., Sun, Y., Fu, M., Wu, Z., & Lee, S. C. (2011). Efficient synthesis of polymeric gC_3N_4 layered materials as novel efficient visible light driven photocatalysts. Journal of Materials Chemistry, 21(39), 15171-15174.

190. Lee EZ, Jun YS, Hong WH, Thomas A, Jin MM. Cubic mesoporous graphitic carbon (IV) nitride: an all-in-one chemosensor for selective optical sensing of metal ions. Angewandte Chemie International Edition 2010; 49(50):9706–9710.

191. Wang, P., Wang, Z., Jia, L., & Xiao, Z. (2009). Origin of the catalytic activity of graphite nitride for the electrochemical reduction of oxygen: geometric factors vs. electronic factors. Physical Chemistry Chemical Physics, 11(15), 2730-2740.

192. Xiang, Q., Yu, J., & Jaroniec, M. (2011). Preparation and enhanced visible-light photocatalytic H_2-production activity of graphene/C_3N_4 composites. The Journal of Physical Chemistry C, 115(15), 7355-7363.

193. Zheng, Y., Liu, J., Liang, J., Jaroniec, M., & Qiao, S. Z. (2012). Graphitic carbon nitride materials: controllable synthesis and applications in fuel cells and photocatalysis. Energy & Environmental Science, 5(5), 6717-6731.

194. Kroke E, Schwarz M. Novel group 14 nitrides. Coordination Chemistry Reviews 2004; 248(5):493–532.

195. Kang, Y., Yang, Y., Yin, L. C., Kang, X., Liu, G., & Cheng, H. M. (2015). An Amorphous Carbon Nitride Photocatalyst with Greatly Extended Visible-Light-Responsive Range for Photocatalytic Hydrogen Generation. Advanced Materials, 27(31), 4572-4577.

196. Tang, Z., Zhang, L., Zeng, C., Lin, T., & Guo, B. (2012). General route to graphene with liquid-like behavior by non-covalent modification. Soft Matter, 8(35), 9214-9220.

197. Zhu, B., Xia, P., Ho, W., & Yu, J. (2015). Isoelectric point and adsorption activity of porous gC_3N_4. Applied Surface Science, 344, 188-195.

198. Niu, P., Zhang, L., Liu, G., & Cheng, H. M. (2012). Graphene-like carbon nitride nanosheets for improved photocatalytic activities. Advanced Functional Materials, 22(22), 4763-4770.

199. Zhang, J., Zhang, M., Zhang, G., & Wang, X. (2012). Synthesis of carbon nitride semiconductors in sulfur flux for water photoredox catalysis. ACS Catalysis, 2(6), 940-948.

200. Dong, F., Wang, Z., Sun, Y., Ho, W. K., & Zhang, H. (2013). Engineering the nanoarchitecture and texture of polymeric carbon nitride semiconductor for enhanced visible light photocatalytic activity. Journal of colloid and interface science, 401, 70-79.

201. Song L, Zhang S, Wu X, Tian H, Wei Q. Graphitic C_3N_4 photo-catalyst for esterification of benzaldehyde and alcohol under visible light radiation. Industrial & Engineering Chemistry Research 2012; 51(28):9510–9514.

202. Vinu A. Two-dimensional hexagonally-ordered mesoporous carbon nitrides with tunable pore diameter, surface area and nitrogen content. Advanced Functional Materials 2008; 18(5):816–827.

203. Jiang J, Cheng W, Zhang Y, Lan M, Zhu H, Shen D. Deposition of crystalline C_3N_4 films via microwave plasma chemical vapour deposition. Materials Letters 2007; 61(11):2243–2246.

204. Vinu A, Ariga K, Mori T, Nakanishi T, Hishita S, Golberg D, Bando Y. Preparation and characterization of well-ordered hexagonal mesoporous carbon nitride. Advanced Materials 2005; 17(13):1648–1652.

205. Thomé T, Colaux JL, Louette P, Terwagne G. Formation of carbon nitride compounds during successive implantations in copper. Journal of Electron Spectroscopy and Related Phenomena 2006; 151(1):19–23.

206. Lu Q, Cao C, Li C, Zhang J, Zhu H, Kong X, Duan X. Formation of crystalline carbon nitride powder by a mild solvothermal method. Journal of Materials Chemistry 2003; 13(6):1241–1243.

207. Gu Y, Chen L, Shi L, Ma J, Yang Z, Qian Y. Synthesis of C_3N_4 and graphite by reacting cyanuric chloride with calcium cyanamide. Carbon 2003; 41(13):2674–2676.

208. Niu P, Liu G, Cheng HM. Nitrogen vacancy-promoted photo-catalytic activity of graphitic carbon nitride. The Journal of Physical Chemistry C 2012; 116(20):11013–11018.

209. Dai H, Gao X, Liu E, Yang Y, Hou W, Kang L, Fan J, Hu X. Synthesis and characterization of graphitic carbon nitride sub-microspheres using microwave method under mild condition. Diamond and Related Materials 2013; 38:109–117.

210. Raymundo-Pinero, E., Cazorla-Amorós, D., Linares-Solano, A., Find, J., Wild, U., & Schlögl, R. (2002). Structural characterization of N-containing activated carbon fibers prepared from a low softening point petroleum pitch and a melamine resin. Carbon, 40(4), 597-608.

211. Thomas, A., Fischer, A., Goettmann, F., Antonietti, M., Müller, J. O., Schlögl, R., & Carlsson, J. M. (2008). Graphitic carbon nitride materials: variation of structure and morphology and their use as metal-free catalysts. Journal of Materials Chemistry, 18(41), 4893-4908.

212. Yan, S. C., Li, Z. S., & Zou, Z. G. (2009). Photodegradation performance of g-C_3N_4 fabricated by directly heating melamine. Langmuir, 25(17), 10397-10401.

213. Wang Y, Wang X, Antonietti M, Zhang Y. Facile onepot synthesis of nanoporous carbon nitride solids by using soft templates. Chem. Sus. Chem 2010; 3(4):435–439.

214. Datta KK, Balasubramanian VV, Ariga K, Mori T, Vinu A. Highly crystalline and conductive nitrogendoped mesoporous carbon with graphitic walls and its electrochemical performance. Chemistry–A European Journal 2011; 17(12):3390–3397.

215. Chen, Y., Wang, B., Lin, S., Zhang, Y., & Wang, X. (2014). Activation of n→ π* transitions in two-dimensional conjugated polymers for visible light photocatalysis. The Journal of Physical Chemistry C, 118(51), 29981-29989.

216. Wen J et al. A review on g-C_3N_4-based photocatalysts. Applied Surface Science 2016.

217. Muñoz-Rojas, D., Oró-Solé, J., Ayyad, O., & Gómez-Romero, P. (2011). Shaping hybrid nanostructures with polymer matrices: the formation mechanism of silver–polypyrrole core/shell nanostructures. Journal of Materials Chemistry, 21(7), 2078-2086.

218. Xu, L., Wei, B., Liu, W., Zhang, H., Su, C., & Che, J. (2013). Flower-like ZnO-Ag2O composites: precipitation synthesis and photocatalytic activity. Nanoscale research letters, 8(1), 536.

219. Stern, K. H. (1972). High temperature properties and decomposition of inorganic salts part 3, nitrates and nitrites. Journal of Physical and Chemical Reference Data, 1(3), 747-772.

220. Li, P., Ouyang, S., Xi, G., Kako, T., & Ye, J. (2012). The effects of crystal structure and electronic structure on photocatalytic H_2 evolution and CO_2 reduction over two phases of perovskite-structured $NaNbO_3$. The Journal of Physical Chemistry C, 116(14), 7621-7628.

221. Liu, Q., Chai, Y., Zhang, L., Ren, J., & Dai, W. L. (2017). Highly efficient Pt/$NaNbO_3$ nanowire photocatalyst: Its morphology effect and application in water purification and H_2 production. Applied Catalysis B: Environmental, 205, 505-513.

222. Molecular and Solid Water - a Comparative ESCA Study Volume 921 of Institute of Physics, Uppsala University: Fysiska Institutionen, Inst. of Physics, Univ., 1976

223. Ho, S. F., Contarini, S., & Rabalais, J. W. (1987). Ion-beam-induced chemical changes in the oxyanions (Moyn-) and oxides (Mox) where M= chromium, molybdenum,

tungsten, vanadium, niobium and tantalum. Journal of Physical Chemistry, 91(18), 4779-4788.

224. Kaushik, V. K. (1991). XPS core level spectra and Auger parameters for some silver compounds. Journal of Electron Spectroscopy and Related Phenomena, 56(3), 273-277.

225. NIST X-ray Photoelectron Spectroscopy Database, Version 4.1 (National Institute of Standards and Technology, Gaithersburg, 2012); Retrieved from http://srdata.nist.gov/xps/

226. Schiavello, M. (1993). Some working principles of heterogeneous photocatalysis by semiconductors. Electrochimica acta, 38(1), 11-14.

227. Teixeira, G. F., Wright, T. R., Manfroi, D. C., Longo, E., Varela, J. A., & Zaghete, M. A. (2015). Photoluminescence in $NaNbO_3$ particles and films. Materials Letters, 139, 443-446.

228. Fresno, F., Jana, P., Reñones, P., Coronado, J. M., Serrano, D. P., & de la Peña O'Shea, V. A. (2017). CO_2 reduction over $NaNbO_3$ and $NaTaO_3$ perovskite photocatalysts. Photochemical & Photobiological Sciences, 16(1), 17-23.

229. Li, X. Z., Li, F. B., Yang, C. L., & Ge, W. K. (2001). Photocatalytic activity of WO_x-TiO_2 under visible light irradiation. Journal of Photochemistry and Photobiology A: Chemistry, 141(2), 209-217.

230. Linsebigler, A. L., Lu, G., & Yates Jr, J. T. (1995). Photocatalysis on TiO_2 surfaces: principles, mechanisms, and selected results. Chemical reviews, 95(3), 735-758.

231. Miyashita, K., Kuroda, S. I., Tajima, S., Takehira, K., Tobita, S., & Kubota, H. (2003). Photoluminescence study of electron–hole recombination dynamics in the vacuum-deposited SiO_2/TiO_2 multilayer film with photo-catalytic activity. Chemical physics letters, 369(1), 225-231.

232. Shi, H., Chen, G., Zhang, C., & Zou, Z. (2014). Polymeric g-C_3N_4 coupled with $NaNbO_3$ nanowires toward enhanced photocatalytic reduction of CO_2 into renewable fuel. ACS Catalysis, 4(10), 3637-3643.

233. Xu, J., Zhang, F., Sun, B., Du, Y., Li, G., & Zhang, W. (2015). Enhanced photocatalytic property of Cu doped sodium niobate. International Journal of Photoenergy, 2015.

234. Maeda, K., & Mallouk, T. E. (2009). Comparison of two-and three-layer restacked Dion–Jacobson phase niobate nanosheets as catalysts for photochemical hydrogen evolution. Journal of Materials Chemistry, 19(27), 4813-4818.

235. Park, S., Song, H. J., Lee, C. W., Hwang, S. W., & Cho, I. S. (2015). Enhanced photocatalytic activity of ultrathin Ba5Nb4O15 two-dimensional nanosheets. ACS applied materials & interfaces, 7(39), 21860-21867.

236. Shi, H., Li, X., Wang, D., Yuan, Y., Zou, Z., & Ye, J. (2009). $NaNbO_3$ nanostructures: facile synthesis, characterization, and their photocatalytic properties. Catalysis letters, 132(1-2), 205-212, p41

237. Yu B, Zhou Y, Li P, Tu W, Li P, Tang L, Ye J, Zou Z. Photo-catalytic reduction of CO_2 over Ag/TiO_2 nanocomposites prepared with a simple and rapid silver mirror method. Nanoscale 2016; 8(23):11870–11874.

238. An C, Wang J, Jiang W, Zhang M, Ming X, Wang S, Zhang Q. Strongly visible-light responsive plasmonic shaped AgX:Ag (X= Cl, Br) nanoparticles for reduction of CO_2 to methanol. Nanoscale 2012; 4(18):5646–5650.

239. Tahir M, Tahir B, Amin NAS, Alias H. Selective photocatalytic reduction of CO_2 by H_2O/H2 to CH_4 and CH_3OH over Cu-promoted In2O3/TiO_2 nanocatalyst. Applied Surface Science 2016; 389:46–55.

240. Amano F, Yasumoto T, Prieto-Mahaney OO, Uchida S, Shibayama T, Ohtani B. Photo-catalytic activity of octahedral single-crystalline mesoparticles of anatase titanium (IV) oxide. Chemical Communications 2009; 17:2311–2313.

241. International Union Of Pure And Applied Chemistry Terminology, Relative Photonic Efficiencies And Quantum Yields in Heterogeneous Photocatalysis. Part I:Suggested Protocol, Pure & Appl. Chem., 71 (1999) 303–320.

242. Yamashita H, Ikeue K, Takewaki T, Anpo M (2002) In situ XAFS studies on the effects of the hydrophobic-hydrophilic properties of Ti-Beta zeolites in the photocatalytic reduction of CO_2 with H_2O. Top Catal 18(1–2):95–100

243. Yamashita H, Okazaki M, Ikeue K, Anpo M (2004). Photocatalytic reduction of CO_2 with H_2O on Ti-containing mesoporous silica hydrophobically modified using fluoride ions. In: Sang-Eon Park J-SC, Kyu-Wan L (eds.) Stud Surf Sci Catal. Elsevier, Amsterdam, The Netherlands

244. Yamashita H, Fujii Y, Ichihashi Y, Zhang SG, Ikeue K, Park DR, Koyano K, Tatsumi T, Anpo M (1998) Selective formation of CH_3OH in the photocatalytic reduction of CO_2 with H_2O on titanium oxides highly dispersed within zeolites and mesoporous molecular sieves. Catal Today 45(1–4):221–227

245. Ikeue K, Yamashita H, Anpo M, Takewaki T (2001) Photocatalytic reduction of CO_2 with H_2O on Ti–β zeolite photocatalysts: effect of the hydrophobic and hydrophilic properties. J Phys Chem B 105(35):8350–8355

246. Anpo, M., & Chiba, K. (1992). Photocatalytic reduction of CO_2 on anchored titanium oxide catalysts. Journal of Molecular Catalysis, 74(1-3), 207-212.

247. Yamashita, H., Ikeue, K., Takewaki, T., & Anpo, M. (2002). In situ XAFS studies on the effects of the hydrophobic–hydrophilic properties of Ti-Beta zeolites in the photocatalytic reduction of CO_2 with H_2O. Topics in catalysis, 18(1), 95-100.

248. Ikeue, K., Yamashita, H., Takewaki, T., Davis, M. E., & Anpo, M. (2001). Characterization of Ti-Beta zeolites and their reactivity for the photocatalytic reduction of CO_2 with H_2O. Journal of synchrotron radiation, 8(2), 602-604.

249. Li, K., An, X., Park, K. H., Khraisheh, M., & Tang, J. (2014). A critical review of CO_2 photoconversion: catalysts and reactors. Catalysis Today, 224, 3-12.

250. Tsai, C. W., Chen, H. M., Liu, R. S., Asakura, K., & Chan, T. S. (2011). Ni@NiO core–shell structure-modified nitrogen-doped InTaO4 for solar-driven highly efficient CO_2 reduction to methanol. The Journal of Physical Chemistry C, 115(20), 10180-10186.

251. Ola, O., Maroto-Valer, M. M., & Mackintosh, S. (2013). Turning CO_2 into Valuable Chemicals. Energy Procedia, 37, 6704-6709.

252. Mankidy, B. D., Joseph, B., & Gupta, V. K. (2013). Photo-conversion of CO_2 using titanium dioxide: enhancements by plasmonic and co-catalytic nanoparticles. Nanotechnology, 24(40), 405402.

253. Murakami, N., Saruwatari, D., Tsubota, T., & Ohno, T. (2013). Photocatalytic reduction of carbon dioxide over shape-controlled titanium (IV) oxide nanoparticles with co-catalyst loading. Current Organic Chemistry, 17(21), 2449-2453.

254. Chang, X., Wang, T., & Gong, J. (2016). CO_2 photo-reduction: insights into CO_2 activation and reaction on surfaces of photocatalysts. Energy & Environmental Science, 9(7), 2177-2196.

255. Tan SS, Zou L, Hu E. Kinetic modelling for photosynthesis of hydrogen and methane through catalytic reduction of carbon dioxide with water vapor. Catalysis Today 2008; 131(1):125–129.

256. Gattrell M, Gupta N, Co A. A review of the aqueous electrochemical reduction of CO_2 to hydrocarbons at copper. Journal of Electroanalytical Chemistry 2006; 594(1):1–19

257. Neaţu S, Maciá-Agulló JA, Concepción P, Garcia H. Gold–copper nanoalloys supported on TiO_2 as photo-catalysts for CO_2 reduction by water. Journal of the American Chemical Society 2014; 136 (45):15969–15976.

258. https://www.engineeringtoolbox.com/gases-solubility-water-d_1148.html

CV

Personal data

Name: Abul Lais

Date of Birth: October 9, 1989

Nationality: Singaporean

Email: abullais78680@gmail.com

Education

2015 – 2017 MSc in Physics	Physics Department, King Fahd University of Petroleum and minerals, Dhahran 31261, Saudi Arabia *Thesis*: Synthesis and Physico-Chemical Characterization of Semiconducting Nano-crystalline Photocatalysts and its Application in Environmental Remediation
2010 – 2014 BSc (Honors) in Physics	Physics Department, National University of Singapore 21 Lower Kent Ridge Rd, Singapore 119077 *Thesis:* Frequency doubling and spectroscopy using fiber amplifiers

ISI-cited publications arising from this thesis

1. ***Abul Lais***, M. A. Gondal, M. A. Dastageer. A review of semiconducting oxide photocatalysts for reduction of CO_2 to methanol, Environmental Chemistry Letters (ECLE-D-17-00335) **PUBLISHED (I.F. = 3.594)**
2. ***Abul Lais***, M. A. Gondal, M. A. Dastageer, F. F. Al-Adel. Experimental Parameters affecting the Photocatalytic Reduction Performance of CO_2 to Methanol: A Review, International Journal of Energy Research (ER-17-8750) **ACCEPTED, UNDER PRODUCTION (I.F. = 2.598)**
3. M.A. Gondal, ***Abul Lais***, Dastageer, Umair Baig, Yang Deyuan, Chang Xiaofeng, Kai Shen. Photocatalytic Conversion of CO_2 into Methanol using Graphitic Carbon Nitride under Solar, UV Laser and Broadband Radiations. International Journal of Energy Research (Article DOI: 10.1002/er.3777) **PUBLISHED (I.F. = 2.598)**